Pramana – J. Phys. (2017) 88: 79
DOI 10.1007/s12043-017-1373-4

Invited review: Physics potential of the ICAL detector at the India-based Neutrino Observatory (INO)

A KUMAR[12], A M VINOD KUMAR[16], ABHIK JASH[6,14], AJIT K MOHANTY[4,6], ALEENA CHACKO[8], ALI AJMI[6,7], AMBAR GHOSAL[6,14], AMINA KHATUN[6,10], AMITAVA RAYCHAUDHURI[17], AMOL DIGHE[15], ANIMESH CHATTERJEE[5,6], ANKIT GAUR[18], ANUSHREE GHOSH[5,6], ASHOK KUMAR[18], ASMITA REDIJ[15], B SATYANARAYANA[15], B S ACHARYA[15], BRAJESH C CHOUDHARY[18], C RANGANATHAIAH[21], C D RAVIKUMAR[16], CHANDAN GUPTA[6,13], D INDUMATHI[6,9], DALJEET KAUR[18], DEBASISH MAJUMDAR[6,14], DEEPAK SAMUEL[15], DEEPAK TIWARI[5,6], G RAJASEKARAN[6,9], GAUTAM GANGOPADHYAY[17], GOBINDA MAJUMDER[15], H B RAVIKUMAR[21], J B SINGH[12], J S SHAHI[12], JAMES LIBBY[8], JYOTSNA SINGH[20], K RAVEENDRABABU[6,8], K K MEGHNA[6,9], K R REBIN[8], KAMALESH KAR[6,14], KOLAHAL BHATTACHARYA[15], LALIT M PANT[4,6], M SAJJAD ATHAR[1], M V N MURTHY[6,9], MANZOOR A MALIK[19], MD NAIMUDDIN[18], MOHAMMAD SALIM[1], MONOJIT GHOSH[13], MOON MOON DEVI[6,15], NABA K MONDAL[15], NAYANA MAJUMDAR[6,14], NITA SINHA[6,9], NITALI DASH[4,6], POMITA GHOSHAL[13], POONAM MEHTA[11], PRAFULLA BEHERA[8], R KANISHKA[12], RAJ GANDHI[5,6], RAJESH GANAI[6,23], RASHID HASAN[1], S KRISHNAVENI[21], S M LAKSHMI[6,9], S K SINGH[1], S S R INBANATHAN[2], S UMA SANKAR[7], SADIQ JAFER[8], SAIKAT BISWAS[6,23], SANJEEV KUMAR[18], SANJIB KUMAR AGARWALLA[6,10], SANDHYA CHOUBEY[5,6], SATYAJIT SAHA[6,14], SHAKEEL AHMED[1], SHIBA PRASAD BEHERA[4,6], SRUBABATI GOSWAMI[13], SUBHASIS CHATTOPADHYAY[6,23], SUDEB BHATTACHARYA[6,14], SUDESHNA BANERJEE[15], SUDESHNA DASGUPTA[15], SUMANTA PAL[6,9], SUPRATIK MUKHOPADHYAY[6,14], SUSHANT RAUT[13], SUVENDU BOSE[6,14], SWAPNA MAHAPATRA[22], TAPASI GHOSH[6,23], TARAK THAKORE[15], V K S KASHYAP[4,6], V S SUBRAHMANYAM[3], VENKTESH SINGH[3], VINAY B CHANDRATRE[4,6], VIPIN BHATNAGAR[12], VIVEK M DATAR[4,15], WASEEM BARI[19] and Y P VIYOGI[6,23]

[1]Aligarh Muslim University, Aligarh 202 001, India
[2]The American College, Madurai 625 002, India
[3]Banaras Hindu University, Varanasi 221 005, India
[4]Bhabha Atomic Research Centre, Trombay, Mumbai 400 085, India
[5]Harish Chandra Research Institute, Jhunsi, Allahabad 211 019, India
[6]Homi Bhabha National Institute, Anushakti Nagar, Mumbai 400 085, India
[7]Indian Institute of Technology Bombay, Powai, Mumbai 400 076, India
[8]Indian Institute of Technology Madras, Chennai 600 036, India
[9]Institute of Mathematical Sciences, Taramani, Chennai 600 113, India
[10]Institute of Physics, Sachivalaya Marg, Bhubaneswar 751 005, India
[11]Jawaharlal Nehru University, New Delhi 110 067, India
[12]Panjab University, Chandigarh 160 014, India
[13]Physical Research Laboratory, Navrangpura, Ahmedabad 380 009, India
[14]Saha Institute of Nuclear Physics, Bidhannagar, Kolkata 700 064, India
[15]Tata Institute of Fundamental Research, Colaba, Mumbai 400 005, India
[16]University of Calicut, Kozhikode 673 635, India
[17]University of Calcutta, Kolkata 700 009, India
[18]University of Delhi, New Delhi 110 021, India

[19]University of Kashmir, Hazratbal, Srinagar 190 006, India
[20]University of Lucknow, Lucknow 226 007, India
[21]University of Mysore, Mysuru 570 005, India
[22]Utkal University, Vani Vihar, Bhubaneswar 751 004, India
[23]Variable Energy Cyclotron Centre, Bidhannagar, Kolkata 700 064, India
Spokesperson: Naba K Mondal. E-mail: nkm@tifr.res.in
THE ICAL COLLABORATION: http://www.tifr.res.in/~ino

MS received 4 July 2015; revised 3 October 2016; accepted 1 December 2016; published online 26 April 2017

Abstract. The upcoming 50 kt magnetized iron calorimeter (ICAL) detector at the India-based Neutrino Observatory (INO) is designed to study the atmospheric neutrinos and antineutrinos separately over a wide range of energies and path lengths. The primary focus of this experiment is to explore the Earth matter effects by observing the energy and zenith angle dependence of the atmospheric neutrinos in the multi-GeV range. This study will be crucial to address some of the outstanding issues in neutrino oscillation physics, including the fundamental issue of neutrino mass hierarchy. In this document, we present the physics potential of the detector as obtained from realistic detector simulations. We describe the simulation framework, the neutrino interactions in the detector, and the expected response of the detector to particles traversing it. The ICAL detector can determine the energy and direction of the muons to a high precision, and in addition, its sensitivity to multi-GeV hadrons increases its physics reach substantially. Its charge identification capability, and hence its ability to distinguish neutrinos from antineutrinos, makes it an efficient detector for determining the neutrino mass hierarchy. In this report, we outline the analyses carried out for the determination of neutrino mass hierarchy and precision measurements of atmospheric neutrino mixing parameters at ICAL, and give the expected physics reach of the detector with 10 years of runtime. We also explore the potential of ICAL for probing new physics scenarios like CPT violation and the presence of magnetic monopoles.

Keywords. Neutrino physics; atmospheric neutrinos; neutrino experiments; India-based neutrino observatory.

PACS Nos 14.60.Pq; 29.40.Gx

Preface

The past two decades in neutrino physics have been very eventful, and have established this field as one of the flourishing areas of high-energy physics. Starting from the confirmation of neutrino oscillations that resolved the decades-old problems of the solar and atmospheric neutrinos, we have now been able to show that neutrinos have non-zero masses, and different flavours of neutrinos mix among themselves. Our understanding of neutrino properties has increased by leaps and bounds. Many experiments have been constructed and envisaged to explore different facets of neutrinos, in particular their masses and mixing.

The iron calorimeter (ICAL) experiment at the India-based Neutrino Observatory (INO) [1] is one of the major detectors that is expected to see the light of the day soon. It will have unique features like the ability to distinguish muon neutrinos from antineutrinos at GeV energies, and measure the energies of hadrons in the same energy range. It is therefore well suited for the identification of neutrino mass hierarchy, the measurement of neutrino mixing parameters, and many probes of new physics. The site for the INO has been identified, and the construction is expected to start soon. In the meanwhile, the R&D for the ICAL detector, including the design of its modules, the magnet coils, the active detector elements and the associated electronics, has been underway over the past decade. The efforts to understand the capabilities and physics potentials of the experiment through simulations are in progress at the same time.

We present here the status report of our current understanding of the physics reach of the ICAL, prepared by the Simulations and Physics Analysis Groups of the INO Collaboration. It describes the framework being used for the simulations, the expected response of the detector to particles traversing it, and the results we expect to obtain after the 50 kt ICAL has been running for about a decade. The focus of the physics

analysis is on the identification of the mass hierarchy and precision measurements of the atmospheric neutrino mixing parameters. The feasibilities of searches for some new physics, in neutrino interactions as well as elsewhere, that can be detected at the ICAL, are also under investigation.

The first such report [2] had been published when the INO was being proposed, and the ICAL Collaboration was at its inception. Our understanding of the detector has now matured quite a bit, and more realistic results can now be obtained, which have been included in this report. The work on improving several aspects of the detector, the simulations, the reconstruction algorithms and the analysis techniques is in progress and will remain so for the next few years. This review is thus not the final word, but a work in progress that will be updated at regular intervals.

In addition to the ICAL detector, the INO facility is designed to accommodate experiments in other areas like neutrinoless double beta decay, dark matter search, low-energy neutrino spectroscopy, etc. Preliminary investigations and R&D in this direction are in progress. The special environment provided by the underground laboratory may also be useful to conduct experiments in rock mechanics, geology, biology etc. This report focusses mainly on the ongoing physics and simulation related to the ICAL detector. The details of other experiments will be brought out separately.

The Government of India has recently (December 2014) given its approval for the establishment of INO. This is a good opportunity to present the physics capabilities of the ICAL experiment in a consolidated form.

Executive summary

The INO and the ICAL detector

The INO is proposed to be built in Bodi West Hills, in Theni district of Tamil Nadu in South India. The main detector proposed to be built at the INO is the magnetized ICAL with a mass of 50 kt. The major physics goal of ICAL is to study neutrino properties, through the observation of atmospheric neutrinos that cover a wide range of energies and path lengths. A special emphasis will be on the determination of neutrino mass hierarchy, by observing the matter effects when they travel through the Earth. This would be facilitated through the ability of ICAL to distinguish neutrinos from antineutrinos.

Table 1. Specifications of the ICAL detector.

ICAL	
No. of modules	3
Module dimension	16 m × 16 m × 14.5 m
Detector dimension	48 m × 16 m × 14.5 m
No. of layers	151
Iron plate thickness	5.6 cm
Gap for RPC trays	4.0 cm
Magnetic field	1.5 T
RPC	
RPC unit dimension	2 m × 2 m
Read-out strip width	3 cm
No. of RPC units/layer/module	64
Total no. of RPC units	∼30,000
No. of electronic readout channels	3.9×10^6

Table 1 gives the salient features of the ICAL detector. The active detector elements in ICAL will be the resistive plate chambers (RPCs). The detector is optimized to be sensitive primarily to the atmospheric muon neutrinos in the 1–15 GeV energy range. The structure of the detector, with its horizontal layers of iron interspersed with RPCs, allows it to have an almost complete coverage to the direction of incoming neutrinos, except for those that produce almost horizontally travelling muons. This makes it sensitive to a large range of path lengths L for the neutrinos travelling through the Earth, while the atmospheric neutrino flux provides a wide spectrum in the neutrino energy E_ν.

ICAL will be sensitive to both the energy and direction of the muons that will be produced in charged-current (CC) interactions of the atmospheric muon neutrinos (and antineutrinos) with the iron target in the detector. In addition, the fast response time of the RPCs (of the order of nanoseconds) will allow for a discrimination of the upward-going muon events and downward-going ones. (Once the starting point of the track is identified, the initial hits in the track determine the initial muon direction accurately.) This direction discrimination separates the neutrinos with short path lengths from those with longer ones. Such a separation is crucial because the neutrino oscillation probability is strongly dependent on the path length L.

Moreover, as ICAL is expected to be magnetized to about 1.5 T in the plane of the iron plates, it will be able to discriminate between muons of different charges, and hence will be capable of differentiating events induced by muon neutrinos and muon antineutrinos. Through this sensitivity, one can probe the difference

in matter effects in the propagation of neutrinos and antineutrinos that traverse the Earth before they reach the detector. This in turn will allow for a sensitivity to the neutrino mass hierarchy, which is the primary goal of the ICAL experiment.

The magnetic field is also crucial for reconstructing the momentum of the muon tracks in the case of partially contained events. When the muon track is completely contained inside the detector, the length of the track can determine the energy of the muon reliably, and the magnetic field plays a supplementary role of improving the momentum resolution. However, for the partially contained track events, the bending of the track in the local magnetic field is crucial to reconstruct the muon momentum in the energies of interest. The good tracking ability and energy resolution of ICAL for muons makes it very well suited for the study of neutrino oscillation physics through the observation of atmospheric neutrinos.

In addition, ICAL is also sensitive to the energy deposited by hadrons in the detector in the multi-GeV range, a unique property that enables a significant improvement in the physics reach of ICAL, as will be clear in this review. In the present configuration, the sensitivity of ICAL to electrons is very limited; however, this is still under investigation.

Though the ICAL is yet to be built, its putative properties have been simulated using the CERN GEANT4 [3] package. The details of these simulations have been presented in §3. Section 4 presents results on the response of ICAL to particles traversing through it. The resultant physics potential of the detector, obtained from these simulations, is given in later sections, where we focus on the identification of neutrino mass hierarchy, and the precise determinations of the atmospheric neutrino parameters: $|\Delta m^2_{\rm eff}|$ and $\sin^2 2\theta_{23}$, as well as the octant of θ_{23}. In addition, we also discuss some novel and exotic physics possibilities that may be explored at ICAL.

The simulation framework

For the results presented in this review, the atmospheric neutrino events have been generated with the NUANCE [4] neutrino generator using the Honda 3d fluxes [5] for the Kamioka site in Japan. The details of the fluxes have been presented in §2. The Honda atmospheric neutrino fluxes at Theni, the INO site, are expected to be finalized soon and will be used when available. A preliminary comparison of the fluxes at the two sites is also presented in Appendix A of this review. The number of muon track events are expected to be similar, within statistical errors, for both fluxes, for energies more than 3 GeV. We, therefore, do not expect the reach of ICAL, especially for the mass hierarchy, to change significantly with the use of the Theni fluxes.

A typical CC interaction of ν_μ in the detector gives rise to a charged muon that leaves a track, and single or multiple hadrons that give rise to shower-like features. The simulations of the propagation of muons and hadrons in the detector have been used to determine the response of the detector to these particles. This leads to the determination of detection efficiencies, charge identification efficiencies, calibrations and resolutions of energies, and directions of the particles. The results of these simulations are presented in §4.

In order to perform the physics analysis, we generate a large number (typically, an exposure of 1000 years) of unoscillated events using NUANCE, which are later scaled to a suitable exposure, and oscillations are included using a reweighting algorithm. The typical values of oscillation parameters used are close to their best-fit values, and are given in table 2. Here $\Delta m^2_{\rm eff} \equiv \Delta m^2_{32} - (\cos^2\theta_{12} - \cos\delta_{\rm CP}\sin\theta_{32}\sin 2\theta_{12}\tan\theta_{23})\Delta m^2_{21}$ is the effective value of $\Delta m^2_{\rm atm}$ relevant for the two-neutrino analysis of atmospheric neutrino oscillations [6,7]. The energies and directions of the relevant particles are then smeared according to the resolutions determined earlier. This approach thus simulates the average behaviour of the measured quantities. 'At the current stage of simulations, we also assume that the muon track and the hadron shower can be separated with full efficiency, and that the noise due to random hits near the signal events in the short time interval of the event is negligible. While these approximations are reasonable, they still need to be justified with actual detector, possibly

Table 2. True values of the input oscillation parameters used in the analyses, unless otherwise specified. For more details, including 3σ limits on these parameters, see table 1.1.

Δm^2_{21} (eV^2)	$\Delta m^2_{\rm eff}$ (eV^2)	$\sin^2\theta_{12}$	$\sin^2\theta_{23}$	$\sin^2 2\theta_{13}$	$\delta_{\rm CP}$
7.5×10^{-5}	2.4×10^{-3}	0.3	0.5	0.1	0°

by collecting data with a prototype. In the meantime, a complete simulation, which involves passing each of the generated event through a GEANT4 simulation of the ICAL detector, is in progress.'

The different analyses then determine the relevant physics results through a standard χ^2 minimization procedure, with the systematic errors included through the method of pulls, marginalizations over the allowed ranges of parameters, and including information available from other experiments using priors. The details of the analysis procedures for obtaining the neutrino mixing parameters are given in §5, which presents the results using only the information on muon energy and angle, as well as the improvement due to the inclusion of information on hadron energies. Section 6 further includes combined analyses of the reach of ICAL with other current and near-future detectors such as T2K and NOνA, for the mass hierarchy and neutrino oscillation parameters. Section 7 discusses the reach of ICAL with respect to exotic physics possibilities such as the violation of CPT or Lorentz symmetries, the detection of magnetic monopoles, etc.

We now list the highlights of the results compiled in this review. Many of these results have appeared elsewhere [8–16]. However, some have been updated with more recent information.

Detector response to propagating particles

Response to muons

The ICAL detector is optimized for the detection of muons propagating in the detector, identification of their charges, and accurate determination of their energies and directions. The energies and directions of muons are determined through a Kalman filter-based algorithm. The reconstructed energy (direction) for a given true muon energy (direction) is found to give a good fit to the Gaussian distribution, and hence the resolution is described in terms of the mean and standard deviation of a Gaussian distribution. The reconstruction efficiency for muons with energies above 2 GeV is expected to be more than 80%, while the charge of these reconstructed muons is identified correctly on more than 95% occasions. The direction of these muons at the point of their production can be determined to within about a degree. The muon energy resolution depends on the part of the detector the muon is produced in, but is typically 25% (12%) at 1 GeV (20 GeV), as can be seen in the left panel of figure 1 [8].

Response to hadrons

The detector response to hadrons is quantified in terms of the quantity $E'_{\rm had} \equiv E_\nu - E_\mu$ for the CC processes that produce a muon, which is calibrated against the number of hits in the detector. The hit distribution for a given hadron energy is found to give a good fit to the Vavilov distribution. Hence, $E'_{\rm had}$ is calibrated against the mean of the corresponding Vavilov mean for the number of hits, and the energy resolution is taken to be the corresponding value of σ. The energy resolution is shown in figure 1. The complete description of Vavilov distributions needs a total of four parameters, the details of which may be found in §4. The presence of different kinds of hadrons, which are hard to distinguish through the hit information, is taken care of

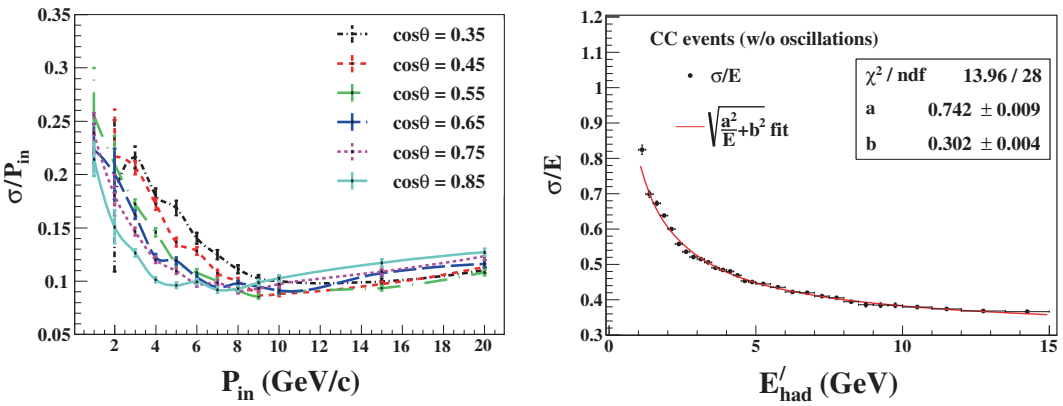

Figure 1. Left panel shows the momentum resolution of muons produced in the region $0 < \phi < \pi/4$ (see §4.1), as functions of the muon momentum in different zenith angle bins [8]. Right panel shows the energy resolution of hadrons (see §4.2) as functions of $E'_{\rm had}$, where events have been generated using NUANCE in different $E'_{\rm had}$ bins. The bin widths are indicated by horizontal error bars [9].

by the generation of events through NUANCE, which is expected to produce hadrons in the right proportions. The energy resolution of hadrons is found to be about 85% (36%) at 1 GeV (15 GeV) [9]. The information on the shape of the hadron shower is not used for extracting hadron energy yet; the work on this front is still in progress.

Physics reach of ICAL

Sensitivity to the mass hierarchy

In order to quantify the reach of ICAL with respect to the neutrino mass hierarchy, a specific hierarchy, normal or inverted, is chosen as the true (input) hierarchy. The CC muon neutrino events are binned in the quantities chosen for the analysis, and a χ^2 analysis is performed taking the systematic errors into account and marginalizing over the 3σ ranges of the parameters $|\Delta m^2_{\text{eff}}|$, $\sin^2\theta_{23}$, and $\sin^2 2\theta_{13}$. The significance of the result is then determined as $\Delta\chi^2_{\text{ICAL-MH}}$ with which the wrong hierarchy can be rejected (see §5).

The analysis for mass hierarchy identification using only the muon momentum information [11] yields $\Delta\chi^2_{\text{ICAL-MH}} \approx 6.5$ with 10 years of exposure of the 50 kt ICAL, as can be seen from figure 2 (black dashed curve), which also shows (red solid curve) that a considerable improvement in the physics reach is obtained if the correlated hadron energy information in each event is included along with the muon energy and direction information; i.e. the binning is performed in the three-dimensional parameter space $(E_\mu, \cos\theta_\mu, E'_{\text{had}})$. The same exposure now allows the identification of mass hierarchy with a significance of $\Delta\chi^2_{\text{ICAL-MH}} \approx 9.5$ [14] for maximal mixing angle ($\sin^2\theta_{23} = 0.5$) and $\sin^2 2\theta_{13} = 0.1$. The significance depends on the actual value of θ_{23} and θ_{13}, and increases with the values of these mixing angles. When $\sin^2\theta_{23}$ and $\sin^2 2\theta_{13}$ are varied in their allowed 3σ ranges, the corresponding significance varies in the range $\Delta\chi^2_{\text{ICAL-MH}} \approx 7$–12.

Precision measurements of oscillation parameters

The precision on the measurements of the neutrino oscillation parameters $\sin^2\theta_{23}$ and $|\Delta m^2_{32}|$ is quantified in terms of $\Delta\chi^2_{\text{ICAL-PM}}(\lambda)$, where λ is the parameter under consideration. The precision on the measurement of θ_{23} is essentially a function of the total number of events, and is expected to be about 12–14%, whether one includes the hadron energy information or not. The precision on $|\Delta m^2_{32}|$, however, improves significantly (from 5.4 to 2.9%) if the information on hadron energy is included.

Figure 3 shows the comparison of the 10-year reach of 50 kt ICAL in the $\sin^2 2\theta_{23}$–Δm^2_{32} plane, with the

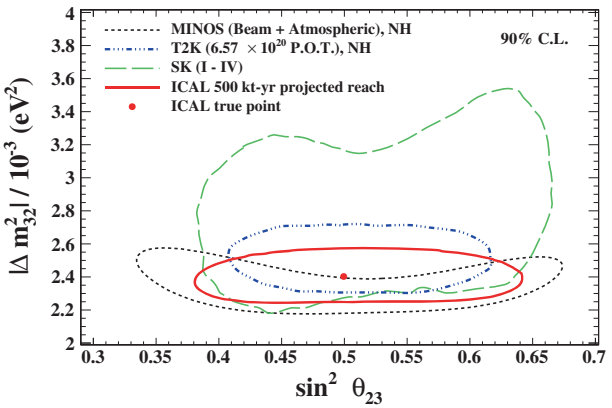

Figure 3. The precision reach of ICAL in the $\sin^2\theta_{23}$–Δm^2_{32} plane, in comparison with other current and planned experiments [14]. Information on hadron energy has been included.

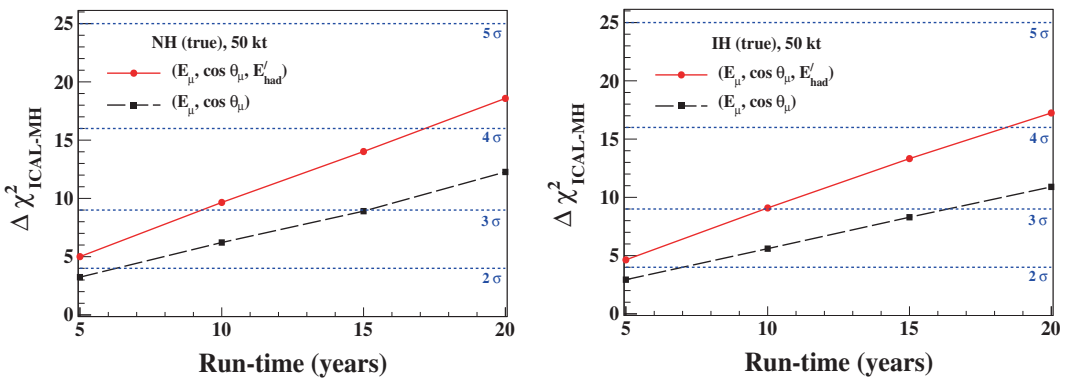

Figure 2. The hierarchy sensitivity of ICAL with input normal (left) and inverted (right) hierarchy including correlated hadron energy information, with $|\Delta m^2_{\text{eff}}|$, $\sin^2\theta_{23}$, and $\sin^2 2\theta_{13}$ marginalized over their 3σ ranges [14]. Improvement with the inclusion of hadron energy is significant.

current limits from other experiments. It is expected that the Δm^2_{32} precision of ICAL would be much better than the atmospheric neutrino experiments that use water Cherenkov detectors, due to its better energy measurement capabilities. However, the beam experiments will keep on accumulating more data, and hence the global role of ICAL for precision measurements of these parameters will not be competitive, but complementary.

Sensitivity to the octant of θ_{23}

While the best-fit value for $\sin^2 2\theta_{23}$ is close to maximal, it is not fully established whether it deviates from maximality, and if so, whether $\sin^2\theta_{23}$ is less than or greater than 0.5, that is, whether it lies in the first or second octant. ICAL is sensitive to the octant of θ_{23} through two kinds of effects: one is through the depletion in atmospheric muon neutrinos (and antineutrinos) via the survival probability $P_{\mu\mu}$ and the other is the contribution of the atmospheric electron neutrinos to the observed CC muon events through the oscillation probability $P_{e\mu}$. Both effects are proportional to $\sin^2 2\theta_{13}$, but, act in opposite directions, thereby reducing the effective sensitivity of ICAL to the θ_{23} octant. The reach of ICAL alone for determining the octant is therefore limited; it can identify the octant to a 2σ significance with 500 kt-yr only if $\sin^2\theta_{23} < 0.37$ [14]. The information from other experiments clearly needs to be included in order to identify the octant.

Synergies with other experiments

Neutrino mass hierarchy determination

The ability of the currently running long-baseline experiments like T2K and NOνA to distinguish between the mass hierarchies depends crucially on the actual value of the CP-violating phase δ_{CP}. For example, if δ_{CP} is vanishing, this ability is severely limited. However, if one adds the data available from the proposed run of these experiments, a preliminary estimation suggests that even for vanishing δ_{CP}, the mass hierarchy identification of 3σ may be achieved with a run-time as low as six years of the 50 kt ICAL, for maximal mixing [17]. This can be observed in figure 4. Note that this improvement in the ICAL sensitivity is not just due to the information provided by these experiments on the mass hierarchy, but also due to the improved constraints on Δm^2_{32} and θ_{23}.

Identifying mass hierarchy at all δ_{CP} values

The large range of path length of the atmospheric neutrinos makes ICAL insensitive to the CP phase δ_{CP}, and as a result its reach in distinguishing the hierarchy is also independent of the actual value of δ_{CP} [18]. On the other hand, the sensitivity of fixed-baseline experiments such as T2K and NOνA is extremely limited if $0 < \delta_{CP} < \pi$ and the true hierarchy is normal. However, adding ICAL information ensures that the hierarchy can be identified even in these unfavoured δ_{CP} regions [11]. Of course, in the δ_{CP} regions favourable to the long-baseline experiments, the ICAL data can only enhance the power of discrimination between the two hierarchies.

Determination of the CP phase

Though ICAL itself is rather insensitive to δ_{CP}, data from ICAL can still improve the determination of δ_{CP} itself, by providing input on mass hierarchy. This is especially crucial in the range $0 \leq \delta_{CP} \leq \pi$, precisely where the ICAL data will also improve the hierarchy discrimination of NOνA and other experiments [19].

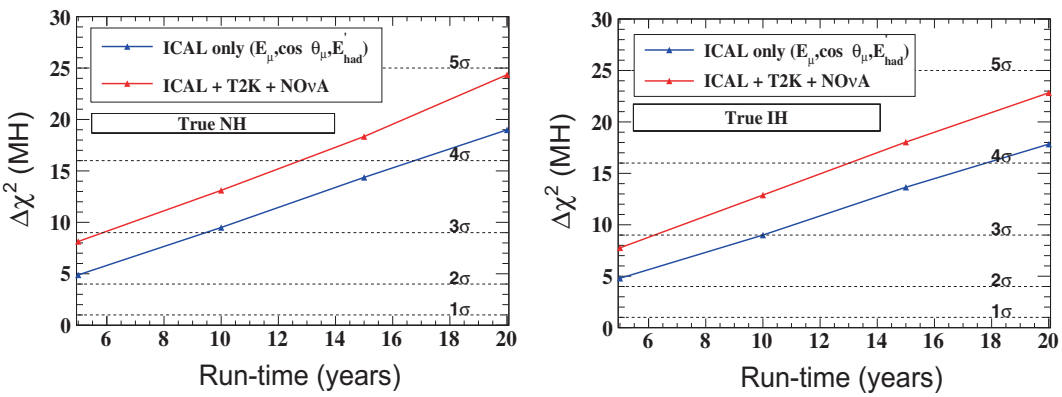

Figure 4. Preliminary results on the hierarchy sensitivity with input normal (left) and inverted (right) hierarchy when ICAL data are combined with the data from T2K (total luminosity of 8×10^{21} protons on target in neutrino mode) and NOνA (three years running in neutrino mode and three years in antineutrino mode) [17].

Other physics possibilities with ICAL

ICAL is a versatile detector, and hence can be employed to test for a multitude of new physics scenarios. For example, the violation of CPT or Lorentz symmetry in the neutrino sector [15] can be probed to a great precision, owing to its excellent energy measurement capability. The passage of magnetic monopoles through the detector may be looked for by simply looking for slowly moving, undeflecting tracks [16]. Dark matter annihilation inside the Sun may be constrained by comparing the flux from the Sun with the flux from other directions. Many such scenarios are currently under investigation.

Concluding remarks

A strong and viable physics programme is ready for ICAL at INO. The simulations based on the incorporation of the ICAL geometry in GEANT4 suggests that the detector will have excellent abilities for detection, charge identification, energy measurement, and direction determination for charged muons of GeV energies. The magnetic field enables separation of μ^- from μ^+, equivalently that of ν_μ from $\bar{\nu}_\mu$, thus increasing the sensitivity to the difference in matter effects on neutrino and antineutrino oscillations. It will also be sensitive to hadrons, an ability that will increase its physics reach significantly and will offer advantages over other atmospheric neutrino detectors. Apart from its main aim of identifying the neutrino mass hierarchy, ICAL can also help in precision measurements of other neutrino mixing parameters, and can probe exotic physics issues even beyond neutrinos.

1. Introduction

The earth is just a silly ball
To them, through which they simply pass
Like dustmaids through a drafty hall
–John Updike

Many important developments have taken place in neutrino physics and neutrino astronomy in recent years. The discovery of neutrino oscillations and consequent inference about the non-vanishing mass of the neutrinos, from the study of neutrinos from the Sun and cosmic rays, have had far-reaching consequences for particle physics, astroparticle physics and nuclear physics. The observation of neutrinos from natural sources as well as those produced at reactors and accelerators has given us the first confirmed signals of physics beyond the Standard Model of particle physics. They have also enabled us access to the energy production mechanisms inside stars and other astrophysical phenomena.

Experimental observations of neutrino interactions began in the mid-1950s at Savannah river reactor by Reines and Cowan [20] followed by experiments deep in the mines of Kolar gold fields (KGF) in India [21] and in South Africa [22]. The pioneering solar neutrino experiments of Davis and collaborators in the USA [23,24], the water Cherenkov detector Kamiokande [25] and its successor the gigantic Super-Kamiokande (SK) [26,27], the gallium detectors SAGE [28] in Russia and Gallex [29], GNO [30] at the Laboratorio National di Gran Sasso (LNGS) in Italy, the heavy-water detector at the Sudbury Neutrino Observatory (SNO) in Canada [31,32], the KamLAND [33] and K2K [34] experiments in Japan, etc. have together contributed in a very fundamental way to our knowledge of neutrino properties and interactions. The observation of solar neutrinos has given a direct experimental proof that the Sun and the stars are powered by thermonuclear fusion reactions that emit neutrinos. The recent results from reactor neutrino experiments, beginning with Double CHOOZ [35] in France and culminating in the results from Reno [36] in Korea and Daya Bay [37] in China, and from accelerator experiments like MINOS [38], T2K [39], and NOνA [40,41] have further revealed properties of neutrinos that not only serve as windows to physics beyond the Standard Model of particle physics, but also provide possibilities of understanding the matter–antimatter asymmetry in the Universe through the violation of the charge-parity (CP) symmetry in the lepton sector.

Impelled by these discoveries and their implications for the future of particle physics and astrophysics, plans are underway worldwide for new neutrino detectors to study open issues such as the hierarchy of neutrino masses, the masses themselves, the extent of CP violation in the lepton sector, the Majorana or Dirac nature of neutrinos, etc. This involves R&D efforts for producing intense beams of neutrinos at GeV energies, suitable detectors to detect them at long-baseline distances, and sensitive neutrinoless double beta decay experiments. A complementary approach to these is the use of atmospheric neutrinos, whose fluxes are more uncertain than beam neutrinos, but which provide a wider range of energies, and more importantly, a wider range of baselines.

The INO is one such proposal aiming to address some of the challenges in understanding the nature of

neutrinos, using atmospheric neutrinos as the source. The unique feature of ICAL, the main detector in INO, will be its ability to distinguish neutrinos from antineutrinos, which enables a clearer distinction between the matter effects on neutrinos and antineutrinos travelling through the Earth, leading to the identification of neutrino mass hierarchy. In this section, we shall introduce the INO laboratory, the ICAL detector, and describe the role of such a detector in the global context of neutrino physics experiments.

1.1 *The ICAL detector at the INO facility*

1.1.1 *Neutrino experiments in India: Past and present*. Underground science in India has a long history. The deep underground laboratory at KGF, where Indian scientists conducted many front-ranking experiments in the field of cosmic rays and neutrinos, was a pioneering effort. The KGF mines are situated at about 870 m above sea level near the city of Bengaluru in South India. It has a flat topography around the area surrounding the mines. The mines have extended network of underground tunnels which permitted experiments up to a depth of 3000 m below the surface. Initially, attempts were made to find the depth variation of muon fluxes starting from the surface up to the deepest reaches. The absence of any count around a depth of 8400 hg/cm^2 leads to the conclusion that the atmospheric muon intensity is attenuated to such a level where one could search for very weak processes like the interactions of high-energy neutrinos. This was in the beginning of the sixties when very little was known about the interaction of neutrinos at high energies (>a few GeV) from accelerators, and that too with only muon neutrino beams. Nothing was known about the electron neutrino or antineutrino interactions.

Thus began the neutrino experiments in KGF in the early sixties, conducted by a collaboration consisting of groups from Durham University (UK), Osaka City University (Japan), and TIFR in India. The techniques used were perfected during the years of muon experiments and involved a basic trigger with scintillation counters and neon flash tubes (NFT) for tracking detectors initially. Seven such detectors were placed in a long tunnel at a depth of 2.3 km, in the Heathcote shaft of Champion reef mines, in three batches over a period of two years starting from the end of 1964 [42].

The first ever atmospheric neutrino event recorded underground was in early 1965 [21]. Two well-defined tacks emerging from the rock in an upward direction indicated unambiguously a clear inelastic neutrino event. Later, this collaboration put together the first experiment that searched for proton decay. Nature did not oblige and experiments are still looking for proton decay. The KGF laboratory operated for nearly four decades, almost till the end of 1980s, collecting data on atmospheric muon and neutrino interactions at various depths, starting from about 300 m all the way down to 2700 m. In the process they also detected some anomalous events which could not be attributed to neutrinos at depths around 2000 m [43–45]. Such events have neither been proved wrong nor have they been confirmed by other experiments.

The INO project, the discussions about which were formally held first in the Workshop on High Energy Physics Phenomenology (WHEPP-VI) in Chennai [46], is an ambitious proposal to recapture this pioneering spirit and do experiments in neutrino physics at the cutting edge. The immediate goal of INO project is the creation of an underground laboratory which will house a large magnetized iron calorimeter (ICAL) detector to study the properties of naturally produced neutrinos in the Earth's atmosphere. Apart from experiments involving neutrinos, in the long term, the laboratory is envisaged to develop into a full-fledged underground laboratory for studies in physics, biology, and geology as well. The INO is the first basic science laboratory planned on such a large scale in India.

1.1.2 *Location and layout of the INO*. The INO will be located at the Bodi West Hills (BWH), near Pottipuram village, in the Theni district of Tamil Nadu, India. The site has been chosen both for geotechnical reasons as well as from environmental considerations. It is near the historic city of Madurai, as shown in figure 1.1. Madurai is about 120 km from the INO site, and will also be the location for the Inter-Institutional Centre for High Energy Physics (IICHEP), where activities related to the INO will be carried out. The figure shows the location and also the features of the local terrain. The construction of the laboratory below the Bodi Hills involves building a horizontal tunnel, approximately 1900 m long, to reach the laboratory that is located under a mountain peak. One large and three small laboratory caverns are to be built with a rock burden of 1000 m or more all around (with a vertical overburden of $\sim$1300 m) to house the experiments. The reduction of cosmic ray background at this site is almost the same as at the Gran Sasso Laboratory, as can be seen from the bottom right panel, which shows the cosmic ray muon flux as a function of depth, with the locations of other major laboratories.

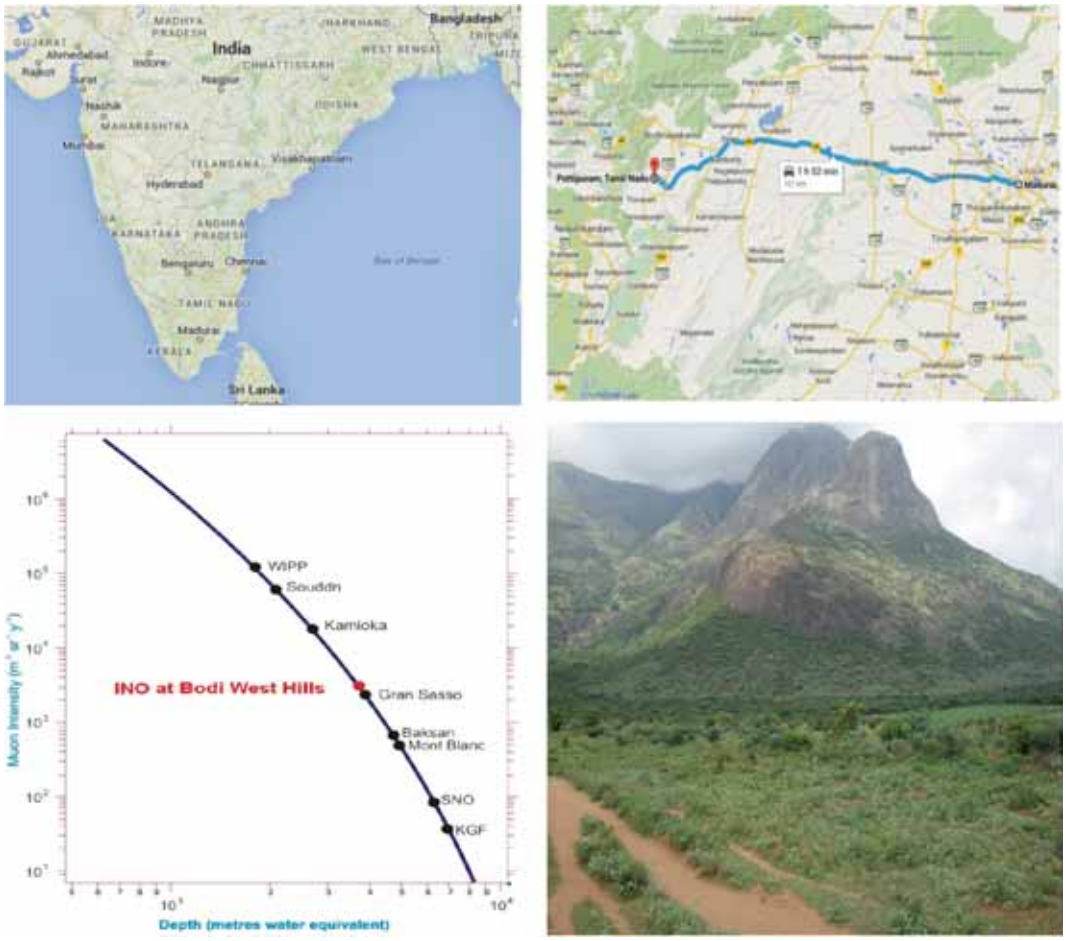

Figure 1.1. The location of the INO site and the nearby major landmarks. The IICHEP is located about 120 km east of the INO site, in the city of Madurai, as shown in the top right panel. The photo in the bottom right panel shows the view of the hill under which the cavern will be located. The terrain is totally flat with minimal undergrowth as seen in the picture (Photo: M V N Murthy). The photo is taken before the start of any construction. The bottom left panel shows the suppression in intensity of atmospheric muon flux at various underground sites, compared to the INO cavern [2].

In addition to the main iron calorimeter (ICAL) detector whose prime goal is the determination of the neutrino mass hierarchy, the laboratory is designed to accommodate experiments in other areas like neutrinoless double beta decay, dark matter search, low-energy neutrino spectroscopy, etc. Preliminary investigations and R&D in this direction are in progress. The special environment provided by the underground laboratory may also be useful to conduct experiments in rock mechanics, geology, biology etc.

The present configuration of the laboratory caverns is shown in figure 1.2. The largest cavern that will house the main iron calorimeter detector (ICAL) is 132 m (L) × 26 m (W) × 32.5 m (H). This cavern, called 'UG-Lab 1', is designed to accommodate a 50 kt ICAL (planned) and a second possible ICAL-II neutrino detector of equal size. Each ICAL consists of three modules with dimensions of 16 m (L) × 16 m (W) × 14.5 m (H), so that the total footprint of both the detectors would be 96 m (L) × 16 m (W). Figure 1.2 shows three modules of the 50 kt ICAL.

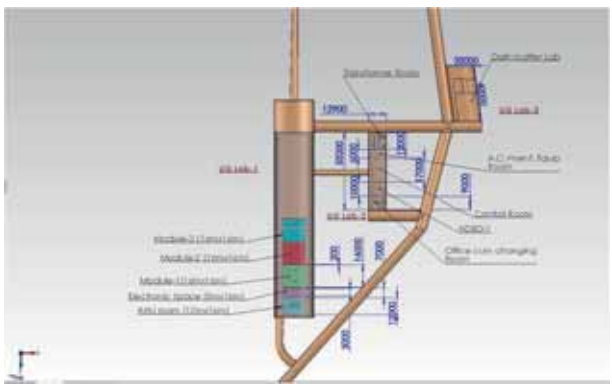

Figure 1.2. The layout of the underground caverns showing footprints of the proposed experiments and other components.

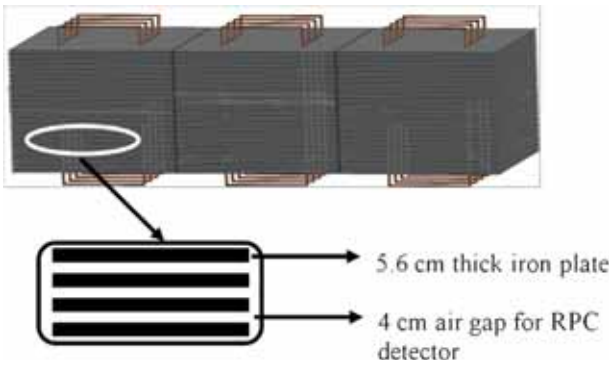

Figure 1.3. Schematic view of the 50 kt ICAL detector.

1.1.3 *The ICAL detector*. The ICAL detector is similar in concept to the earlier proposed Monolith [47,48] detector at Gran Sasso. The layout of the proposed ICAL detector is shown in figure 1.3. The detector will have a modular structure of total lateral size 48 m × 16 m, subdivided into three modules of area 16 m × 16 m. It will consist of a stack of 151 horizontal layers of 5.6 cm thick magnetized iron plates interleaved with 4 cm gaps to house the active detector layers, making it 14.5 m high. Iron spacers acting as supports will be located every 2 m along both X and Y directions; the 2 m wide roads along the transverse (Y) direction will enable the insertion and periodic removal of RPCs, when required.

The active detector elements, the resistive plate chambers (RPCs) made up of a pair of 3 mm thick glass plates of 2 m × 2 m area separated by 2 mm spacers, will be inserted in the gaps between the iron layers. These will be operated at a high voltage of about 10 kV in avalanche mode. A high-energy charged particle, passing through the RPCs, will leave signals that will be read by orthogonal X and Y pickup strips, about 3 cm wide, one on each side of an RPC. Detailed R&D has shown that the RPCs have an efficiency of around 90–95% with a time resolution of about a nanosecond. This will allow the determination of the X and Y coordinates of the track of the charged particles passing through the RPC. The layer number of the RPC will provide the Z coordinate. The observed RPC time resolution of ∼1 ns will enable the distinction between upward-going particles and downward-going particles. From the hit pattern observed in the RPCs, the energies as well as directions of the charged particles produced in the neutrino interactions can be reconstructed.

Each module will have two vertical slots cut into it to enable current-carrying copper coils to be wound around as shown in figure 1.3. Simulation studies [49] have shown that the iron plates can be magnetized to a field strength of about 1.5 T, with fields greater than 1 T over at least 85% of the volume of the detector. The bending of charged particles in this magnetic field will enable the identification of their charge. In particular, the sign of the charge of the muon produced by neutrino interactions inside the detector will help in identifying and studying the ν_μ- and $\bar{\nu}_\mu$-induced events separately. The magnetic field will also help measuring the momentum of the final-state particles, especially the muons.

With about 14,000 iron plates of 2 m × 4 m area and 5.6 cm thickness, 30,000 RPCs of 2 m × 2 m area, 4,000,000 electronic readout channels, and a magnetic field of 1.5 T, the ICAL is going to be the largest electromagnet in the world, and is expected to play a pivotal role in our understanding of neutrino properties.

1.2 *Role of ICAL in neutrino mixing and beyond*

In this section, we briefly discuss our present understanding of neutrino oscillation parameters and identify the fundamental issues in the neutrino sector that can be addressed by the ICAL detector.

1.2.1 *Current status of neutrino mixing parameters*. The neutrino flavour states $|\nu_\alpha\rangle$ (where $\alpha = e, \mu, \tau$) are linear superpositions of the neutrino mass eigenstates $|\nu_i\rangle$ (with $i = 1, 2, 3$), with masses m_i:

$$|\nu_\alpha\rangle = \sum_i U_{\alpha i} |\nu_i\rangle. \tag{1.1}$$

Here U is the 3 × 3 unitary mixing matrix. A physically motivated form of the mixing matrix that is conventionally used is [50–52]

$$U = \begin{pmatrix} c_{12}c_{13} & s_{12}c_{13} & s_{13}e^{-i\delta} \\ -c_{23}s_{12} - s_{23}s_{13}c_{12}e^{i\delta} & c_{23}c_{12} - s_{23}s_{13}s_{12}e^{i\delta} & s_{23}c_{13} \\ s_{23}s_{12} - c_{23}s_{13}c_{12}e^{i\delta} & -s_{23}c_{12} - c_{23}s_{13}s_{12}e^{i\delta} & c_{23}c_{13} \end{pmatrix},$$

where $c_{ij} = \cos\theta_{ij}$, $s_{ij} = \sin\theta_{ij}$ and δ denotes the CP-violating (Dirac) phase, also called $\delta_{\rm CP}$. Note that the Majorana phases are not included in the above parametrization, because they do not play a role in neutrino oscillation experiments.

The probability of an initial neutrino ν_α of flavour α and energy E being detected as a neutrino ν_β of the same energy but with flavour β after travelling a distance L in vacuum is

$$P_{\alpha\beta} = \delta_{\alpha\beta} - 4\sum_{i>j} \mathrm{Re}[U_{\alpha i}U^*_{\beta i}U^*_{\alpha j}U_{\beta j}]\sin^2(\Delta_{ij}) + 2\sum_{i>j} \mathrm{Im}[U_{\alpha i}U^*_{\beta i}U^*_{\alpha j}U_{\beta j}]\sin(2\Delta_{ij}), \quad (1.2)$$

where $\Delta_{ij} = 1.27\Delta m^2_{ij}(\mathrm{eV}^2)\times L(\mathrm{km})/E(\mathrm{GeV})$, with $\Delta m^2_{ij} = m^2_i - m^2_j$ the mass squared differences between the ith and the jth neutrino mass eigenstates. Oscillation measurements are not sensitive to the individual neutrino masses, but only to their mass-squared differences. Note that the above expression is valid only for propagation through vacuum. In matter, the probabilities are drastically modified. The relevant expressions may be found in Appendix B.

The neutrino flavour conversion probabilities can be expressed in terms of the two mass squared differences, the three mixing angles, and the single CP-violating phase. Also of crucial importance is the 'mass ordering', i.e., the sign of Δm^2_{32} (the same as the sign of Δm^2_{31}). While we know that Δm^2_{21} is positive so as to accommodate the observed energy dependence of the electron neutrino survival probability in solar neutrino experiments, at present Δm^2_{32} is allowed to be either positive or negative. Hence, it is possible to have two patterns of neutrino masses: $m_3 > m_2 > m_1$, called normal ordering, where Δm^2_{32} is positive, and $m_2 > m_1 > m_3$, called inverted ordering, where Δm^2_{32} is negative. Determining the sign of Δm^2_{32} is one of the prime goals of the ICAL experiment. Note that, though the 'mass ordering' is perhaps the more appropriate term to use in this context, the more commonly used term in literature is 'mass hierarchy'. In this report, therefore, we shall use the notation 'normal hierarchy' (NH) to denote normal ordering, and 'inverted hierarchy' (IH) to denote in*v*erted ordering. The word 'hierarchy' used in this context has no connection with the absolute values of neutrino masses.

Table 1.1 summarizes the current status of neutrino oscillation parameters [53,54] based on the world neutrino data that was available after the NOW 2014 conference. The numbers given in table 1.1 are obtained by keeping the reactor fluxes free in the fit and also including the short-baseline reactor data with $L \leq 100$ m [53,54].

Table 1.1 also provides the relative 1σ precision on the measurements of these quantities at this stage (here the 1σ precision is defined as 1/6th of the $\pm 3\sigma$ variations around the best-fit value). The global fit suggests the best-fit value of $\Delta m^2_{21} = 7.5 \times 10^{-5}$ eV^2 with a relative 1σ precision of 2.4%. In a three-flavour framework, we have the best-fit values of $\Delta m^2_{31} = 2.42 \times 10^{-3}$ eV^2 for NH and $\Delta m^2_{32} = -2.41 \times 10^{-3}$ eV^2 for IH. A relative 1σ precision of 2.5% has been achieved for the atmospheric mass-squared splitting.

As far as the mixing angles are concerned, θ_{12} is now pretty well measured with a best-fit value of $\sin^2\theta_{12} = 0.3$ and a relative 1σ precision of 4% has been achieved for the solar mixing angle. Our understanding of the atmospheric mixing angle θ_{23} has also

Table 1.1. The values of neutrino oscillation parameters used for the analyses in [53]. The second column shows the central values of the oscillation parameters. The third column depicts the 3σ ranges of the parameters with the relative 1σ errors being listed in the last column. Note that the parameter Δm^2_{31} (Δm^2_{32}) is used while performing the fit with normal (inverted) hierarchy. The current best-fit values and allowed ranges of these parameters may be found in [54–56].

Parameter	Best-fit values	3σ ranges	Relative 1σ precision
Δm^2_{21} (eV^2)	7.5×10^{-5}	$[7.0,\ 8.1] \times 10^{-5}$	2.4%
Δm^2_{31} (eV^2)	2.46×10^{-3} (NH)	$[2.32,\ 2.61] \times 10^{-3}$ (NH)	2.0%
Δm^2_{32} (eV^2)	-2.45×10^{-3} (IH)	$-[2.59,\ 2.31] \times 10^{-3}$ (IH)	1.9%
$\sin^2\theta_{12}$	0.3	[0.27, 0.34]	4.4%
$\sin^2\theta_{23}$	0.45 (NH), 0.58 (IH)	[0.38, 0.64]	8.7%
$\sin^2\theta_{13}$	0.022	[0.018, 0.025]	5.3%
$\delta_{\rm CP}$ (°)	306	[0, 360]	–

improved a lot in recent years. Combined analysis of all the neutrino oscillation data available so far disfavours the maximal mixing solution for θ_{23} at $\sim 1.5\sigma$ confidence level [53,54,57–59]. This result is mostly governed by the MINOS accelerator data in ν_μ and $\bar{\nu}_\mu$ disappearance modes [60]. The dominant term in ν_μ survival channel mainly depends on the value of $\sin^2 2\theta_{23}$. Now, if $\sin^2 2\theta_{23}$ turns out to be different from 1 as suggested by the recent oscillation data, then it gives two solutions for $\sin^2 \theta_{23}$: one whose value is less than half, known as the lower octant (LO) solution and the other whose value is greater than half, known as the higher octant (HO) solution. This creates the problem of octant degeneracy of θ_{23} [61]. At present, the best-fit value of $\sin^2 \theta_{23}$ in LO (HO) is 0.45 (0.58) assuming NH (IH). The relative 1σ precision on $\sin^2 \theta_{23}$ is around 8.7% assuming maximal mixing as the central value. Further improvement in the knowledge of θ_{23} and settling the issue of its octant (if it turns out to be non-maximal) are also important issues that can be addressed by observing atmospheric neutrinos.

For many years, we only had an upper bound on the value of the 1–3 mixing angle [62–65]. A non-zero value for this angle has been discovered rather recently [35–37,66,67], with a moderately large best-fit value of $\sin^2 \theta_{13} = 0.022$, which is mostly driven by the high-statistics data provided by the ongoing Daya Bay reactor experiment [37,67]. It is quite remarkable that already we have achieved a relative 1σ precision of 5.3% on $\sin^2 \theta_{13}$. On the other hand, the whole range of $\delta_{\rm CP}$ is still allowed at the 3σ level.

1.2.2 *Unravelling three-neutrino mixing with ICAL.* As has been discussed earlier, the main advantage of a magnetized iron calorimeter is its ability to distinguish μ^+ from μ^-, and hence to study ν_μ and $\bar{\nu}_\mu$ separately. This allows a cleaner measurement of the difference in the matter effects experienced by neutrinos and antineutrinos. However, this difference depends on the value of θ_{13}. The recent measurement of a moderately large value of θ_{13} therefore boosts the capability of ICAL for observing these matter effects, and hence its reach in addressing the key issues related to the neutrino masses and mixing. In this section, we shall highlight the role that an iron calorimeter like ICAL will have in the context of global efforts to measure neutrino mixing parameters.

The moderately large θ_{13} value has opened the door to the fundamental measurements of (i) the neutrino mass ordering, (ii) the deviation of 2–3 mixing angle from its maximal value and hence the correct octant of θ_{23}, and (iii) the CP phase $\delta_{\rm CP}$ and to look for CP violation in the lepton sector, for several experiments which would have had limited capability to address these questions had this parameter been significantly smaller. Central to all these measurements are effects which differ between neutrinos and antineutrinos. These could either be matter-related effects which enhance or suppress the oscillation probabilities (relevant for (i) and (ii) above), or those induced by a non-zero value of $\delta_{\rm CP}$ (relevant for (iii)). The ICAL will be sensitive to the matter effects, but will have almost no sensitivity to the actual value of $\delta_{\rm CP}$.

Prior to summarizing the role of ICAL, it is useful to mention several other experiments which are underway or will come online in the next couple of decades with the aim of making the three important measurements mentioned above. The T2K experiment has observed electron neutrino appearance in a muon neutrino beam [66], thus showing a clear evidence of neurino oscillations. The accelerator-based long-baseline beam experiments NOνA [68–70] has already started taking data that will be sensitive to mass hierarchy, and the first results have been presented [41]. The IceCube DeepCore experiment has also recently [71] published their results on atmospheric neutrino oscillations. Future large atmospheric neutrino detectors on the cards are Hyper-Kamiokande (HK) [72], Precision IceCube Next-Generation Upgrade (PINGU) [73] and Oscillation Research with Cosmics in the Abyss (ORCA) [74]. The Deep Underground Neutrino Experiment (DUNE) [75], a combined initiative of the earlier Long-Baseline Neutrino Experiment (LBNE) [76,77] and Long-Baseline Neutrino Oscillation (LBNO) [78–80] Collaborations, is also slated to aim at the mass hierarchy identification. Additionally, the medium-baseline reactor oscillation experiments [81], JUNO [82], and RENO-50 [83] aim to determine the hierarchy by performing a very precise, high statistics measurement of the neutrino energy spectrum. The CP phase $\delta_{\rm CP}$ can be measured (in principle) by accelerator experiments like T2K [84,85], NOνA [85–88], T2HK [72], and DUNE [75]. These experiments, if they run in both the neutrino and the antineutrino modes, would additionally be sensitive to the octant of θ_{23} [89,90], and so would the large-mass atmospheric experiments like ICAL [14] and Hyper-K [91].

The ICAL detector at the INO cavern will provide an excellent opportunity to study atmospheric neutrinos and antineutrinos separately with high detection efficiency and good enough energy and angular resolutions in the multi-GeV range in the presence of the Earth's matter effect. There is no doubt that the

rich dataset which would be available from the proposed ICAL atmospheric neutrino experiment will be extremely useful to validate the three-flavour picture of the neutrino oscillation taking into account the Earth's large matter effect in the multi-GeV range. The first aim of the ICAL detector would be to observe the oscillation pattern over at least one full period, in order to make a precise measurement of the atmospheric oscillation parameters. The ICAL detector performs quite well in a wide range of L/E and can confirm the evidence of the sinusoidal flavour transition probability of neutrino oscillation already observed by the Super-Kamiokande detector by observing the dips and peaks in the event rate vs. L/E [92], as well as by the IceCube DeepCore [71]. In the case of Super-Kamiokande, the sub-GeV events have played an important role to perform this L/E analysis, while for IceCube the very high energy events ($E \gtrsim 10$ GeV) have contributed significantly. The ICAL detector is sensitive mainly to the energy range 1–10 GeV, which fills the gap between the other two large Cherenkov detectors. In its initial phase, the ICAL experiment will also provide an independent measurement of θ_{13} by exploring the Earth's matter effect using the atmospheric neutrinos. This will certainly complement the ongoing efforts of the reactor and the accelerator experiments to learn about the smallest lepton mixing angle θ_{13}.

The relevant neutrino oscillation probabilities that the ICAL will be sensitive to are: $P_{\mu\mu}$, $P_{\bar{\mu}\bar{\mu}}$, $P_{e\mu}$, and $P_{\bar{e}\bar{\mu}}$, especially the first two. These probabilities have rich structures for neutrinos and antineutrinos at GeV energies, travelling through the Earth for a distance of several thousands of km (for a detailed description, see Appendix B). The matter effects on these neutrinos and antineutrinos lead to significant differences between these oscillation probabilities, which may be probed by a detector like ICAL that can distinguish neutrinos from antineutrinos. This feature of ICAL would be instrumental in its ability to distinguish between the two possible mass hierarchies.

Detailed simulations of the ICAL detector performance, as discussed in the following sections, show that ICAL will be an excellent tracker for muons. The energy and direction of a muon would also be reconstructed rather accurately, with the muon direction resolution of better than a degree at high energies. Furthermore, the capability of ICAL to study the properties of the final-state hadrons in multi-GeV neutrino interactions will be one of its unique features. This will allow the reconstruction of the neutrino energy in every event, albeit with large error. (Note that the extraction of hadronic information at multi-GeV energies in currently running or upcoming water or ice-based atmospheric neutrino detectors is quite challenging; the efficiency of reconstruction of multiring events is rather small in such detectors.) As a result, the ICAL would have a significant stand-alone sensitivity to the mass hierarchy, which, when combined with data from experiments like NOνA and T2K, will significantly enhance the overall sensitivity to this important quantity.

Although the ICAL will not be sensitive to the value of $\delta_{\rm CP}$, this very feature will make it an important supporting experiment for others that are sensitive to $\delta_{\rm CP}$, in a unique manner. Note that in experiments where event rates are sensitive simultaneously to both matter and CP phase effects, disentangling one from the other restricts the sensitivities to individual and unambiguous measurements of each of the three quantities (i), (ii), and (iii) mentioned above. The virtue of ICAL here will lie in its ability to offer a dataset that is free of entanglements between matter enhancements and dynamical CP-violating effects due to a non-zero $\delta_{\rm CP}$. Thus, when used in combination with other experiments, the ICAL measurements will facilitate the lifting of degeneracies which may be present otherwise. In particular, the ICAL data, when combined with that from NOνA and T2K, will make a significant difference to their discovery potential of CP violation [19].

1.2.3 *Addressing new physics issues with ICAL.* The complete role of an iron calorimeter in the global scenario of neutrino physics is rich and complex. In addition to what is described here, it can add to our knowledge on very high-energy muons [93,94] on hitherto undiscovered long-range forces [95], on CPT violation [15,96] and on non-standard interactions [97], among other issues. The future of neutrino physics is, in our opinion, crucially dependent on the synergistic combination of experiments with differing capabilities and strengths. A large iron calorimeter brings in unique muon charge identification capabilities and an event sample independent of the CP phase. Both these aspects will play important roles in our concerted global effort to understand the mysteries of neutrino physics and consequently understand physics beyond the Standard Model.

Though the ICAL has been designed mainly with neutrino physics in view, it is expected that many non-neutrino issues may find relevance with this detector. For example, a few decades ago, both in the cosmic ray neutrino experiments [43,44] and later in the

proton decay experiment [45] at KGF in South India, some unusual events were seen. These so-called Kolar events were multitrack events with some unusual features which could not be explained away by any known processes of muons or neutrinos. Recently, it has been speculated that such events may be caused by the decay of unstable cold dark matter particles with mass in the range of 10 GeV with a lifetime approximately equal to the age of the Universe [98]. Such an interpretation may be easily tested with ICAL at INO, even without further modifications [99]. Signals of dark matter annihilation inside the Sun can also be detected at ICAL. The possible observation of GUT monopoles is another such issue that can be addressed at ICAL with its current set-up.

2. Atmospheric neutrino fluxes

Everything is in a state of flux, Even the status quo.
–Robert Byrne

2.1 *Introduction to atmospheric neutrinos*

Atmospheric neutrinos are produced in the interactions of cosmic ray with the nuclei of air molecules in the atmosphere. The first report of cosmic ray-induced atmospheric neutrinos was from the deep underground laboratories at KGF in India by TIFR, Osaka University, and Durham University [21], and immediately afterwards by Reines *et al* [22] in an experiment conducted in South African mines in 1965. Atmospheric neutrinos have been studied since then in several other underground laboratories, and important discoveries such as the evidence for neutrino oscillations [27], have been made. We shall briefly review the atmospheric neutrinos in this section.

Primary cosmic rays are high-energy particles impinging on the Earth from galactic and extragalactic sources. Their origins are still clouded in mystery. In the GeV energy range, the cosmic ray particles are mainly made up of protons and about 9% helium nuclei, with a small fraction of heavy nuclei. Although the energy spectrum of cosmic rays extends to very high energies, beyond even 10^{10} GeV, it falls rapidly as energy increases. When cosmic rays enter the atmosphere, interactions with the nuclei in air molecules produce secondary particles. These secondary particles are mainly pions with a small admixture of kaons. These mesons decay mainly to muons and their associated neutrinos following the decay chain

$$\pi^{\pm} \to \mu^{\pm} + \nu_{\mu}(\bar{\nu}_{\mu}),$$
$$\mu^{\pm} \to e^{\pm} + \bar{\nu}_{\mu}(\nu_{\mu}) + \nu_{e}(\bar{\nu}_{e}). \quad (2.1)$$

Kaons also decay in a similar manner producing the two neutrino flavours, but their contribution to the atmospheric neutrino flux is small compared to the pions for neutrinos of a few GeV. We call the neutrinos produced in this manner as atmospheric neutrinos. It may be noted that only the ν_e and ν_μ neutrinos, along with their antiparticles, are produced in the atmosphere. The flux of ν_τ requires the production of mesons with heavy quarks, and as a result their flux is extremely small and we do not consider these neutrinos here. A schematic illustration of this cascading neutrino production is shown in figure 2.1.

From eq. (2.1) it is clear that the ratio

$$R = \frac{\Phi(\nu_\mu) + \Phi(\bar{\nu}_\mu)}{\Phi(\nu_e) + \Phi(\bar{\nu}_e)} \approx 2, \quad (2.2)$$

where Φ denotes the flux of neutrinos. The ratio is only approximate, because at high energies, muon may not decay before reaching the surface of the Earth. It, however, remains greater than 2, which may be observed from figure 2.2. The figure displays the direction-integrated neutrino fluxes in various models, as well as the ratios of fluxes of different kinds of neutrinos.

An important property of the atmospheric neutrino flux is that it is symmetric about a given direction on the surface of the Earth, that is

$$\Phi_\nu(E, \cos\theta) = \Phi_\nu(E, -\cos\theta), \quad (2.3)$$

where θ is the zenith angle. This result is robust above 3 GeV, though at lower energies the geomagnetic effects result in deviations from this equality. Therefore, at higher energies, any asymmetry in the fluxes of the upward-going and downward-going neutrinos can be

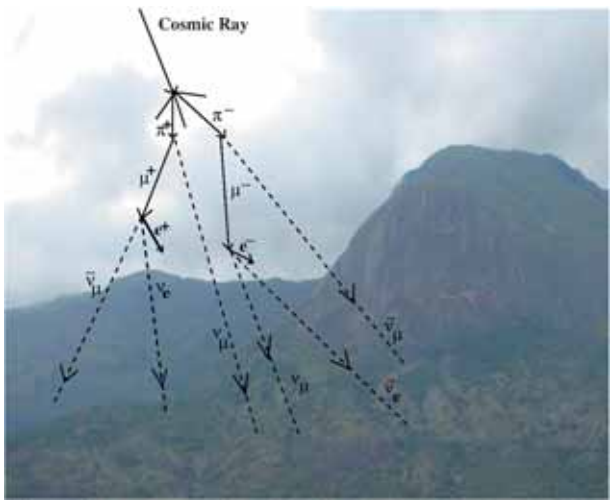

Figure 2.1. A schematic illustration of the production of neutrinos due to cosmic rays.

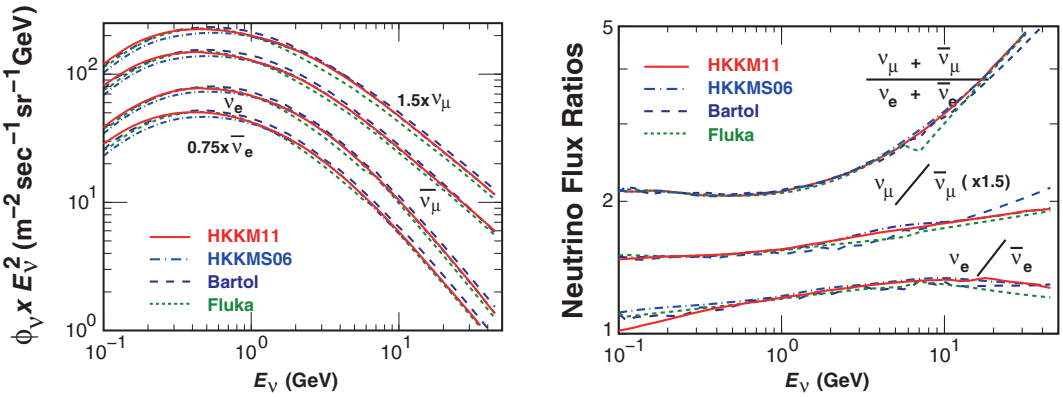

Figure 2.2. The direction integrated neutrino fluxes in various models are shown on the left panel. The ratios of fluxes of different neutrino species as functions of energy are shown on the right panel. Figures are reproduced from Honda *et al* [5], based on the analysis of cosmic ray neutrino fluxes from [100], [101] and [102].

attributed to the flavour changes during propagation. Even at lower energies, large deviations from the above equality are not expected, except from neutrino oscillations. This up–down asymmetry is thus the basis of atmospheric neutrino analysis, and it was effectively used by the Super-Kamiokande Collaboration to establish the first confirmed signal of neutrino oscillations [27]. Of course detailed analyses need the calculations of atmospheric neutrino fluxes as functions of energies, zenith angles as well as azimuthal angles.

The atmospheric neutrinos not only provide neutrinos in two distinct flavours, but also over a whole range of energies from hundreds of MeV to TeV and beyond. Yet another advantage over the conventional accelerator neutrino beams is the fact that the atmospheric neutrinos traverse widely different distances in different directions: from ∼10 km on the way downwards to more than 12000 km on the way upwards through the centre of the Earth. They also traverse matter densities varying from very small (essentially air) to almost 13 g/cc when passing through the Earth's core.

These facts make the analysis of atmospheric neutrinos not only interesting but also unique. The ICAL is expected to exploit the advantages of the freely available atmospheric neutrino flux, not only to explore the neutrino oscillation parameters but also to determine the hierarchy of neutrino masses, and perhaps probe new physics.

2.2 *Calculations of atmospheric neutrino fluxes*

The neutrino oscillation studies with atmospheric neutrinos can be put on a firm foundation provided the atmospheric neutrino flux estimates and their interaction cross-sections are known as precisely as possible. The main steps in the determination of atmospheric neutrino fluxes are:

- The energy spectrum of primary cosmic rays: The flux of primary cosmic rays decreases approximately as $E^{-2.7}$ in the 10 GeV to TeV region. Consequently, the flux of neutrinos decreases rapidly in the high-energy region. The flux of cosmic rays outside the atmosphere is isotropic and constant in time. These are measured experimentally up to tens of GeV. The primary spectrum of cosmic ray protons can be fitted to a form

$$\Phi(E) = K[E + b\exp(-c\sqrt{E})]^{-\alpha}, \qquad (2.4)$$

  where $\alpha = 2.74$, $K = 14900$, $b = 2.15$, $c = 0.21$ [103].
- The energy spectrum of secondary muons: The interactions of primary cosmic rays with the air nuclei produce pions and kaons, which in turn yield muons. An important input needed for this calculation is the hadronic cross-sections. These are well measured in accelerator experiments from low energy up to hundreds of GeV. Beyond the range of accelerator energies, these cross-sections are model-dependent. Hence, the composition of the secondary cosmic rays and their energy spectrum are well known up to TeV energies. The muons are produced by the decay of these mesons.
- The energy spectrum of neutrinos: This needs modelling the altitude dependence of interactions in the atmosphere, the geomagnetic effect on the flux of cosmic rays and secondaries, and the longitudinal dependence of extensive air showers.

Uncertainties in each one of the above steps limit the precision in the determination of neutrino fluxes on the

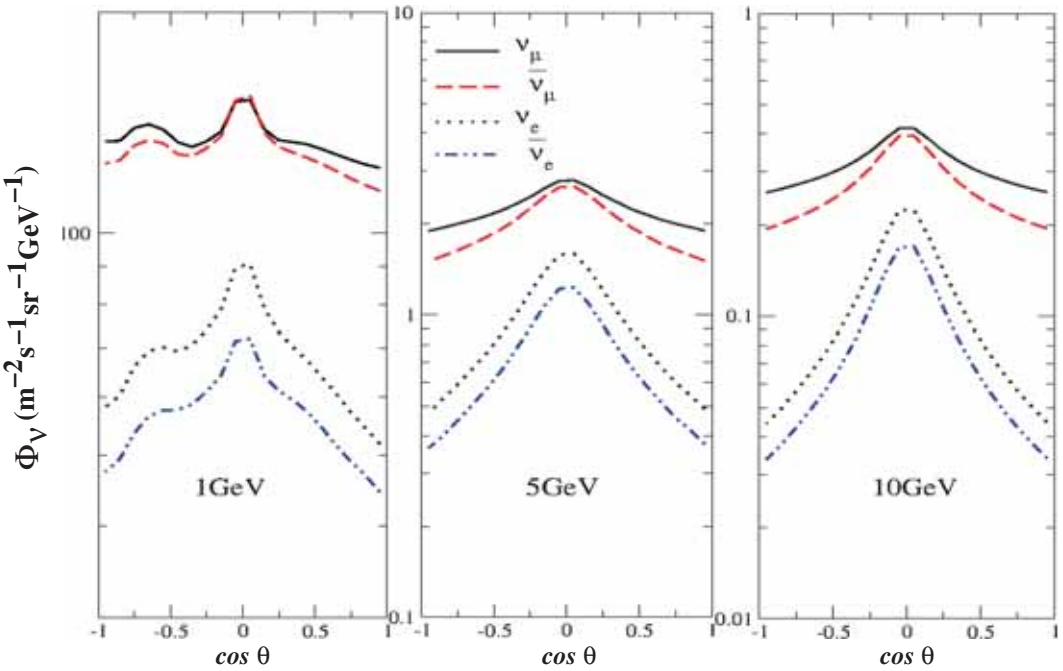

Figure 2.3. Zenith angle dependence of the neutrino flux averaged over azimuthal angles are shown for three different energies. This has been calculated for the Kamioka location. Figures are taken from Honda *et al* [104]. Note that the flux scales are different for different energies.

surface. Typically, these introduce an uncertainty of the order of 15–20% in the overall normalization.

Some typical features of the zenith angle distributions of atmospheric neutrino fluxes may be seen in figure 2.3, which show the fluxes (averaged over azimuthal angles) for three neutrino energies, calculated for Kamioka, the location of the Super-Kamiokande detector. The figure shows that the flux is typically maximum near $\cos\theta = 0$, i.e. for horizontal neutrinos, where the muons have had the maximum proper time to decay. Also, the ratio of muon to electron neutrino flux is observed to increase at higher energies and at more vertical (down-going or up-going) neutrinos, where muons have less proper time to decay, and so the second reaction in eq. (2.1) is less efficient. It can also be seen that when $E > 3$ GeV, the fluxes are essentially symmetric in zenith angle. However, at lower energies, there is some asymmetry, arising mainly from the bending of muons in the geomagnetic field.

Recently, Honda *et al* [105] have calculated the atmospheric neutrino spectrum at the INO location (Theni). It is observed that the total flux at INO is slightly smaller than that at Kamioka at low energies ($E \lesssim 3$ GeV), but the difference becomes small with the increase in neutrino energy. Also, at low energies ($E \sim 1$ GeV), the up–down asymmetries are larger at the INO site. These asymmetries decrease with the increase in neutrino energy. Detailed characteristics of these fluxes have been given in Appendix A. The analyses presented in this report use fluxes at the Kamioka location. We plan to use the recently compiled fluxes [104,105] for the Theni site in our future analysis.

3. The ICAL simulation framework

A good simulation · · · gives us
a sense of mastery over experience.
Heinz R Pagels

The broad simulation framework for the ICAL, starting with event generation, is indicated schematically in table 3.1. The events in the detector are generated using the NUANCE Monte Carlo generator [4]. This uses the atmospheric neutrino fluxes as described in §2 along with various possible neutrino–nucleus interaction cross-sections to generate the vertex and the energy–momentum of all final states in each event; these are then propagated through the virtual ICAL detector using the GEANT4 simulation tool. The GEANT4 simulates the propagation of particles through the detector, including the effects of the

Table 3.1. The simulation framework as implemented in the ICAL simulation package.

NUANCE	**Neutrino Event Generation** $\nu_\ell + N \to \ell + X$. Generates particles that result from a random interaction of a neutrino with matter using theoretical models for both neutrino fluxes and cross-sections.	**Output:** (i) Reaction channel (ii) Vertex and time information (iii) Energy and momentum of all final-state particles
GEANT	**Event Simulation** $\ell + X$ through simulated ICAL. Simulates propagation of particles through the ICAL detector with RPCs and magnetic field.	**Output:** (i) x, y, z, t of the particles as they propagate through detector (ii) Energy deposited (iii) Momentum information
DIGITIZATION	**Event Digitization** (X, Y, Z, T) of final states on including noise and detector efficieny. Add detector efficiency and noise to the hits.	**Output:** (i) Digitized output of the previous stage
ANALYSIS	**Event Reconstruction** $(E, \vec{p})$ of ℓ, X (total hadrons) Fit the muon tracks using Kalman filter techniques to reconstruct muon energy and momentum; use hits in hadron shower to reconstruct hadron information.	**Output:** (i) Energy and momentum of muons and hadrons, for use in physics analyses.

iron, the RPCs, and the magnetic field. The information in the events is then digitized in the form of (X, Y, Z) coordinates of the hits in the RPCs and the timing corresponding to each of these 'hits'. This is the information available for the event reconstruction algorithms, which attempt, from the hit pattern, to separate the muon tracks from the showers generated by the hadrons, and reconstruct the energies and directions of these particles. The process is described in detail below.

3.1 *Neutrino interactions and event generation*

Neutrino and antineutrino interactions in the ICAL detector are modelled using NUANCE neutrino generator version 3.5 [4]. Some preliminary studies and comparisons have also been initiated using the GENIE neutrino generator [106], but are not a part of this Review. The interactions modelled in NUANCE include (i) quasielastic scattering (QE) for both charged and neutral current neutrino interactions with nucleons, which dominate below neutrino energies of 1 GeV, (ii) resonant processes (RES) with baryon resonance production mainly from neutrinos with energy between 1 and 2 GeV, (iii) deep inelastic scattering (DIS) processes with considerable momentum (squared) transfer from the neutrino to the target, with the nuclei breaking up into hadrons, which is the dominant contribution in the multi-GeV region, (iv) coherent nuclear processes on nuclei, and (v) neutrino–electron elastic scattering and inverse muon decay. These are the main neutrino interaction processes of relevance for our simulation framework, with the contribution of the last two being the least in the few GeV energy region of interest. A simple ICAL geometry has been described within NUANCE, including mainly the iron and glass components of the detector, as most of the interactions will occur in these two media. NUANCE identifies these bound nucleons (with known Fermi energies) differently from free nucleons and also applies final-state nuclear corrections.

The NUANCE generator calculates event rates by integrating different cross-sections weighted by the fluxes for all charged current (CC) and neutral current (NC) channels at each neutrino energy and angle. Some typical total cross-sections for different CC processes are illustrated in figure 3.1. Based on the interaction channel, there can be 10–40% uncertainty in cross-sections in the intermediate energy ranges [107].

As mentioned in §2, for the present we have used the Honda fluxes [5] generated at the location of Kamioka. This will be changed soon to that at the actual location of INO. We choose to generate only unoscillated neutrino events using NUANCE for the simulations, even though there is a provision for generating oscillated events in it. The oscillations are applied externally, separately in each analysis.

3.2 *Simulation of the ICAL detector*

We now describe the ICAL detector geometry within the GEANT4 [3] simulation framework. This includes the geometry itself, and the magnetic field map and the RPC characteristics that are inputs to the simulation.

3.2.1 *The detector geometry*. The simulations have been performed for the 50 kt ICAL detector, which has a modular structure with the detector consisting of three modules, each of size 16 m (length) × 16 m (width) × 14.5 m (height), with a gap of 20 cm between the modules. The ICAL coordinates are defined as

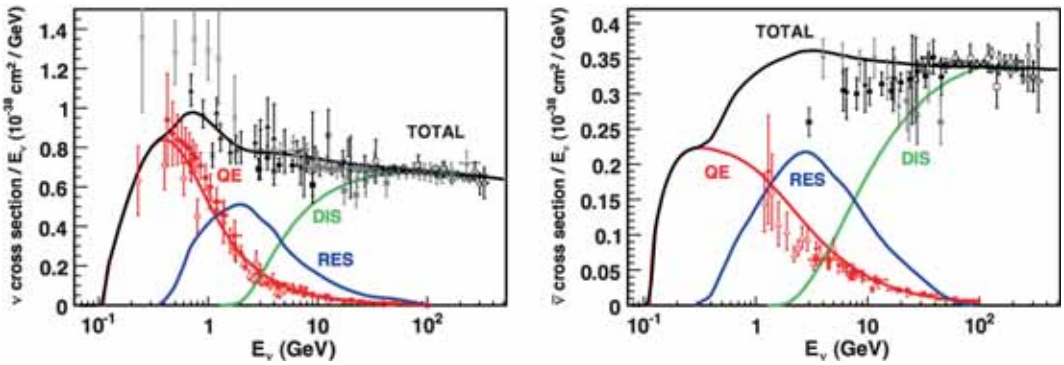

Figure 3.1. Muon neutrino (left) and muon antineutrino (right) total charged current cross-sections in cm^2/GeV, obtained from NUANCE, are shown (smooth lines) as a function of incident neutrino energy, E_ν, in comparison with the existing measurements of these cross-sections along with their errors [108]. Note that the y-axis scale of the two panels is different.

follows: The direction along which the modules are placed is labelled as the x-direction with the remaining horizontal transverse direction being labelled y. At present, x is also considered to coincide with south, because the final orientation of the INO cavern is not yet decided. The z-axis points vertically upwards so that the polar angle equals the zenith angle θ while the zero of the azimuthal angle ϕ points south. The origin is taken to be the centre of the second module. Each module comprises 151 horizontal layers of 5.6 cm thick iron plates. The area of each module is 16 m × 16 m, while the area of each iron plate is 2 m × 4 m. There is a vertical gap of 4 cm between the two layers. The iron sheets are supported every 2 m in both the x and y directions, by steel support structures. The basic RPC units have dimensions of 1.84 m × 1.84 m × 2.5 cm, and are placed in a grid format within the air gaps, with a 16 cm horizontal gap between them in both x and y directions to accommodate the support structures.

Vertical slots at $x = x_0 \pm 4$ m (where x_0 is the central x value of each module) extending up to $y = \pm 4$ m and cutting through all layers are provided to accommodate the four copper coils that wind around the iron plates, providing a magnetic field in the x–y plane, as shown in figure 3.2. The detector excluding the coils weighs about 52 kt, with 98% of this weight coming from iron where the neutrino interactions are dominantly expected to occur, and less than 2% from the glass of the RPCs. In the central region of each module, typical values of the field strength are about 1.5 T in the y-direction, as obtained from simulations using MAGNET6.26 software [109].

3.2.2 *The magnetic field.* Figure 3.2 depicts the magnetic field lines in the central iron plate near the centre of the central module. The arrows denote the direction of the magnetic field lines while the length of the arrows (and the shading) indicates the magnitude of the field. The maximum magnitude of the magnetic field is about 1.5 T. Notice that the field direction reverses on the two sides of the coil slots (beyond $x_0 \pm 4$ m) in the x-direction. In between the coil slots (an 8 m × 8 m square area in the x–y plane) the field is maximum and nearly uniform in both magnitude (to about 10%) and direction; we call this the 'central region'. Near the edges in the x-direction (outside the coil slots) the field is also fairly uniform, but in the opposite direction; this is called the 'side region'. Near the edges in the y-direction, i.e., in the regions 4 m $\leq |y| \leq$ 8 m, both the direction and magnitude of the magnetic field vary considerably; this region is labelled as the 'peripheral region'.

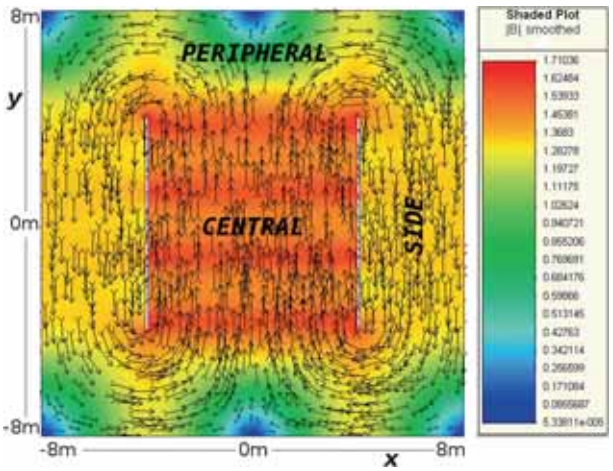

Figure 3.2. Magnetic field map in the central plate of the central module ($z = 0$), as generated by the MAGNET6 software. The length and direction of the arrows indicate the magnitude and direction of the field; the magnitude (in T) is also shown according to the colour-coding indicated on the right.

In our simulations, the field has been assumed to be uniform over the entire thickness of the iron plate at every (x, y) position, and has been generated in the centre of the iron plate, i.e., at $z = 0$. In the 4 cm air gap between the iron plates, the field is taken to be zero as it falls off to several hundred gauss in these regions, compared to more than 1 T inside the iron plates. The magnetic field is also taken to be zero in the (non-magnetic) steel support structures. These support structures, along with the coil slot, form the bulk of the dead spaces of the detector.

The side and peripheral regions are beset by edge effects as well as by non-uniform and lower magnetic field. We confine ourselves, in the present study, to tracks generated only in the central region (-4 m $\leq x - x_0 \leq 4$ m and -4 m $\leq y \leq 4$ m), although the particle may subsequently travel outside this region or even exit the detector.

3.2.3 *The resistive plate chambers.* In order to appreciate the hit pattern in the simulated detector, it is necessary to describe the active detector elements, the RPCs. These are glass chambers made by sealing two 3 mm thick glass sheets with a high DC voltage across them, with a uniform gap of 2 mm using plastic edges and spacers through which a mixture of R134A ($\sim$95%), isobutane, and trace amounts of SF_6 gas continually flows. In brief, the working principle of an RPC is the ionization of the gaseous medium when a charged particle passes through it. The combination of gases keeps the signal localized and the location is used to determine the trajectory of the charged particle in the detector. For more details, see ref. [110].

A 150 micron thick copper sheet is the component most relevant to the simulation and track reconstruction as it inductively picks up the signal when a charged particle traverses the chamber. This copper sheet is pasted on the 'inside' of a 5 mm thick foam (used for structural strength and electrical insulation) placed both above and below the glass chamber. It is pasted on the side of the foam facing the glass and is insulated from the glass by a few sheets of mylar. This layer is scored-through with grooves to form strips of 1.96 cm width in such a way that the strips above and below are transverse to each other, that is, in the x- and y-directions. (Note that the strip width in the current ICAL design is 3 cm. However this is subject to changes.) These pick-up strips thus provide the x and y location of the charged particle as it traverses the RPC while the RPC layer number provides the z information. A timing resolution of about 1.0 ns is assumed as also an efficiency of 95%, consistent with the observations of RPCs that have been built as a part of the R&D for ICAL [110].

3.3 *Event simulation and digitization*

Muons and hadrons, generated in neutrino interactions with the detector material, pass through dense detector material and an inhomogeneous magnetic field. Simulation of such particles through the detector geometry is performed by a package based on the GEANT4 [3] toolkit. Here the ICAL geometry is written to a machine readable GDML file – which includes the RPC detector components, the support structure, and the gas composition as described above – that can be read off by other associated packages, like the event reconstruction package. The pick-up strips are considered as a continuous material for GEANT4 simulations. However, for signal digitization the strips are considered independently.

When a charged particle, for example, a muon, passes through an RPC, it gives a signal which is assigned x or y values from the respective pick-up strip information, a z-value from the layer information, and a time stamp t. The minimum energy deposited in the RPC gap which will produce an electron–ion pair, and hence give a hit, is taken to be 30 eV, with an average efficiency of 95%. The global coordinates of the signals are then translated through digitization into information of the Xth x strip and the Yth y strip at the Zth plane. These digitized signals along with the time stamp form what are called 'hits' in the detector as this is precisely the information that will be available when the actual ICAL detector begins to take data.

The spatial resolution in the horizontal plane is of the order of cm (due to the strip width) while that in the z-direction is of the order of mm (due to the gas gap between the glass plates in the RPCs). The effect of cross-talk, i.e., the probability of either or both adjacent strips giving signals in the detector, is also incorporated, using the results of the on-going studies of RPCs [110]. Finally, as the X and Y strip information are independent, all possible pairs of the nearby X and Y hits in a plane are combined to form a 'cluster'.

A typical neutrino CC interaction giving rise to an event with a muon track and associated hadron shower is shown in figure 3.3. It can be seen that the muon track is clean with typically one or two hits per layer, whereas the hadron hits form a diffused shower.

3.4 *Event reconstruction*

The reconstruction of individual hadrons in the hadronic showers is not possible because the response of the detector to different hadrons is rather similar. Only an averaged information on the energy and

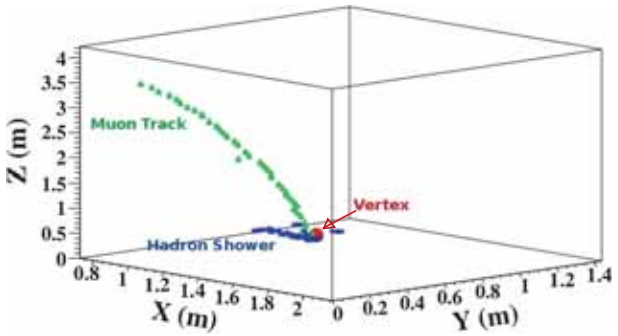

Figure 3.3. Sample track of a neutrino event with a muon track and hadron shower in the ICAL detector, where $z = 0$ indicates the central layer of the detector.

direction of the hadrons is in principle possible; furthermore, hadrons, due to the different nature of their interactions, propagate relatively short distances in the detector. The response of ICAL to hadrons as determined by simulation studies is described in §4.2.

Muons, on the other hand, being minimum ionizing particles, leave long clean tracks, and hence the ICAL detector is most sensitive to them. The muon momentum can be determined from the curvature of its trajectory as it propagates in the magnetized detector, and also by measuring its path length. The nanosecond time resolution of the RPCs also allows the distinction between up-going and down-going muons. The muon momentum reconstruction is achieved by using a track finder package, followed by a track fitting algorithm that reconstructs both the momentum and charge of the muon, using the information on the local magnetic field.

'The track finder' uses clusters, i.e., the combinations of all possible pairs of nearby X and Y hits in a Z-plane, as its basic elements. A set of clusters generated in three successive layers is called a 'tracklet'. The track finder algorithm uses a simple curve-fitting algorithm to find possible tracklets by finding clusters in three adjacent planes. It includes the possibility of no hit (due to inefficiency) in a given plane, in which case the next adjoining planes are considered. Typically, charged current muon neutrino interactions in ICAL have a single long track due to the muons and a shower from the hadrons near the vertex. Since, typically muons leave only about one or two hits per layer they traverse ($\sim$1.6 on average) as opposed to hadrons that leave several hits per layer, the hadron showers are separated by using criteria on the average number of hits per layer in a given event.

Ends of overlapping tracklets are matched to form longer tracks, and the longest possible track is found [111] by iterations of this process. The track finder package thus forms muon tracks as an array of three-dimensional clusters. In the rare cases when there are two or more tracks, the longest track is identified as the muon track. The direction (up/down) of the track is calculated from the timing information which is averaged over the X and Y timing values in a plane. For muon tracks which have at least 5 hits in the event, the clusters in a layer are averaged to yield a single hit per layer with X, Y, and timing information; the coordinates of the hits in the track are sent to the track fitter for further analysis. (This translates to a minimum momentum of about 0.4 GeV/c for a nearly vertical muon, below which no track is fitted.)

The 'track fitter', a Kalman filter-based algorithm, is used to fit the tracks based on the bending of the tracks in the magnetic field. Every track is identified by a starting vector $X_0 = (X, Y, \mathrm{d}X/\mathrm{d}Z, \mathrm{d}Y/\mathrm{d}Z, q/p)$ which contains the position of the earliest hit (X, Y, Z) as recorded by the finder, with the charge-weighted inverse momentum q/p taken to be zero. As the tracks are virtually straight in the starting section, the initial track direction (the slopes $\mathrm{d}X/\mathrm{d}Z$, $\mathrm{d}Y/\mathrm{d}Z$) is calculated from the first two layers. This initial state vector is then extrapolated to the next layer using a standard Kalman filter-based algorithm, which calculates the Kalman gain matrix using the information on the local magnetic field and the geometry, the composition of the matter through which the particle propagates, and the observed cluster position in that later.

In the existing code, the state prediction is based on the Kalman filter algorithm and the corresponding error propagation is performed by a propagator matrix [111]. The state extrapolation takes into account process noise due to multiple scattering as described in [112] and energy loss in matter, mostly iron, according to the Bethe formula [113]. A new improved set of formulae for the propagation of the state and errors [114], optimized for atmospheric neutrinos with large energy and range, have also been developed, and are being used in the Kalman filter. The extrapolated point is compared with the actual location of a hit in that layer, if any, and the process is iterated.

The process of iteration also obtains the best fit to the track. The track is then extrapolated backwards to another half-layer of iron (as the interaction is most likely to have taken place in the iron) to determine the vertex of the interaction and the best-fit value of the momentum at the vertex is returned as the reconstructed momentum (both in magnitude and direction). Only fits for which the quality of fit is better than $\chi^2/\mathrm{ndf} < 10$ are used in the analysis.

While q/p determines the magnitude of the momentum at the vertex, the direction is reconstructed using $\mathrm{d}X/\mathrm{d}Z$ and $\mathrm{d}Y/\mathrm{d}Z$, which yield the zenith and the azimuthal angles, i.e., θ and ϕ. The results on the quality of reconstruction are presented in the next section.

4. ICAL response to muons and hadrons

Muons are clean because they leave a trail,
Hadrons are dirty because they shower.
– M V N Murthy

In this section, we discuss the simulation response of ICAL to the final-state particles produced in neutrino–nucleus interactions as discussed in the previous section. Being minimum ionizing particles, muons typically register clean long tracks with just about one hit per RPC layer in the detector while hadrons produce a shower with multiple hits per layer, due to the very different nature of their interactions. Multiple scattering further affects the quality of the track.

First, we discuss the detector response with respect to single particles (muons or hadrons) with fixed energies. In order to simulate the neutrino events fully, we then use the particles generated in atmospheric neutrino events using the NUANCE [4] event generator, for calibration. For the case of single muons, we study the response of the detector to the energy/momentum, direction and charge of muons propagated with fixed energy/momentum and direction (θ, ϕ) from the central region of the detector (described in §3). Next, we propagate the hadrons, mainly single pions, also with fixed energy and direction, through the central region of the detector and determine the energy response of the detector with respect to hadrons. Amongst the particles generated via NUANCE, the muon tracks can be separated while the hits from all the hadrons in the event are treated as just one shower.

4.1 *Response of ICAL to muons*

In this section, we present the results of the reconstruction of the charge, energy, and direction of muons [8]. For this study, we confine ourselves to tracks generated only in the central region of the ICAL detector, i.e. $-4\ \mathrm{m} \leq x \leq 4\ \mathrm{m}$, $-4\ \mathrm{m} \leq y \leq 4\ \mathrm{m}$, and $-4\ \mathrm{m} \leq z \leq 4\ \mathrm{m}$, with the origin taken to be the centre of the central detector module. The particle may subsequently travel outside this region or even exit the detector: both fully contained and partially contained events are analysed together. At low energies, the tracks are fully contained while particles start to leave the detector region for $P_{\mathrm{in}} \gtrsim 6\ \mathrm{GeV/c}$, depending on the location of the vertex and the direction of the particles.

The μ^- and μ^+ are analysed separately for fixed values of the muon momentum P_{in} and direction: while $\cos\theta$ is kept fixed for a set of typically 10,000 muons, the azimuthal angle ϕ is smeared over all possible values from $-\pi$ to π. The distribution of reconstructed muon momentum for the particular choice $(P_{\mathrm{in}}, \cos\theta) = (5\ \mathrm{GeV/c},\ 0.65)$ is shown in the left panel of figure 4.1. As the results are almost identical, as can be seen from the figure, only the results for μ^- are presented in the further analysis.

The mean and the rms width σ are determined by fitting the reconstructed momentum distribution; the momentum resolution is defined as $R \equiv \sigma/P_{\mathrm{in}}$. Apart from the intrinsic uncertainties due to particle interactions and multiple scattering effects, the distribution – especially its width – is also sensitive to the presence of detector support structures, gaps for magnetic field coils, etc., that have been described in the previous section.

In addition, the reconstructed momentum distribution of low-energy muons has a clear asymmetric tail, as can be seen in the right panel of figure 4.1 for muons with $(P_{\mathrm{in}}, \cos\theta) = (1\ \mathrm{GeV/c}, 0.65)$. It can be seen that the distribution at low energies is significantly broader, and there is also a shift in the mean. It is therefore fitted with a convolution of Landau and Gaussian distributions. For muons with $P_{\mathrm{in}}{>}2\ \mathrm{GeV/c}$, the distributions are fitted with purely Gaussian distributions. In the case of Landau–Gaussian fits, the width is defined as $\sigma \equiv \mathrm{FWHM}/2.35$, in order to make a consistent and meaningful comparison with the Gaussian fits at higher energies, where the square root of the variance, or the rms width, equals FWHM/2.35. Before we present results on the muon resolution, we first discuss the impact on the resolutions of the muon angle and location within the detector.

4.1.1 *Momentum resolution in different azimuthal regions.*

The number of hits in the detector by a muon with a fixed energy will clearly depend on the zenith angle, because muons traversing at different angles travel different distances through each iron plate. As a result, the momentum resolution will depend on the zenith angle. However, it also has a significant dependence on the azimuthal angle for two different reasons. One is that the magnetic field explicitly breaks the local azimuthal symmetry of the detector geometry. There is an additional effect due to the coil gaps that are located at $x = x_0 \pm 4$ m where x_0 is the centre of each module. The second reason is that the support structures are also

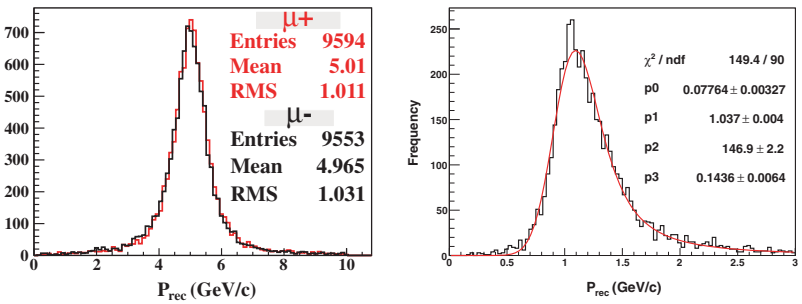

Figure 4.1. The left panel shows the reconstructed momentum distributions for $(P_{\rm in}, \cos\theta) = (5\ {\rm GeV/c}, 0.65)$ smeared over the central volume of the detector for μ^- and μ^+ particles [8]. The right panel shows the same distribution, but for $(P_{\rm in}, \cos\theta) = (1\ {\rm GeV/c}, 0.65)$, for μ^-, fitted with the Landau-convoluted-with-Gaussian distribution.

not azimuthally symmetric; moreover, the length of the track 'lost' within these dead spaces is also a function of the location from where the muon was propagated and the zenith angle at which it traverses these spaces. The cumulative dependence on the azimuthal angle ϕ is a complex consequence of all these dependences and impacts low momentum and large zenith angle muons more than higher energy, small angle ones.

For instance, a muon initially directed along the y-axis experiences less bending because the momentum component in the plane of the iron plates (henceforth referred to as in-plane momentum) is parallel to the magnetic field. Furthermore, upward-going muons that are in the negative (positive) x-direction experience a force in the positive (negative) z-direction (the opposite is true for μ^+) and so muons injected with $|\phi| > \pi/2$ traverse more layers than those with the same energy and zenith angle but with $|\phi| < \pi/2$ and hence are better reconstructed. This is illustrated in the schematic in figure 4.2 which shows two muons (μ^-) injected at the origin with the same momentum magnitude and zenith angle, one with positive momentum component in the x-direction, $P_x > 0$ and the other with negative x momentum component. The muon with $P_x > 0$ (initially directed in the positive x direction) bends differently from the one with $P_x < 0$ (along negative x-direction) and hence they traverse different number of layers, while having roughly the same path length. Hence, muons with different ϕ elicit different detector response. Because of these effects, the momentum resolution is best studied in different azimuthal angle bins. We separate our muon sample into four regions/bins: bin I with $|\phi| \leq \pi/4$, bin II with $\pi/4 < |\phi| \leq \pi/2$, bin III with $\pi/2 < |\phi| \leq 3\pi/4$, and bin IV with $3\pi/4 < |\phi| \leq \pi$. The resolutions of $P_{\rm in}$ in the above ϕ-regions, for six values of zenith angle, are shown in figure 4.3.

It may be noticed that, at lower energies the resolution improves as $\cos\theta$ increases, as expected, but

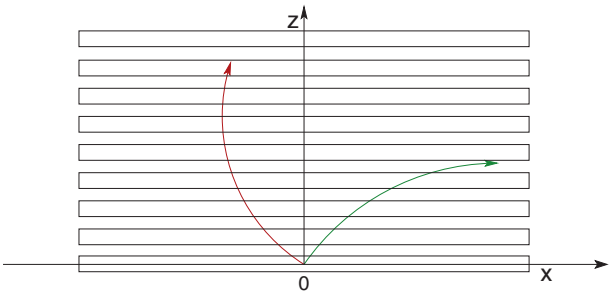

Figure 4.2. Schematic showing muon tracks (for μ^-) in the x–z plane for the same values of $(P_{\rm in}, \cos\theta)$ but with $|\phi| < \pi/2$ and $>\pi/2$ (momentum component in the x direction positive and negative, respectively). Different bending causes the muon to traverse different number of layers in the two cases.

at higher energies the behaviour is rather complicated. At higher energies, the muons injected at larger zenith angles in ϕ regions I and IV, have better resolutions than their counterparts at more vertical angles (for instance, $\cos\theta = 0.45$ vs. $\cos\theta = 0.85$) because larger portions of the tracks, being more slanted, are still contained within the detector. In contrast, in ϕ regions II and III, muons with larger zenith angles have worse resolution than those at smaller zenith angles because the former exits the detector from the y-direction and are partially contained. In general, at angles larger than about 75° ($\cos\theta = 0.25$), the resolution is relatively poor as there are several times fewer hits than at more vertical angles.

Finally, note that the simulation studies of the physics reach of ICAL discussed in later sections use the 'azimuth-averaged' resolutions for muons. This is because the main focus of ICAL is the study of neutrino oscillations using atmospheric neutrino fluxes that are azimuthally symmetric for $E_\nu \geq 2$ GeV. While studying the neutrinos from fixed astrophysical sources, for example, the azimuthal dependence of the detector needs to be taken into account.

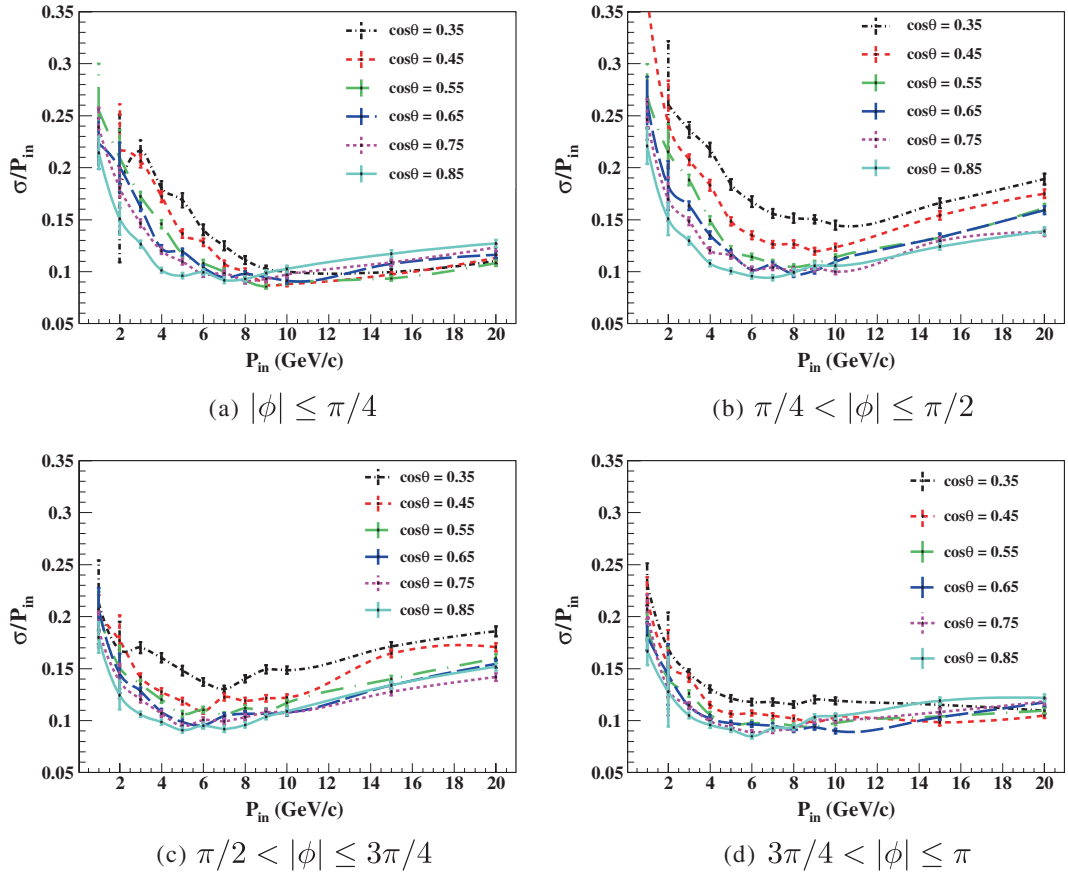

(a) $|\phi| \leq \pi/4$ (b) $\pi/4 < |\phi| \leq \pi/2$

(c) $\pi/2 < |\phi| \leq 3\pi/4$ (d) $3\pi/4 < |\phi| \leq \pi$

Figure 4.3. Muon resolution as a function of input momentum and $\cos\theta$, in bins of ϕ as described in the text [8].

In the rest of this section, we present simulations studies of the 'azimuth-averaged' response of ICAL to the muon direction and its charge, because these are not very sensitive to the azimuth. We also present the overall reconstruction efficiency for muons; this determines the overall reconstruction efficiency of the entire neutrino event as there may or may not be an associated hadron shower in the event.

4.1.2 *Zenith angle resolution*. The events that are successfully reconstructed for their momenta are analysed for their zenith angle resolution. The reconstructed zenith angle distribution for muons with $P_{\text{in}} = 1$ GeV/c, at zenith angles $\cos\theta = 0.25$ and $\cos\theta = 0.85$, are shown in figure 4.4, where the time resolution of the RPCs is taken to be 1 ns (muons with $\cos\theta = 1$ are up-going). It can be seen that a few events are reconstructed in the opposite (downward) direction i.e., with zenith angle ($\theta_{\text{rec}} \sim \pi - \theta$). For muons with $P_{\text{in}} = 1$ GeV/c at large (small) angles with $\cos\theta = 0.25\,(0.85)$, this fraction is about 4.3 (1.5)%. As energy increases, the fraction of events reconstructed in the wrong direction drastically comes down. For example, this fraction reduces to 0.3% for muons with $P_{\text{in}} = 2$ GeV/c at $\cos\theta = 0.25$. Comparison of the goodness of fits to a track, assuming it to be in upward and downward directions, reduces this uncertainty further. The analysis incorporating this technique is in progress.

The muons that contribute to mass hierarchy identification have energies greater than about 4 GeV and the time interval between the first and the last hits of such muons is more than 5 ns, so that the up-going vs. down-going muons would be easily identified. The time resolution of the detector therefore is not expected to affect the mass hierarchy determination.

The event distribution as a function of the reconstructed zenith angle is shown in the left panel of figure 4.5 for a sample $(P_{\text{in}}, \cos\theta) = (5$ GeV/c, 0.65). It is seen that the distribution is very narrow, indicating a good angular resolution for muons. The right panel of figure 4.5 shows the θ resolution as a function of input momentum for different zenith angles.

As noted earlier, due to multiple scattering and the smaller number of layers with hits, the momentum resolution is worse at lower energies. This is also true for the zenith angle, whose resolution improves with energy. For a given energy, the resolution is worse for

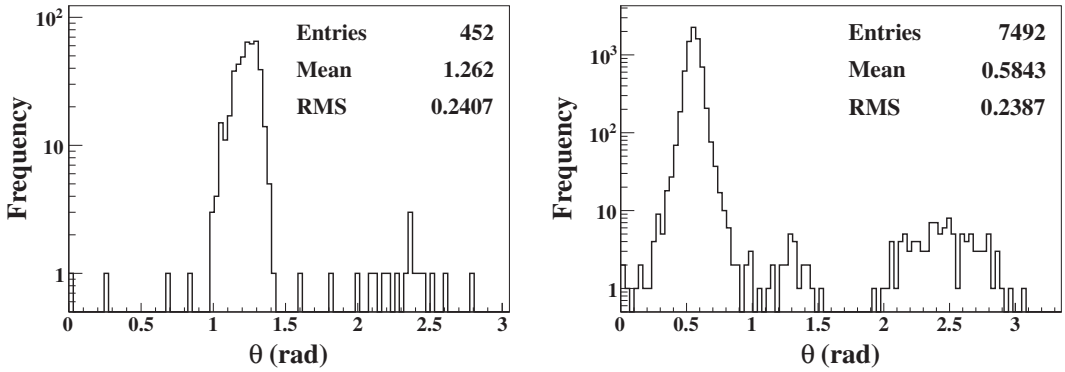

(a) $\cos\theta = 0.25; \theta = 1.318$ (b) $\cos\theta = 0.85; \theta = 0.555$

Figure 4.4. Reconstructed theta distribution for $P_{\text{in}} = 1$ GeV/c at two values of $\cos\theta$ [8]. The time resolution of the RPCs has been taken to be 1 ns. Note that the fraction of muons reconstructed in the wrong hemisphere decreases sharply with energy.

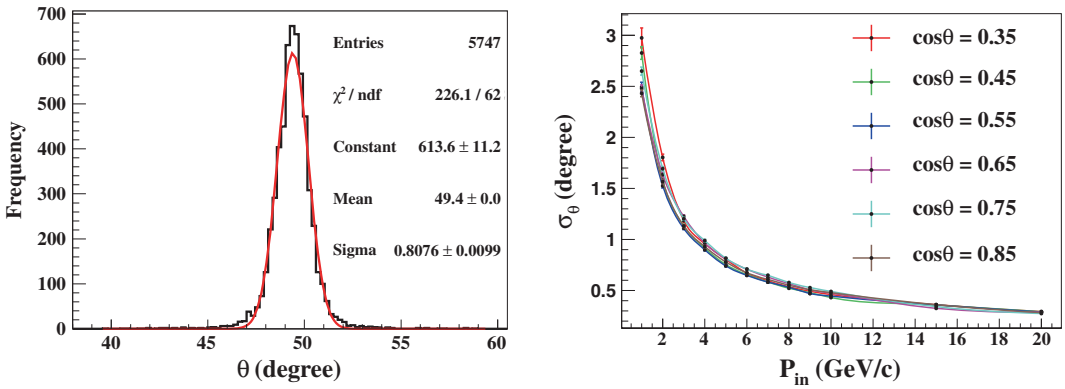

Figure 4.5. The left panel shows the reconstructed θ distribution for input $(P_{\text{in}}, \cos\theta) = (5$ GeV/c, 0.65). The right panel shows the θ resolution as a function of input momentum.

larger zenith angles because, again the number of layers with hits decreases. Even so, it is seen that the angular resolution for $\cos\theta \geq 0.25$ (i.e. $\theta \lesssim 75°$) is better than 1° for muon momenta greater than 4 GeV/c.

4.1.3 *Reconstruction efficiency*. The reconstruction efficiency for muons is defined as the ratio of the number of reconstructed events n_{rec} (irrespective of charge) to the total number of events, N_{total} (typically 10,000). We have

$$\epsilon_{\text{rec}} = \frac{N_{\text{rec}}}{N_{\text{total}}},$$

$$\delta\epsilon_{\text{rec}} = \sqrt{\epsilon_{\text{rec}}(1-\epsilon_{\text{rec}})/N_{\text{total}}}\,. \tag{4.1}$$

The left panel of figure 4.6 shows the muon reconstruction efficiency as a function of input momentum for different $\cos\theta$ bins.

When the input momentum increases, the reconstruction efficiency also increases for all angles, because the number of hits increases as the particle crosses more number of layers. At larger angles, the reconstruction efficiency for small energies is smaller compared to vertical angles as the number of hits for reconstructing tracks is less. But as the input energy increases, above almost 4 GeV since the particle crosses more number of layers, the efficiency of reconstructing momentum also increases and becomes comparable with vertical angles. At higher energies, the reconstruction efficiency becomes almost constant. The drop in efficiency at high energies for vertical muons is due to the track being partially contained, their smaller bending in the magnetic field, as well as the impact of the detector support structure. It is expected that this may improve as the track recognition algorithms are refined and better tuned.

The fraction of muonless charged current events/neutral current events that get misidentified as charged current muon events is ∼2−3%, as long as the energy of the reconstructed muon is $\gtrsim$1 GeV. This fraction may be further reduced with a proper choice of cuts, and for high-energy muons that are relevant for mass hierarchy determination, this is expected to be negligible. Work in this direction is in progress.

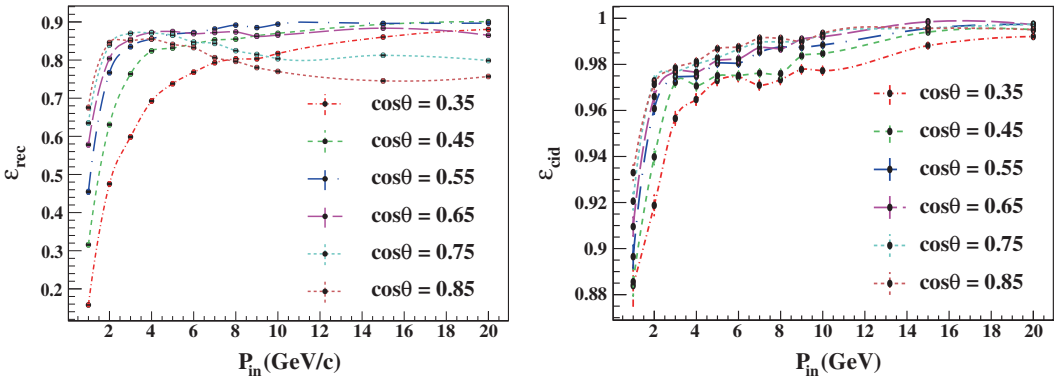

Figure 4.6. The left (right) panel shows the reconstruction efficiency (the relative charge identification efficiency) as a function of the input momentum for different cos θ values [8].

4.1.4 *Relative charge identification efficiency.* The charge of the particle is determined from the direction of curvature of the track in the magnetic field. Relative charge identification efficiency is defined as the ratio of the number of events with correct charge identification, n_{cid}, to the total number of reconstructed events:

$$\epsilon_{\text{cid}} = \frac{N_{\text{cid}}}{N_{\text{rec}}},$$

$$\delta\epsilon_{\text{cid}} = \sqrt{\epsilon_{\text{cid}}(1-\epsilon_{\text{cid}})/N_{\text{rec}}}. \tag{4.2}$$

Figure 4.6 shows the relative charge identification efficiency as a function of input momentum for different cos θ bins. As seen earlier, there is a very small contribution to the set with the wrongly identified charge from the events where the track direction is wrongly identified ($\theta \rightarrow \pi - \theta$); such events will also reconstruct with the wrong charge as there is a one-to-one correspondence between the up–down identification and the muon charge.

When a low-energy muon propagates in the detector, it undergoes multiple scattering. So the number of layers with hits is small, and the reconstruction of charge goes wrong, which results in poor charge identification efficiency as can be seen from figure 4.6. As the energy increases, the length of the track also increases, due to which the charge identification efficiency also improves. Beyond a few GeV/c, the charge identification efficiency becomes roughly constant, about 98%.

4.2 *Response of ICAL to hadrons*

An important feature of ICAL is its sensitivity to hadrons over a wide energy range. This allows the reconstruction of the energy of the incoming muon neutrino in a charged-current event by combining the energies of the muon and the hadrons. It also enables the detection of neutral-current events, charged-current DIS events generated by ν_e interactions, and charged-current ν_τ events where τ decays hadronically. The information contained in all these events adds crucially to our knowledge of neutrino oscillations. The charged-current event is a direct measure of the oscillation probabilities among the three active neutrino species. On the other hand, the neutral-current events are not affected by active neutrino oscillations, and hence help in flux normalization, as well as in the search for oscillations to sterile neutrinos. It is therefore important to characterize the response of the ICAL to hadrons.

The hadrons generated from the interactions of atmospheric neutrinos consist mainly of neutral and charged pions, which together account for about 85% of the events. The rest of the events consists of kaons and nucleons, including the recoil nucleons that cannot be distinguished from the remaining hadronic final state. The neutral pions decay immediately giving rise to two photons, while the charged pions propagate and develop into a cascade due to strong interactions. For the neutrino–nucleon interaction $\nu_\mu N \rightarrow \mu X$, the incident neutrino energy is given by

$$E_\nu = E_\mu + E_{\text{hadrons}} - E_N, \tag{4.3}$$

where E_N is the energy of the initial nucleon which is taken to be at rest, neglecting its small Fermi momentum. The visible hadron energy depends on factors like the shower energy fluctuation, leakage of energy, and invisible energy loss mechanisms, which in turn affect the energy resolution of hadrons. We choose to quantify the hadron response of the detector in terms of the quantity [9]

$$E'_{\text{had}} = E_\nu - E_\mu. \tag{4.4}$$

As the first step in understanding the ICAL response to hadrons, single charged hadrons of fixed energies are generated via Monte Carlo and propagated through the detector to compare its response to them. The response to charged pions is then studied in more detail, and the pion energy is calibrated against the number of hits. Next, the multiple hadrons produced through atmospheric neutrino interactions are generated using NUANCE [4], and the quantity E'_{had} is used to calibrate the detector response. This should take care of the right combination of the contributions of different hadrons to the hits, on an average. It will of course be dominated by neutral and charged pions, and hence we expect it to be similar to the response to fixed-energy pions.

4.2.1 *Energy response to fixed-energy hadrons.* In an RPC, the X- and Y-strip information on a hit is 'independently' obtained from the top and bottom pick-up strips, as described in §1.1.3 and then combined to give the (X, Y) coordinates of the hit. For a muon, the (X, Y) positions of the hits in a given layer can easily be identified because a muon usually leaves only one or two hits per layer. However, a hadron shower consists of multiple hits per layer, and combining all possible X and Y strip hits leads to overcounting, resulting in what are termed as 'ghost hits'. To avoid the ghost hit counts, the variables 'x-hits' and 'y-hits' – the number of hits in the X and Y strips of the RPC, respectively – can be used. We choose to perform the energy calibration with the variable 'orig-hits', which is the maximum of x-hits or y-hits.

Figure 4.7 shows the comparison of these three types of hit variables for $\pi^{\pm}$ of energy 3 GeV. Clearly, there is no significant difference among these variables. However, orig-hit has been used as the unbiased parameter. It is also observed that the detector response to the positively and negatively charged pions is identical. So we shall not differentiate between them henceforth.

Fixed-energy single pion events in the energy range of 1 to 15 GeV were generated using the particle gun in GEANT4. The total number of events generated for each input energy value is 10,000 in this section, unless specified otherwise. Each event is randomly generated to have vertices over a volume of 2 m × 2 m × 2 m in the central region of the ICAL detector. As in the earlier section, the reference frame chosen has the origin at the centre of the detector, the z-axis pointing vertically up, and the x–y plane along the horizontal plates, with the three modules lined up along the x-axis. The hadron direction is uniformly smeared over the zenith angle $0 \leq \theta \leq \pi$ and azimuth of $0 \leq \phi \leq 2\pi$. This serves to smear out any angle-dependent bias in the energy resolution of the detector by virtue of its geometry which makes it the least (most) sensitive to particles propagating in the horizontal (vertical) direction.

Figure 4.8 shows the hit distributions in the detector for pions, kaons, and protons at various energies in the range of 1 to 15 GeV. It is observed that the hit patterns are similar for all these hadrons, though the peak positions and spreads are somewhat dependent on the particle ID. Hence, the detector cannot distinguish the specific hadron that has generated the shower. The large variation in the number of hits for the same incident particle energy is mainly a result of different strong interaction processes for different hadrons (for π^0 the interactions are electromagnetic because it decays immediately to a $\gamma\gamma$ pair), and partly an effect of angular smearing.

4.2.2 *The e/h ratio.* The NUANCE [4] simulation suggests that the fraction of the different types of hadrons produced in the detector is $\pi^+ : \pi^- : \pi^0 ::$

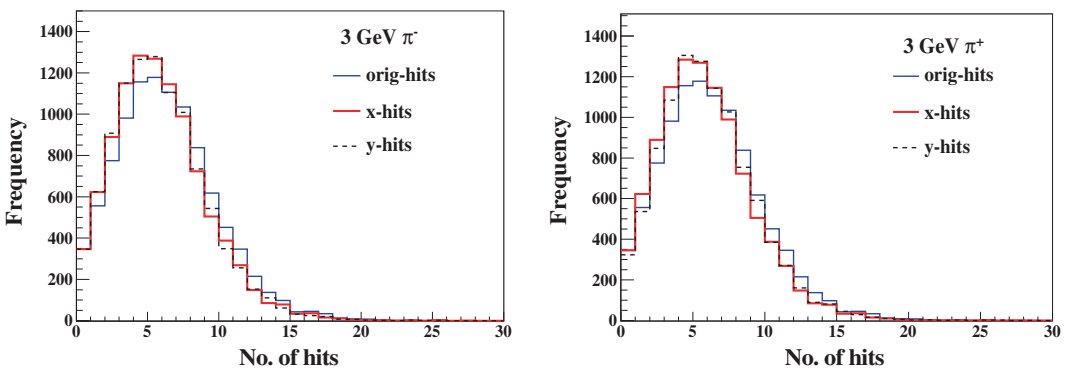

Figure 4.7. The comparison of the distributions of x-hits, y-hits and orig-hits for π^- (left) and π^+ (right) of energy 3 GeV [9].

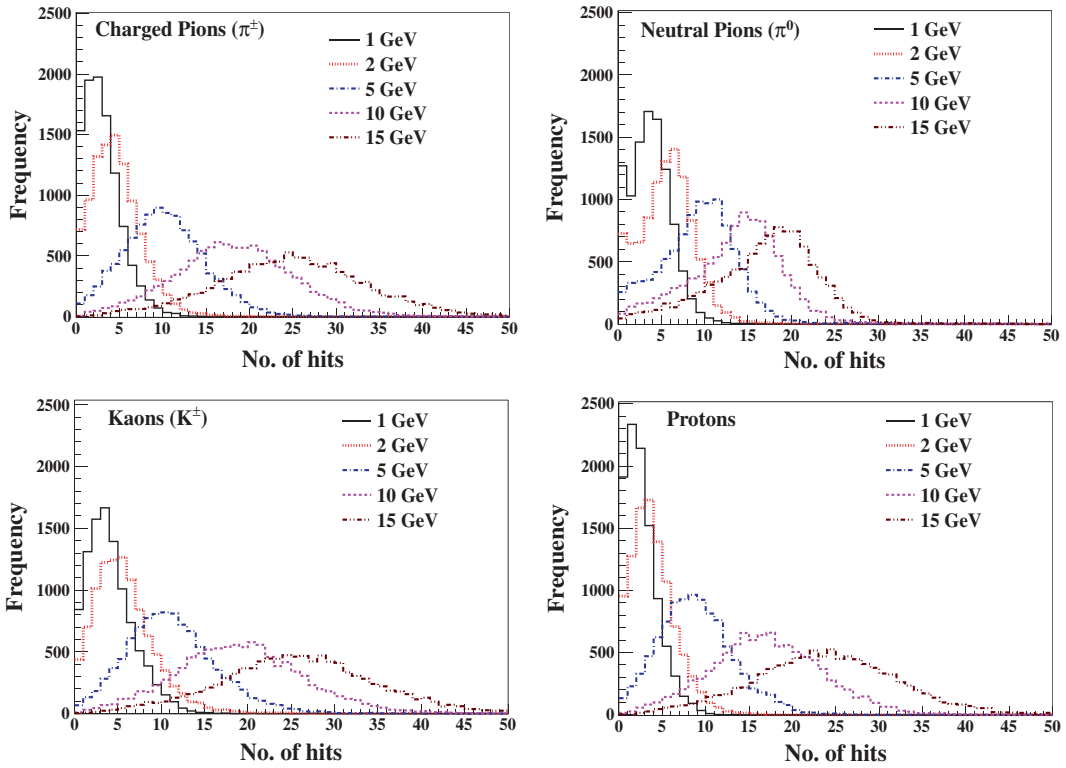

Figure 4.8. The direction-averaged hit distributions at various energies for $\pi^{\pm}$, π^0, $K^{\pm}$ and protons propagated from vertices smeared over the chosen detector volume [9].

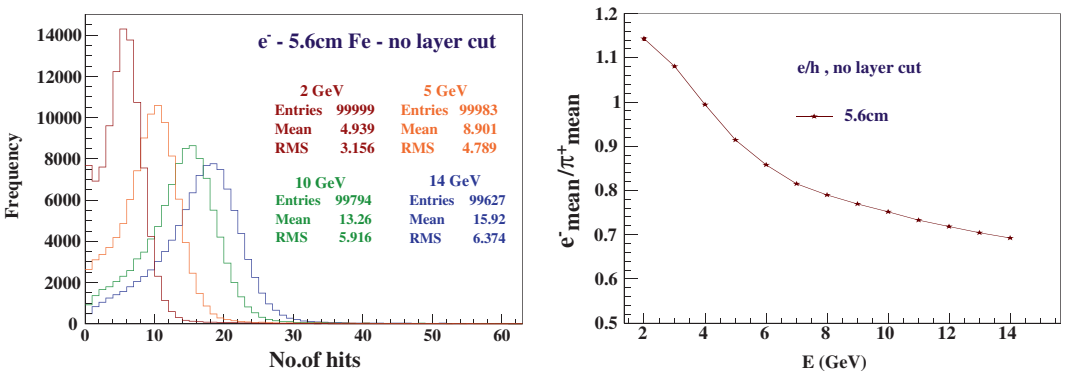

Figure 4.9. The left panel shows the hit distributions of fixed energy single electrons at 2, 5, 10, and 14 GeV, averaged over all directions. The right panels shows the variation of the e/h ratio with the particle energies [10].

0.38 : 0.25 : 0.34, with the remaining 3% contribution coming mainly from kaons [10]. While the response of the detector to π^+ and π^- is almost identical as seen earlier, its response to the electromagnetic part of the hadron shower that originates from π^0 is different. This may be quantified in terms of the e/h ratio, i.e. the ratio of the electron response to the charged pion response. This ratio will help us characterize the effect of neutral hadrons on the energy resolution.

In order to study this ratio, we generated 100,000 electron events at fixed energies in the energy range 2–15 GeV, propagating in arbitrary directions (with θ smeared from $0-\pi$ and ϕ from $0-2\pi$) from vertices within a volume of 2 m × 2 m × 2 m in the central region of the ICAL detector. The hit distributions averaged over all directions for 2, 5, 10, and 14 GeV electrons are shown in figure 4.9. This may be compared with the hit distributions shown in figure 4.8. The response is almost the same as that for π^0, with narrower high-energy tails than those for charged pions.

The e/h ratio is obtained as

$$e/h = e^-_{\text{mean}}/\pi^+_{\text{mean}}, \tag{4.5}$$

where e^-_{mean} is the arithmetic mean of the electron hit distribution and π^+_{mean} is the arithmetic mean of the hit distribution for π^+, for a given fixed energy of the two particles. If $e/h = 1$, then the detector is said to be compensating. The variation of the e/h ratio with incident energy is shown in the right panel of figure 4.9.

It can be seen that the value of e/h decreases with energy. However, it should be noted that there is no direct measurement of the energy deposited in ICAL. Here the energy of a shower is simply 'calibrated' to the number of hits, and electrons which travel smaller distances in a high Z material like iron have lower number of hits compared to charged pions. At lower energies, the electron as well as pion shower hits are concentrated around a small region. The mean of the electron hit distribution is roughly the same or slightly larger than that of the π^+ hit distribution. With the increase in energy, the charged pions travel more distance and hence give more hits (as they traverse more layers) because the hadronic interaction length is much more than the electromagnetic interaction length at higher energies and hence the ratio of hits in the two cases drops with energy.

In a neutrino interaction where all types of hadrons can be produced (although the dominant hadrons in the jet are pions), the response of ICAL to hadrons produced in the interaction depends on the relative fractions of charged and neutral pions. Using the relative fractions $\pi^+ : \pi^- : \pi^0 :: 0.38 : 0.25 : 0.34$ as mentioned above, the average response of hadrons obtained from the charged current muon neutrino interaction can be expressed as

$$\begin{aligned} R_{\text{had}} &= [(1 - F_0) \times h + F_0 \times e], \\ &= h\left[(1 - F_0) + F_0 \times \frac{e}{h}\right], \end{aligned} \tag{4.6}$$

where e is the electron response, h the charged hadron response, and F_0 is the neutral pion fraction in the sample.

The atmospheric neutrino events of interest in ICAL are dominated by low-energy events with hadrons typically having energies $E < 10$ GeV for which the average value of e/h is $e/h \approx 0.9$. Using $F_0 = 0.34$ in eq. (4.6), we get the average hadron response for NUANCE-generated events to be $R_{\text{had}} \approx 0.97h$ which is not very different from h. For this reason, the analysis of response with multiple hadrons in NUANCE-generated event samples is not expected to be very different from that of the single pion sample. However, we shall confirm this by first focussing on the detector response to fixed-energy charged pions in §4.2.3, and then moving on to a more general admixture of different hadrons in §4.2.5.

4.2.3 *Analysis of the charged pion hit pattern.* The hit distributions for charged pions, at sample values of $E = 3, 8$ GeV, are shown in figure 4.10. The distributions are asymmetric with long tails, with a mean of about two hits per GeV. In addition, at low energies several events yield zero hits in the detector.

A search for a good fitting function for the distribution was made, and it was found that the Vavilov distribution function gives a good fit for all energies, as is illustrated in figure 4.10. This distribution (see Appendix C) is described by the four parameters P_0, P_1, P_2, and P_3, which are energy-dependent [9]. The Vavilov distribution reduces to a Gaussian distribution for $P_0 \geq 10$, which happens for $E > 6$ GeV. However, at lower energies, it is necessary to use the full Vavilov distribution.

The mean $\bar{n}(E)$ of the number of hits from the Vavilov fit at different energies is shown in the left panel of figure 4.11. It increases with increasing pion energy, and saturates at higher energies. It may be approximated by

$$\bar{n}(E) = n_0[1 - \exp(-E/E_0)], \tag{4.7}$$

where n_0 and E_0 are constants. This fit has to be interpreted with some care, because n_0 and E_0 are sensitive to the energy ranges of the fit. The value of E_0 is found to be $\sim$30 GeV when a fit to the energy range 1–15 GeV is performed. As the energies of interest for atmospheric neutrinos are much less than E_0, eq. (4.7) may be used in its approximate linear form $\bar{n}(E) = n_0 E/E_0$. A fit to this linear form is also shown in figure 4.11.

As in the linear regime ($E \ll E_0$) one has

$$\frac{\bar{n}(E)}{n_0} = \frac{E}{E_0}, \tag{4.8}$$

the energy resolution may be written as

$$\frac{\sigma}{E} = \frac{\Delta n(E)}{\bar{n}(E)}, \tag{4.9}$$

where $(\Delta n)^2$ is the variance of the distribution. The notation σ/E will be used for energy resolution throughout, and eq. (4.9) will be taken to be valid for the rest of the analysis.

The energy resolution of pions may be parametrized by

$$\frac{\sigma}{E} = \sqrt{\frac{a^2}{E} + b^2}\,, \tag{4.10}$$

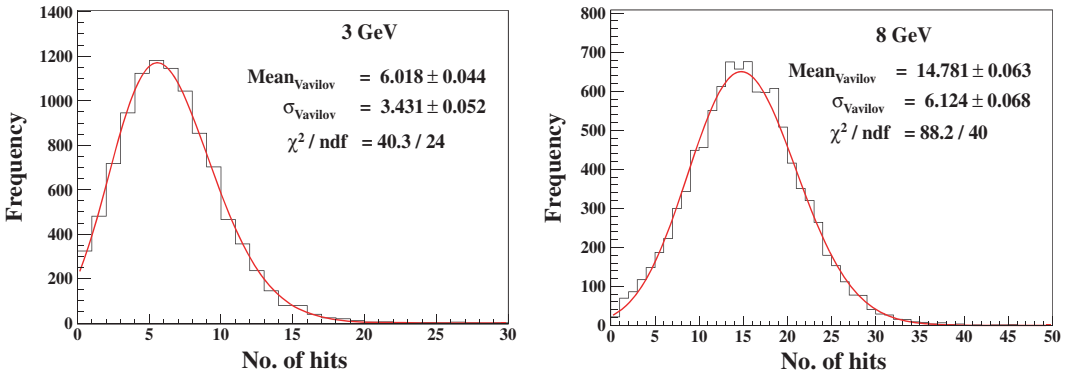

Figure 4.10. The hit distributions at 3 (left) and 8 GeV (right), for pions propagating in the detector, starting from randomized vertices over a volume of 2 m×2 m×2 m in the detector. The red curve denotes a fit to the Vavilov distribution [9].

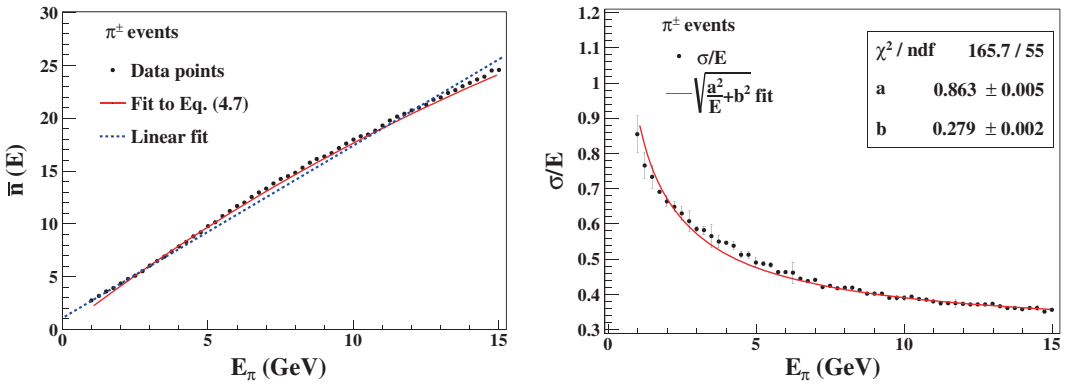

Figure 4.11. The mean hit distribution (left) and the energy resolution (right) for fixed-energy charged pion events, as a function of pion energy. The right panel also shows a fit to eq. (4.10) [9].

where a and b are constants. The energy resolutions for charged pions as functions of the pion energy are shown in the right panel of figure 4.11. The parameters a and b extracted by a fit to eq. (4.10) over the pion energy range 1–15 GeV are also shown. The values of a and b depend on the iron plate thickness; this dependence has been studied in detail in Appendix D.

4.2.4 *Dependence of the energy resolution on hadron direction.* As the number of layers traversed by a particle would depend on the direction of the particle, it is expected that the energy calibration and energy resolution for hadrons will depend on the direction of the hadron. To check this dependence, we simulate pions of fixed energies in the detector, which travel in different directions. The directions are binned into five zenith angle bins, and the distributions of the number of hits are recorded. The ratio of the rms width of the distribution to its mean is used as a measure of the energy resolution [10]. Figure 4.12 shows the zenith angle dependence of the hadron energy resolution.

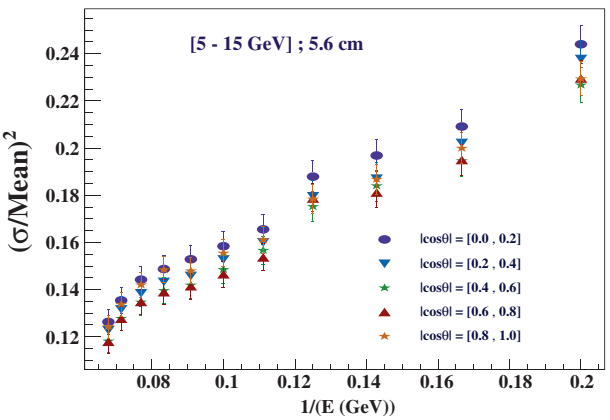

Figure 4.12. The dependence of the pion energy resolution on the zenith angle [10].

As there is only a mild dependence on the hadron direction, and the direction of hadron itself cannot be determined yet with a good confidence, we continue to use the direction-averaged results in the future analyses in this Review.

4.2.5 *Response to hadrons produced by atmospheric neutrinos*. Atmospheric neutrino interactions in the detector may contain no hadrons (for quasielastic scattering events), one hadron or multiple ones (in resonance scattering and DIS events). While the former events dominate for $E_\nu \sim 1$ GeV, at higher energies the DIS events dominate. In this section, we focus on the charged-current ν_μ interactions in the detector that produce hadrons in addition to the charged muons.

We assume here that the ν_μ CC events can be clearly separated from the NC as well as ν_e CC events, and that the muon and hadron shower may be identified separately. (In our procedure, we determine the number of hadron hits by taking away the true muon hits, as in the Monte Carlo simulation, from the total hits in the event.) Preliminary studies show that this is a reasonable assumption for $E_\nu \gtrsim 1$ GeV. At lower energies where the number of hits is small, the misidentification of a muon hit as a hadron one, or vice versa, can significantly affect the hadron energy calibration. The analysis of this effect is in progress.

The atmospheric neutrino (ν_μ) and antineutrino ($\bar{\nu}_\mu$) events in ICAL have been simulated using the neutrino event generator NUANCE (v3.5) [4]. The hadrons produced in these interactions are primarily pions, but there are some events with kaons (about 3%) and a small fraction of other hadrons as well. As discussed earlier, it is not possible to identify the hadrons individually in ICAL. However, since the hit distribution of various hadrons are similar to each other (see figure 4.8), and the NUANCE generator is expected to produce a correct mixture of different hadrons at all energies, it is sufficient to determine the hadron energy resolution at ICAL through an effective averaging of NUANCE events, without having to identify the hadrons separately.

A total of 1000 kt-yr of 'data' events (equivalent to 20 years of exposure with the 50 kt ICAL module) were generated with NUANCE. The events were further binned into the various $E'_{\rm had}$ energy bins and the hit distributions (averaged over all angles) in these bins are fitted to the Vavilov distribution function. The mean values ($\text{Mean}_{\text{Vavilov}}$) of these distributions as a function of $E'_{\rm had}$ are shown in the left panel of figure 4.13. As expected, these are similar to the mean values obtained earlier with fixed energy pions. As the mean hits grow approximately linearly with energy, the same linearized approximation used in §4.2.3 can be used to obtain the energy resolution $\sigma/E = \Delta n/\bar{n}$. The energy resolution as a function of $E'_{\rm had}$ is shown in figure 4.13. The energy resolution ranges from 85% (at 1 GeV) to 36% (at 15 GeV).

The effective energy response obtained from the NUANCE-generated data is an average over the mixture of many hadrons that contribute to hadron shower at all energies. The fractional weights of different kinds of hadrons produced in neutrino interactions may, in principle, depend on neutrino oscillations. In addition, the relative weights of events with different energy that contribute in a single energy bin changes because neutrino oscillations are energy-dependent. In order to check this, events with oscillations using the best-fit values of standard oscillation parameters (mixing angles and mass-squared differences) [115] were also generated. The resolutions obtained without and with oscillations are very close to each other. Thus, the hadron energy resolution can be taken to be insensitive to oscillations.

4.2.6 *Hadron energy calibration*. To calibrate the hadron energy $E'_{\rm had}$ against the hit multiplicity, hadrons from the simulated NUANCE [4] 'data' were divided

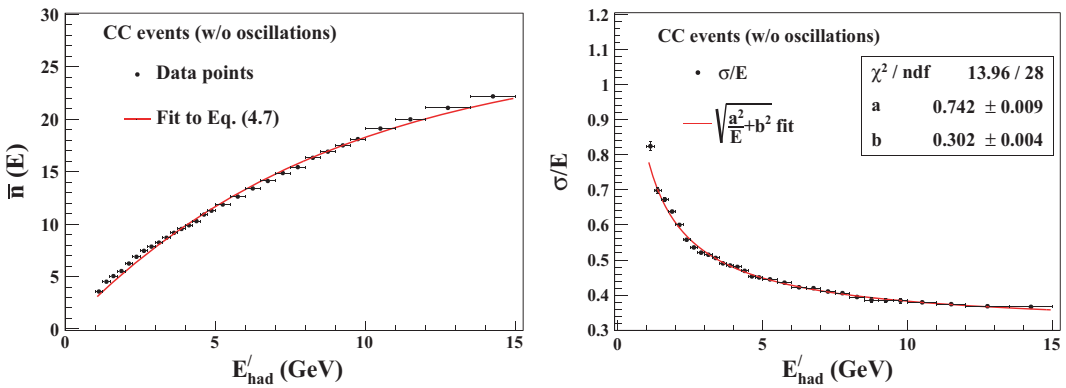

Figure 4.13. The mean hit distribution (left) and the energy resolution (right) for hadron events generated by NUANCE, as a function of $E'_{\rm had}$. The right panel also shows a fit to eq. (4.10). The bin widths are indicated by horizontal error bars [9].

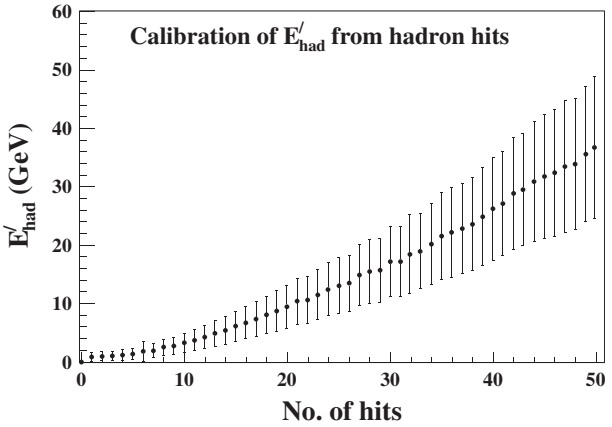

Figure 4.14. Calibration plot for E'_{had}, where mean and σ from the Vavilov fits are represented by the black filled circles and error bars, respectively [9].

into bins of different hit multiplicities n. Even here, a good fit was obtained for the Vavilov distribution function at all values of n. We show the mean, $\text{Mean}_{\text{Vavilov}}$, and the standard deviation, σ_{Vavilov}, obtained from the fit in the calibration plot in figure 4.14.

For charged-current ν_μ events, the energy of the incident neutrino can be reconstructed through

$$E_\nu = E_\mu + E'_{\text{had}}, \tag{4.11}$$

where E_μ is reconstructed from the Kalman filter algorithm and E'_{had} is calibrated against the number of hadronic hits. The neutrino energy resolution will in principle depend on the energy and direction of the muon as well as that of the hadron shower. The poor energy resolution of hadrons also makes the energy resolution of neutrinos rather poor, and loses the advantage of an accurate muon energy measurement. Therefore, reconstructing neutrino energy is not expected to be the most efficient method for extracting information from the ICAL analysis. Indeed, we expect to use the muon and hadron information separately, as will be seen in §5.8.

4.2.7 *Salient features of the detector response*. The ICAL detector is mainly sensitive to muons produced in the charged-current interactions of atmospheric ν_μ or $\bar{\nu}_\mu$. We have studied the response of the detector to muons [8] generated in the central volume of a module of the ICAL detector where the magnetic field is uniform. The momentum, charge, and direction of the muons are determined from the curvature of the track in the magnetic field using Kalman filter algorithm. The response of the detector to muons in the energy range 1–20 GeV with $\cos\theta > 0.25$ is studied in the different azimuthal ϕ regions. The momentum resolution, reconstruction efficiency, charge identification efficiency, and direction resolution are calculated. The momentum resolution is about 20% (10%) for energies of 2 GeV (10 GeV), while the reconstruction efficiency is about 80% for $E_\mu > 2$ GeV. The relative charge identification efficiency is found to be 98% for almost all energies above the threshold. The direction resolution is found to be better than a degree for all angles for energies greater than about 4 GeV.

The hadron events of interest in the ICAL detector primarily contain charged pions. The hit pattern of pions and kaons in the detector is similar; hence it is not possible to separate different hadrons in the detector. Similarly, neutrino–nucleus interactions produce events with multiple hadrons in the final state (generated by the NUANCE neutrino generator), whose energies cannot be reconstructed individually. However, the 'total energy' deposited in hadrons can be determined by a calibration against the hit multiplicity of hadrons in the detector [9].

The hit patterns in single and multiple hadron events are roughly similar, and may be described faithfully by a Vavilov distribution. Analyses, first with fixed-energy pions, and later with a mixture of hadrons from atmospheric ν_μ interaction events, show that a hadron energy resolution in the range 85% (at 1 GeV)–36% (at 15 GeV) is obtainable. The parameters of the Vavilov fit presented here as a function of hadron energy can be used for simulating the hadron energy response of the detector, in order to perform physics analyses that need the hadron energy resolution of ICAL. We have also presented the calibration for the energy of the hadron shower as a function of the hit multiplicity. This analysis will be improved upon by incorporating edge effects and noise in a later study, after data from the prototype detector are available.

The reconstruction of hadrons allows us to reconstruct the total visible energy in NC events. Combined with the information on the muon energy and direction in the CC events, it will also allow one to reconstruct total neutrino energy in the CC events. As we shall see in §5, the correlated information in muon and hadron in a CC event will also help to enhance the capabilities of the ICAL. The ICAL will be one of the largest neutrino detectors sensitive to the final-state muons as well as hadrons in neutrino interactions at multi-GeV energies, and this advantage needs to be fully exploited.

Note that the calibration of the hadron response presented in this section has been determined by Monte Carlo simulations. To confirm its validity, we have

compared in Appendix D the results of our simulations with the hadron response at MINOS and the baby MONOLITH detector at appropriate plate thicknesses. This appendix also studies the dependence of hadron response at ICAL as a function of the iron plate thickness.

Some muon events at ICAL will also arise from the ν_τ's arising due to oscillations of ν_μ. These ν_τ's may produce τ's through charged-current interactions, which would further decay to muons within the detector. These events will then contaminate the direct muon signal [116]. The number of such events (indirect muon events through tau production) is however heavily suppressed, first due to the mass of τ that implies a large threshold energy for the neutrino, then due to the small branching fraction of $\tau \rightarrow \mu\nu_\tau\bar{\nu}_\mu$, and finally due to the three-body kinematics of τ decay that reduces the energy of the resultant muon even further. This results in only about 150 such indirect muon events in five years, as compared to a few thousands of direct muon events. Hence, at this level of analysis, we have neglected these events. The ν_e charged current events which may be mistakenly reconstructed as charged-current muon events have also been neglected at this stage. These are in the process of being included in a more sophisticated analysis.

5. Neutrino oscillation physics at ICAL

The pendulum of mind oscillates between sense and nonsense, not between right and wrong.
– Carl Gustav Jung

In this section, we shall present the physics capabilities of ICAL for the mixing parameters within the three-generation flavour oscillation paradigm. We shall restrict ourselves to the charged-current events produced in the ICAL from ν_μ and $\bar{\nu}_\mu$ interactions, which produce μ^- and μ^+, respectively. We shall start by describing our analysis method in §5.1, and then proceed to present the results showing the physics reach of this experiment for various quantities of interest. We shall focus on the identification of the neutrino mass hierarchy, as well as on the precision measurements of $|\Delta m^2_{32}|$ and θ_{23}.

The results will be presented using three different analyses. First in §5.2, we use only the information on the measured muon energy and muon direction $(E_\mu, \cos\theta_\mu)$, both of which should be rather precisely measured in this detector, as described in detail in §4. Note that the results for the muon reconstruction used in these physics analyses have been obtained with an averaging over the azimuthal angle, and with the vertex taken to be in the central (8 m × 8 m × 10 m) region of each module of the detector. These muons may propagate out of this region into the peripheral regions, and even exit the detector. The latter 'partially contained' events roughly form about 12% of our sample, and we have not analysed them separately.

We next show the improvement expected in the precision measurement of the atmospheric mass squared difference and the mixing angle if we use the information on the hadron energy in addition, to reconstruct the neutrino energy in each event. In this analysis, first in §5.7 we analyse the data in terms of the reconstructed neutrino energy and the measured muon angle $(E_\nu, \cos\theta_\mu)$. However, the reconstruction of neutrino energy involves the addition of the rather coarsely known hadron energy information to the measured muon energy, which results in a dilution of the muon energy information, which is more accurately known due to the good tracking capabilities of the ICAL. In order to retain the benefits of the accurately measured muon energy, we separately use the information on the measured muon energy, muon direction, and the hadron energy $(E_\mu, \cos\theta_\mu, E'_{\rm had})$ corresponding to each atmospheric neutrino event at the ICAL detector. The results of this final analysis, which leads to the best physics reach for ICAL at this stage, are presented in §5.8.

Note that the detector characteristics used for the analyses presented in this section have been determined in the central region of the central module of the ICAL detector, as mentioned in the previous section. When the three modules are placed adjacent to each other along the x-axis, similar detector response is seen in the extended central region that includes the central region of each module as well as the 'side' regions that are sandwiched between two central regions. This comprises the region $-20\,\text{m} \leq x \leq 20\,\text{m}$, $-4\,\text{m} \leq y \leq 4\,\text{m}$, and the entire z region, that is, about 42% of ICAL. As expected, the muon response is worse in the peripheral regions of the detector [117]. Studies show that the reconstruction efficiencies drop by about 10% while the charge identification efficiency drops from 98% in the central to about 96% in the peripheral region for a few GeV muons. Further, the momentum resolution worsens from $\sigma/P \sim 10\%$ to about 12–15% while the direction resolution remains the same. Hence, this will worsen the physics results that we will obtain, although not drastically. Note that the hadron resolutions are not altered on inclusion of the entire volume of ICAL, mainly because it is independent of the magnetic field. We do not comment further on this

in this paper, and present all results using the central region resolutions described earlier.

5.1 *Charged-current ν_μ events in ICAL*

We focus on the charged-current events from the atmospheric ν_μ interactions, that produce muons in the ICAL. We shall start by dividing them into bins of energy and momenta, taking into account the efficiencies and resolutions obtained in §4. As its output, the generator provides the 4-momentum (p^μ) of the initial, intermediate, and the final-state particles for each event. To reduce the Monte Carlo fluctuations in the events obtained, we generate an event sample corresponding to 1000 years of running of ICAL and scale it down to the desired exposure for the χ^2 analysis. The ICAL sensitivities presented here can then be interpreted as median sensitivities (in the frequentist sense), as described in [118]. Using 1000 years of data takes us closer to the ideal 'Asimov' dataset [119] that has no statistical fluctuations.

In the oscillated event sample, the total number of μ^- events come from the combination of the $\nu_\mu \to \nu_\mu$ and the $\nu_e \to \nu_\mu$ channels as

$$\frac{\mathrm{d}^2N}{\mathrm{d}E_\nu\,\mathrm{d}(\cos\theta_\nu)} = N_T\,N_D\,\sigma_{\nu_\mu}\left[P_{\mu\mu}\frac{\mathrm{d}^2\Phi_{\nu_\mu}}{\mathrm{d}E_\nu\,\mathrm{d}(\cos\theta_\nu)} + P_{e\mu}\frac{\mathrm{d}^2\Phi_{\nu_e}}{\mathrm{d}E_\nu\,\mathrm{d}(\cos\theta_\nu)}\right], \tag{5.1}$$

where N_D is the number of targets and N_T is the exposure time of the detector. Here Φ_{ν_μ} and Φ_{ν_e} are the fluxes of ν_μ and ν_e, respectively, and $P_{\alpha\beta}$ is the $\nu_\alpha \to \nu_\beta$ oscillation probability. The first term in eq. (5.1) corresponds to the number of μ^- events from ν_μ that have survived oscillations, while the second term corresponds to the oscillated ν_e flux into ν_μ.

The oscillation probabilities $P_{\mu\mu}$ and $P_{e\mu}$ are calculated numerically for any given set of oscillation parameters for each event, corresponding to the neutrino energy and zenith angle associated with it. As it takes a long time to run the NUANCE code to generate such a large event sample, generating events for each set of possible oscillation parameters is practically impossible. Therefore, we run the event generator only once for no oscillations and thereafter incorporate the oscillations using the 'reweighting' algorithm, which works as follows:

In order to implement the effects of oscillation on a ν_μ, a random number R between 0 and 1 is generated. If $R < P_{\mu e}$, the event is classified as a ν_e event. If $R > (P_{\mu e} + P_{\mu\mu})$, then we classify the event as a ν_τ event. If $P_{\mu e} \le R \le (P_{\mu e} + P_{\mu\mu})$, then it means that this event has come from an atmospheric ν_μ which has survived as a ν_μ and is hence selected as a muon neutrino event. The effects of oscillation on the ν_e events are implemented similarly, where the muon events are a result of oscillated ν_e events with a probability $P_{e\mu}$. The net number of muon events is obtained by adding the 'survived' and the 'oscillated' ν_μ events, as shown in eq. (5.1).

The μ^+ events in the detector are generated using a similar procedure. This final data sample is then binned in energy and zenith angle bins. Figure 5.1 shows the zenith angle distribution of μ^- events in the muon energy bin $E_\mu = 2$–3 GeV, before and after invoking oscillations. We use the oscillation parameters described in table 1.1 and take the exposure to be 50 kt × 10 years.

These are the events in an ideal detector. To proceed further, we apply the muon reconstruction efficiencies and resolutions (in both energy and direction) obtained in the previous section. The reconstruction efficiency (ϵ_{R-}) and the charge identification (CID) efficiencies (ϵ_{C-} for μ^- and ϵ_{C+} for μ^+ event sample) are applied as follows:

$$N^C_{\mu^-} = \epsilon_{C-}\,N_{\mu^-} + (1-\epsilon_{C+})N_{\mu^+}\,, \tag{5.2}$$

with

$$N_{\mu^-} = \epsilon_{R-}\,N^{\mathrm{true}}_{\mu^-}\,, \tag{5.3}$$

where $N^{\mathrm{true}}_{\mu^-}$ is the number of μ^- events in a given (E_μ, $\cos\theta_{\mu_{hyperlink}}$) bin. All the quantities appearing in eq. (5.2) are functions of E_μ and $\cos\theta_\mu$, and are determined bin-wise. The same procedure is applied for determining the μ^+ events.

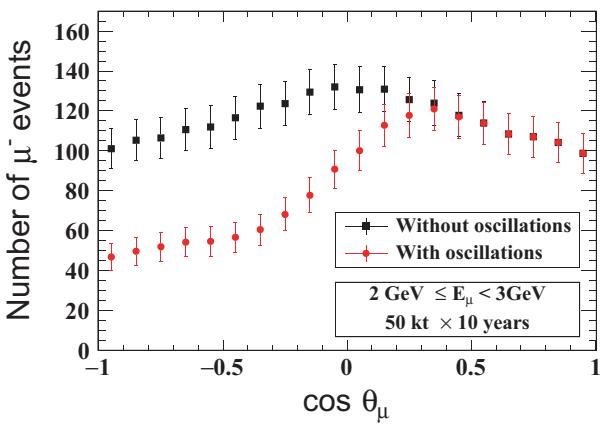

Figure 5.1. Zenith angle distribution of μ^- events for the bin 2 GeV $\le E_\mu <$ 3 GeV, without and with flavour oscillations. The detector efficiencies have not been included here. The error bars shown are statistical [11].

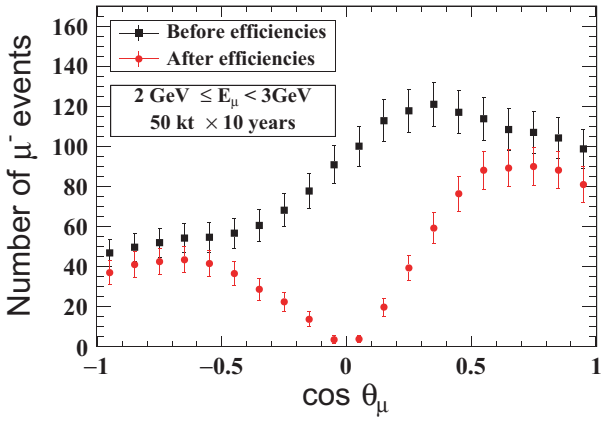

Figure 5.2. Zenith angle distribution of oscillated μ^- events for the bin 2 GeV $\leq E_\mu <$ 3 GeV, after taking into account the detector efficiencies. The error bars shown are statistical [11].

Figure 5.2 shows the zenith angle distribution of events obtained before and after applying the reconstruction and CID efficiencies. Compared to figure 5.1, one can notice that the number of events fall sharply for the almost horizontal ($\cos\theta_\mu \approx 0$) bins because the reconstruction efficiency for muons falls as we go to more horizontal bins as the iron slabs and RPCs in ICAL are stacked horizontally. As a result, there are hardly any events for bins with $-0.2 \leq \cos\theta_\mu < 0.2$.

Finally, the muon resolutions σ_E and $\sigma_{\cos\theta}$ are applied as follows:

$$(N^D_{\mu^-})_{ij}(E,\cos\theta) = \sum_k \sum_l N^C_{\mu^-}(E^k_\mu, \cos\theta^l_\mu) \times K^k_i(E^k_\mu) M^l_j(\cos\theta^l_\mu), \quad (5.4)$$

where $(N^D_{\mu^-})_{ij}$ denotes the number of muon events in the ith E-bin and the jth $\cos\theta$-bin after applying the energy and angle resolutions. Here, E and $\cos\theta$ are the measured muon energy and zenith angle. The summation is over the true energy bin k and true zenith angle bin l, with E^k_μ and $\cos\theta^l_\mu$ being the central values of the kth true muon energy and lth true muon zenith angle bin. The quantities K^k_i and M^l_j are the integrals of the detector resolution functions over the bins of E and $\cos\theta$, the measured energy and direction of the muon, respectively. These are evaluated as

$$K^k_i(E^k_\mu) = \int_{E_{L_i}}^{E_{H_i}} \mathrm{d}E \frac{1}{\sqrt{2\pi}\sigma_{E^k_\mu}} \exp\left(-\frac{(E^k_\mu - E)^2}{2\sigma^2_{E^k_\mu}}\right), \quad (5.5)$$

and

$$M^l_j(\cos\theta^l_\mu) = \int_{\cos\theta_{L_j}}^{\cos\theta_{H_j}} \mathrm{d}\cos\theta \frac{1}{\sqrt{2\pi}\sigma_{\cos\theta^l_\mu}} \times \exp\left(-\frac{(\cos\theta^l_\mu - \cos\theta)^2}{2\sigma^2_{\cos\theta^l_\mu}}\right), \quad (5.6)$$

where $\sigma_{E^k_\mu}$ and $\sigma_{\cos\theta^l_\mu}$ are the energy and zenith angle resolutions, respectively, in these bins, as obtained in §4. We perform the integrations between the lower and upper boundaries of the measured energy (E_{L_i} and E_{H_i}) and the measured zenith angle ($\cos\theta_{L_j}$ and $\cos\theta_{H_j}$). For the extreme $\cos\theta$ bins, the bins are taken to be $(-\infty, -0.9)$ and $[0.9, +\infty)$ while integrating, and the events are assigned to the bins $[-1, -0.9]$ and $[0.9, 1]$, respectively. This ensures that no event is lost to the unphysical region and the total number of events does not change after applying the angular resolution. For $E^k_\mu < 1$ GeV, the integrand in eq. (5.5) is replaced with the Landau distribution function. Figure 5.3 shows the zenith angle distribution of μ^- events before and after folding in the resolution functions. The angular dependence seems to get only slightly diluted. This is due to the good angular resolution of the detector.

Table 5.1 shows the total number of muon events with the measured energy range 0.8–10.8 GeV at various stages of the analysis for an exposure of 50 kt × 10 years. Note the sharp fall in statistics due to the reconstruction efficiencies. The reconstruction efficiencies are particularly poor for the near-horizontal bins where the reconstruction of the muon tracks is very hard. The small increase in the number of events after

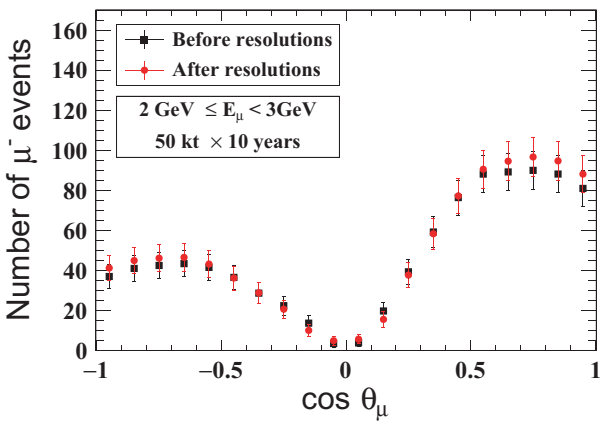

Figure 5.3. Zenith angle distribution of μ^- events for the bin 2 GeV $\leq E_\mu <$ 3 GeV before and after including energy and zenith angle resolution function. Here E and θ are the measured energy and measured zenith angle, respectively. The error bars shown are statistical [11].

Table 5.1. Number of muon events produced in CC ν_μ interactions at various stages of analysis for an exposure of 50 kt × 10 years in the energy range 0.8–10.8 GeV.

	μ^-	μ^+
Unoscillated	14311	5723
Oscillated	10531	4188
After applying reconstruction and CID efficiencies	4941	2136
After applying $(E, \cos\theta)$ resolutions	5270	2278

applying the energy resolution function is due to the spillover of events from the low-energy part of the spectrum to measured energies greater than 0.8 GeV. The spillover to the energy bins with $E_\mu > 10.8$ GeV is comparatively small. The zenith angle resolution leaves the number of muon events nearly unchanged.

5.2 *Analysis with E_μ and $\cos\theta_\mu$*

In this analysis, we use only the information in muon energy and muon direction. These two quantities can be measured with a good precision, much better than the precision on hadron energy. Therefore, we ignore the latter for now. We shall include the hadron information in our analysis in the next two sections.

We generate the data at the benchmark true values for oscillation parameters given in table 1.1. We define χ^2 for the ICAL data as

$$\chi^2(\mu^-) = \min_{\{\xi_k\}} \sum_{i,j} \left[2\,(N_{ij}^{\text{theory}}(\mu^-) - N_{ij}^{\text{data}}(\mu^-)) + 2N_{ij}^{\text{data}}(\mu^-) \ln\left(\frac{N_{ij}^{\text{data}}(\mu^-)}{N_{ij}^{\text{theory}}(\mu^-)}\right)\right] + \sum_k \xi_k^2, \tag{5.7}$$

where

$$N_{ij}^{\text{theory}}(\mu^-) = N_{ij}^{0\ \text{theory}}(\mu^-)\left(1 + \sum_{k=1}^{l} \pi_{ij}^k \xi_k\right). \tag{5.8}$$

Here we use the linearized approximation while using the method of pulls. We have assumed a Poissonian distribution for the errors in this definition of χ^2. The reason is that the number of events falls sharply with energy due to the falling flux (see figure 2.3) and for small exposure times these bins can have very few events per bin. As ICAL will have separate data in μ^- and μ^+, we calculate $\chi^2(\mu^-)$ and $\chi^2(\mu^+)$ separately for the μ^- sample and the μ^+ sample respectively and then add the two to get total χ^2 as

$$\chi^2 = \chi^2(\mu^-) + \chi^2(\mu^+). \tag{5.9}$$

In the above equations, $N_{ij}^{\text{data}}(\mu^-)$ and $N_{ij}^{\text{data}}(\mu^+)$ are the observed number of μ^- and μ^+ events respectively in the ith energy and jth angle bin and $N_{ij}^{0\ \text{theory}}(\mu^-)$ and $N_{ij}^{0\ \text{theory}}(\mu^+)$ are the corresponding theoretically predicted event spectrum. This predicted event spectrum can shift due to the systematic uncertainties, which is taken care of by the method of pulls [120,121]. The shifted spectrum N_{ij}^{theory} is given by eq. (5.8), where π_{ij}^k is the kth systematic uncertainty in the ijth bin and ξ_k is the pull variable corresponding to the uncertainty π^k. χ^2 is minimized over the full set of pull variables $\{\xi_k\}$. In our analysis we have considered the muon energy range 0.8 GeV–10.8 GeV with 10 bins of bin size 1 GeV. The zenith angle range in $\cos\theta$ is taken from -1 to $+1$, with 80 bins of bin size 0.025. Note that the zenith angle resolution of ICAL is $\sim$0.01 in $\cos\theta_\mu$ over the entire parameter range of interest, the number of zenith angle bins is limited to ensure enough number of events in individual bins.

The index k in eqs (5.7) and (5.8) runs from 1 to l, where l is the total number of systematic uncertainties. We have included the following five systematic uncertainties in our analysis [122]:

- an overall flux normalization error of 20%,
- an overall cross-section normalization error of 10%,
- a 5% uncertainty on the zenith angle dependence of the fluxes,
- an overall 5% energy-independent systematic uncertainty, and
- an energy-dependent 'tilt factor', incorporated according to the following prescription. The event spectrum is calculated with the predicted atmospheric neutrino fluxes and then with the flux spectrum shifted according to

$$\Phi_\delta(E) = \Phi_0(E)\left(\frac{E}{E_0}\right)^\delta \simeq \Phi_0(E)\left(1 + \delta\,\ln\frac{E}{E_0}\right), \tag{5.10}$$

where $E_0 = 2$ GeV and δ is the 1σ systematic error which we have taken as 5% [123]. The difference between the predicted event rates for the two cases is then included in the statistical analysis.

5.2.1 *Mass hierarchy sensitivity*. Figure 5.4 shows the discovery potential of ICAL alone for the neutrino

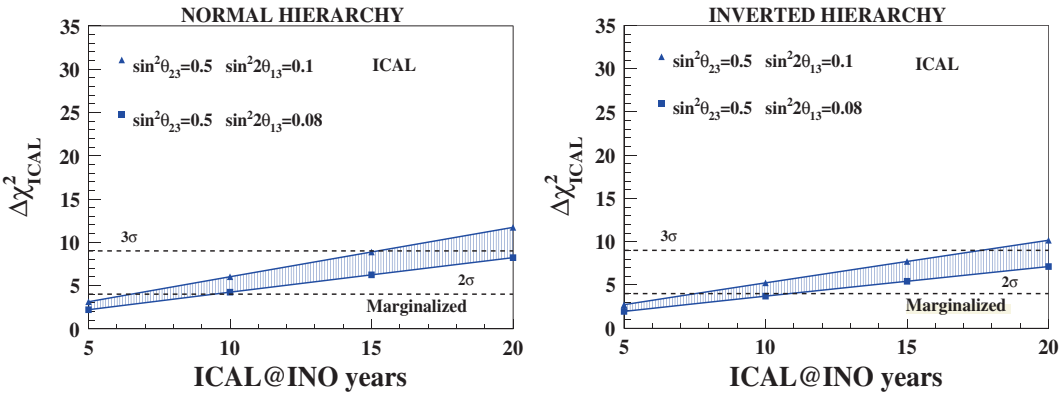

Figure 5.4. Left panel shows $\Delta\chi^2$ for the wrong hierarchy when normal hierarchy is taken to be true, while the right panel shows the corresponding reach when inverted hierarchy is taken as true. The bands correspond to $\sin^2 2\theta_{13}$(true) in the range 0.08–0.1 as shown in the legend box, while $\sin^2\theta_{23}$(true) $= 0.5$ for all cases. We take only ICAL 'muon' data in the analysis and marginalize over oscillation parameters $|\Delta m^2_{\rm eff}|$, $\sin^2\theta_{23}$, and $\sin^2 2\theta_{13}$, which are allowed to vary freely within their 3σ ranges given in table 1.1 [11].

mass hierarchy, as a function of the number of years of data taking of the 50 kt ICAL. The data are generated for the values of oscillation parameters given in table 1.1 and for $\sin^2\theta_{23}(\text{true}) = 0.5$ for a definite hierarchy. These simulated data are then fitted with the wrong mass hierarchy to check the statistical significance with which this wrong hierarchy can be disfavoured.

The bands in figure 5.4 correspond to $\sin^2 2\theta_{13}$(true) in the range 0.08–0.1. The left panel is for true normal hierarchy while the right panel is for true inverted hierarchy. In figure 5.4 the plots show the sensitivity reach of ICAL when χ^2 is marginalized over oscillation parameters $|\Delta m^2_{\rm eff}|$, $\sin^2\theta_{23}$, and $\sin^2 2\theta_{13}$, meaning these oscillation parameters are allowed to vary freely in the fit within the ranges shown in table 1.1, and the minimum of the χ^2 taken. The CP phase $\delta_{\rm CP}$ does not significantly impact the ICAL mass hierarchy sensitivity. (This will be discussed in some detail later.) Therefore, we keep $\delta_{\rm CP}$ fixed at 0 in the fit. The parameters Δm^2_{21} and $\sin^2\theta_{12}$ also do not affect χ^2 and hence are kept fixed at their true values given in table 1.1. From the figure we see that for full marginalization within the current 3σ allowed range for $|\Delta m^2_{\rm eff}|$, $\sin^2\theta_{23}$ and $\sin^2 2\theta_{13}$, the sensitivity reach of ICAL with 10 (5) years data would be only about 2.2σ (1.6σ) for $\sin^2\theta_{23}(\text{true}) = 0.5$ and $\sin^2 2\theta_{13}(\text{true}) = 0.1$, for true normal hierarchy. The impact for the case of inverted hierarchy is seen to be marginally worse.

We shall further explore the effects of priors, systematic uncertainties, and the true value of θ_{23} in some detail. The lessons learnt from this study will be applied directly to later analyses.

5.3 *Impact of priors*

All values of the oscillation parameters are not allowed with equal CL by the current data. Moreover, all oscillation parameters are expected to be measured with much better precision by the ongoing and upcoming neutrino experiments. In fact, by the time ICAL is operational, all of the current accelerator-based and reactor experiments would have completed their scheduled runs and hence we expect that by then significant improvements in the allowed ranges of oscillation parameters would have been made. In particular, we expect improvement in the values of $\sin^2 2\theta_{13}$, $|\Delta m^2_{\rm eff}|$, and $\sin^2 2\theta_{23}$. One could incorporate this information into the analysis by including 'priors' on these parameters, through

$$\chi^2_{\rm ICAL} = \chi^2 + \sum \chi^2_{\rm prior}, \quad \chi^2_{\rm prior}(p) = \frac{(p_0 - p)^2}{\sigma_0^2}\ , \tag{5.11}$$

where $\chi^2 = \chi^2_+ + \chi^2_-$ as in eq. (5.9), p is the parameter on which a prior is included and p_0 and σ_0 are its best fit and 1σ error, respectively. For our analysis, we take the 1σ error on $\sin^2 2\theta_{13}$ to be 0.1 (a bit conservative, given the current measurements), and take $|\Delta m^2_{\rm eff}|$ and $\sin^2 2\theta_{23}$ to be determined with an accuracy of 2 and 0.65%, respectively.

The sensitivity reach of ICAL with projected priors on $|\Delta m^2_{\rm eff}|$, $\sin^2 2\theta_{23}$, and $\sin^2 2\theta_{13}$ keeping other parameters fixed is shown in figure 5.5. We can note from these plots that with 5 years of ICAL data alone, we shall have a 1.8σ (1.8σ) signal for the wrong hierarchy if normal (inverted) hierarchy is true. After 10 years of ICAL data, this will improve to 2.5σ (2.5σ)

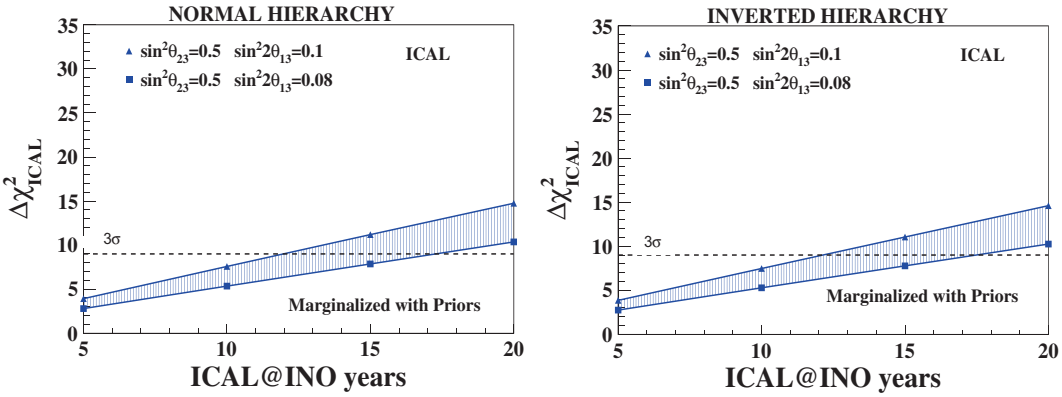

Figure 5.5. Same as figure 5.4 but here we impose priors while marginalizing over $|\Delta m^2_{\text{eff}}|$, $\sin^2\theta_{23}$, and $\sin^2 2\theta_{13}$, as discussed in the text [11].

signal for the wrong hierarchy if normal (inverted) hierarchy is true. The sensitivity obviously increases with the true value of $\sin^2 2\theta_{13}$(true). The $\Delta\chi^2$ value is seen to increase almost linearly with exposure. This is not hard to understand as the hierarchy sensitivity comes from the difference in the number of events between normal and inverted hierarchies due to Earth matter effects. As this is a small difference, the relevant statistics in this measurement is small. As a result, the mass hierarchy analysis is statistics-dominated and the $\Delta\chi^2$ value increases linearly with exposure.

5.4 *Impact of systematic uncertainties*

The systematic uncertainties, mainly due to the uncertainties in the atmospheric neutrino fluxes, have already been included in the above analysis, through the method of pulls [120,121] as described in §5.2.1. An analysis of the extent of the impact of these uncertainties will give us an idea of how much the reduction in these uncertainties will help. In figure 5.6 we show the mass hierarchy sensitivity with and without systematic uncertainties in the ICAL analysis. $\Delta\chi^2$ value is shown as a function of the number of years of exposure of the experiment. The data were generated at the benchmark oscillation point.

The effect of taking systematic uncertainties is to reduce the statistical significance of the analysis. We have checked that of the five systematic uncertainties, the uncertainty on overall normalization of the fluxes and the cross-section normalization uncertainty have minimal impact on the final results. The reason for that can be understood from the fact that the atmospheric neutrinos come from all zenith angles and over a wide range of energies. The overall normalization uncertainty is the same for all bins, while the mass hierarchy-dependent Earth matter effects are important only in certain zenith angle bins and certain range of

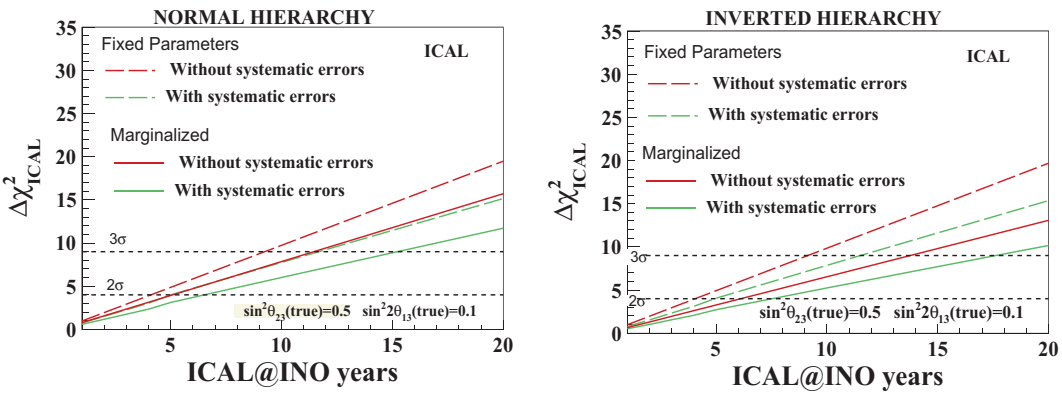

Figure 5.6. The impact of systematic uncertainties on mass hierarchy sensitivity. The red lines are obtained without taking systematic uncertainties in the ICAL analysis, while the green lines are obtained when systematic uncertainties are included. Long-dashed lines are for fixed parameters in theory as in data, while solid lines are obtained by marginalizing over $|\Delta m^2_{\text{eff}}|$, $\sin^2\theta_{23}$, and $\sin^2 2\theta_{13}$ [11].

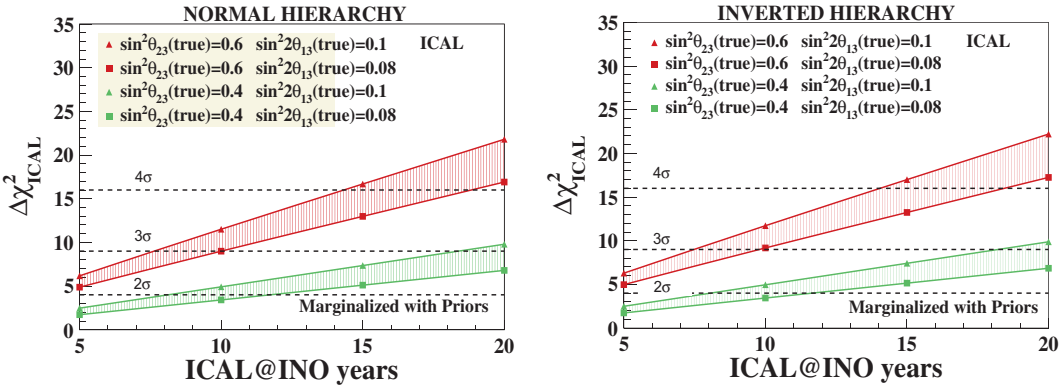

Figure 5.7. Same as figure 5.5 but for $\sin^2\theta_{23}(\text{true}) = 0.4$ (green band) and $\sin^2\theta_{23}(\text{true}) = 0.6$ (red band). The width of each of the band is mapped by increasing the value of $\sin^2 2\theta_{13}(\text{true})$ from 0.08 to 0.1.

energies. Therefore, the effects of the overall normalization errors get cancelled between different bins. On the other hand, the tilt error can be used to modify the energy spectrum of the muons in the fit and the zenith angle error allows changes to the zenith angle distribution. Therefore, these errors do not cancel between the different bins and can dilute the significance of the data. In particular, we have checked that the effect of the zenith angle-dependent systematic error on the atmospheric neutrino fluxes has the maximum effect on the lowering of $\Delta\chi^2$ for the mass hierarchy sensitivity.

5.5 *Impact of the true value of* $\sin^2\theta_{23}$

The mass hierarchy sensitivity of the ICAL will depend strongly on the actual value of θ_{23}. The amount of Earth matter effects increases with increase in both θ_{13} and θ_{23}. In the previous plots, we have seen mass hierarchy sensitivity for different allowed values of $\sin^2 2\theta_{13}(\text{true})$, while $\sin^2\theta_{23}(\text{true})$ was fixed at maximal mixing. In figure 5.7 we show the sensitivity to the neutrino mass hierarchy as a function of the number of years of running of ICAL for different values of $\sin^2 2\theta_{13}(\text{true})$ as well as $\sin^2\theta_{23}(\text{true})$. As seen in the previous subsection, $\Delta\chi^2$ for the wrong mass hierarchy increases with $\sin^2 2\theta_{13}(\text{true})$ for a given value of $\sin^2\theta_{23}(\text{true})$ and ICAL exposure. A comparison of $\Delta\chi^2$ for different values of $\sin^2\theta_{23}(\text{true})$ reveals that $\Delta\chi^2$ also increases with $\sin^2\theta_{23}(\text{true})$.

5.6 *(In)sensitivity to the CP-violating phase*

In the analyses above, the true value for the CP-violating phase δ_{CP} has been taken to be 0°, and this parameter has not been marginalized over. The reason for this is that atmospheric neutrino data are insensitive to this phase [18,122]. In order to illustrate this, we show figure 5.8 where the data with 500 kt-yr exposure are generated for $\delta_{\text{CP}} = 0$, and the fit is tried for all δ_{CP} values. It can be observed that the hierarchy sensitivity is not affected by what value of δ_{CP} we choose to fit the data with. We have checked that the same results hold for any actual δ_{CP} value, that is the hierarchy sensitivity of ICAL is independent of the actual value of δ_{CP}.

The reason behind the insensitivity of ICAL to the actual value of δ_{CP} lies in the fact that the muon neutrinos at ICAL come dominantly from the original unoscillated muon neutrinos, while the muon neutrinos coming from the oscillated electron neutrinos are a smaller fraction, partly due to the smallness of the electron neutrino flux, but mostly due to the small value of the conversion probability $P_{e\mu}$ owing to the smallness

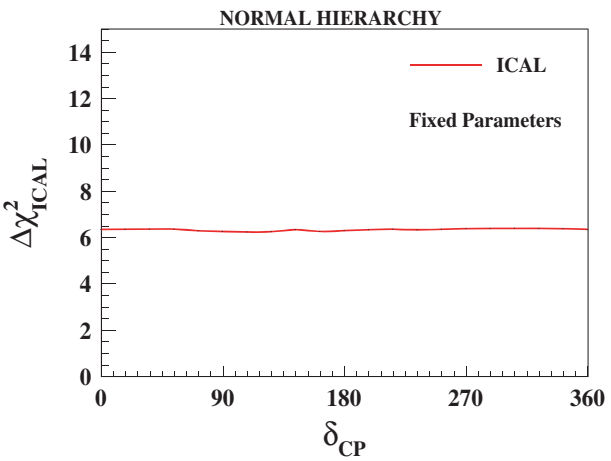

Figure 5.8. The hierarchy sensitivity at different assumed values of δ_{CP} with 500 kt-yr of ICAL data, when the data are generated with the actual value $\delta_{\text{CP}} = 0$.

of θ_{13} and $\Delta m^2_{21}/\Delta m^2_{31}$ (see Appendix B). The survival probability $P_{\mu\mu}$ therefore controls the oscillations detected at ICAL. In $P_{\mu\mu}$, the CP-violating phase δ_{CP} appears as a subdominant term that oscillates as $\cos\Delta$, where the oscillation phase $\Delta \equiv \Delta m^2_{31} L/(4E)$ (see Appendix B). If the distance L travelled by the neutrino is uncertain by δL, this phase becomes uncertain by $\delta\Delta \approx \Delta(\delta L/L)$. For a few GeV neutrinos travelling distances of a few thousands of km through the Earth matter, $\Delta \sim 10$. Hence, only a 10% uncertainty in L can wipe out the information about the phase Δ, and hence about the dependence on δ_{CP}. It is indeed difficult to determine the direction of incoming neutrino, and hence the value of L, for an atmospheric neutrino. Another added factor is the uncertainty in energy, which also contributes to the uncertainty in Δ as $\delta\Delta \approx \Delta(\delta E/E)$ in a similar way.

Note that this insensitivity of ICAL to the δ_{CP}-dependent oscillating term is already a part of our analysis, and so the capability of ICAL to distinguish between the two hierarchies is 'in spite of' this disadvantage. This may be contrasted with the hierarchy sensitivities of fixed-baseline experiments like T2K or NOνA, whose sensitivities to the mass hierarchy depend crucially on the actual δ_{CP} value. This issue will be discussed later in §6.

5.6.1 *Precision measurement of* $|\Delta m^2_{32}|$ *and* $\sin^2\theta_{23}$. The reach of ICAL for the parameters $\sin^2\theta_{23}$ and $|\Delta m^2_{32}|$ separately is shown in figure 5.9 in terms of the $\Delta\chi^2$ value compared to the best-fit value to the simulated data. The precision on these parameters may be quantified by

$$\text{Precision} = \frac{p_{\max} - p_{\min}}{p_{\max} + p_{\min}}, \tag{5.12}$$

where $p_{\max}$ and $p_{\min}$ are the largest and smallest value of the concerned oscillation parameter, determined at the given CL from the atmospheric neutrino measurements at ICAL, for a given exposure. We find that after five years of data taking, ICAL will be able to measure $\sin^2\theta_{23}$ to a precision of 20% and $|\Delta m^2_{32}|$ to 7.4% at 1σ. With 10 years exposure, these numbers are expected to improve to 17 and 5.1% for $\sin^2\theta_{23}$ and $|\Delta m^2_{32}|$, respectively. The precision on $\sin^2\theta_{23}$ is mainly governed by the muon reconstruction efficiency and is expected to improve with it. It will also improve as the systematic uncertainties are reduced. If the flux normalization error were to come down from 20 to 10%, the precision on $\sin^2\theta_{23}$ will improve to 14% for 10 years of exposure. Reducing the zenith angle error from 5 to 1% will also improve this precision to ~14%. On the other hand, the precision on $|\Delta m^2_{32}|$ is governed by the ability of the detector to determine the value of L/E for individual event accurately. This depends on the energy and $\cos\theta$ resolution of the detector.

A few more detailed observations may be made from the χ^2 plots in figure 5.9. From figure 5.9a one can notice that the precision on θ_{23} when it is in the first octant ($\sin^2\theta_{23} < 0.5$) is slightly better than when it is in the second octant ($\sin^2\theta_{23} > 0.5$), even though the muon neutrino survival probability depends on $\sin^2 2\theta_{23}$ at the leading order. This asymmetry about $\sin^2\theta_{23} = 0.5$ stems mainly from the full three-flavour analysis that we have performed in this study. In particular, we have checked that the non-zero value of θ_{13} is responsible for the asymmetry observed in this figure. On the other hand, χ^2 asymmetry about the true value of $|\Delta m^2_{32}|$ observed in figure 5.9b is an effect that is present even with a two-flavour analysis.

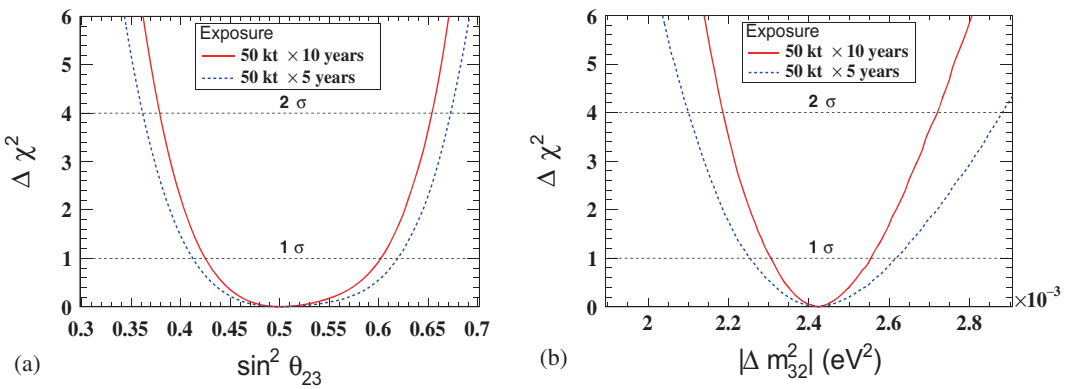

Figure 5.9. The panel (a) shows χ^2 as a function of $\sin^2\theta_{23}$ for $|\Delta m^2_{32}| = 2.4 \times 10^{-3}$ eV^2 and $\sin^2\theta_{23}$(true) $= 0.5$. The panel (b) shows χ^2 as a function of $|\Delta m^2_{32}|$ for $\sin^2\theta_{23} = 0.5$ and $|\Delta m^2_{32}|$(true) $= 2.4 \times 10^{-3}$ eV^2. Only muon information has been used [12].

The precisions obtainable at ICAL for $\sin^2\theta_{23}$ and $|\Delta m^2_{32}|$ are expected to be correlated. We therefore present the correlated reach of ICAL for these parameters in figures 5.10a and 5.10b. As noted above, our three-neutrino analysis should be sensitive to the octant of θ_{23}. Therefore, we choose to present our results in terms of $\sin^2\theta_{23}$ instead of $\sin^2 2\theta_{23}$. Though the constant-χ^2 contours still look rather symmetric about $\sin^2\theta_{23} = 0.5$, that is mainly due to the true value of $\sin^2\theta_{23}$ being taken to be 0.5. The values of $\sin^2\theta_{23}$ away from 0.5 will make the contours asymmetric and will give rise to some sensitivity to the octant of θ_{23}, as we shall see later.

5.6.2 *Sensitivity to the octant of* θ_{23}. Earth matter effects in atmospheric neutrinos can be used to distinguish maximal from non-maximal θ_{23} mixing and can lead to the determination of the correct θ_{23} octant [124–126]. We show in figure 5.11 the potential of 10 years of ICAL run for distinguishing a non-maximal value of θ_{23} from maximal mixing in the case where $\sin^2 2\theta_{23} = 0.90$ ($\sin^2\theta_{23} = 0.342,\ 0.658$) and $\sin^2 2\theta_{23} = 0.95$ ($\sin^2\theta_{23} = 0.388,\ 0.612$). The figure shows that, if the value of θ_{23} is near the current 3σ bound and in the first octant, then it may be possible to exclude maximal mixing to 99% CL with this 2-parameter analysis. If θ_{23} is in the second octant, or if $\sin^2 2\theta_{23}$ is larger than 0.9, the exclusion of the maximal mixing becomes a much harder task.

Figure 5.11 can also be used to quantify the reach of ICAL for determining the correct octant of θ_{23}, if the value of $\sin^2 2\theta_{23}$ is known. This can be seen by comparing the χ^2 value corresponding to the true value of $\sin^2\theta_{23}$, but in the wrong octant, with that corresponding to the true value of $\sin^2\theta_{23}$. We find that, for $\sin^2 2\theta_{23} = 0.9$, i.e. just at the allowed 3σ bound, the octant can be identified at >95% CL with 10 years of ICAL run if θ_{23} is in the first octant. However, if θ_{23} is in the second octant, the identification of the octant will be much harder: θ_{23} in the wrong octant can be disfavoured only to about 85% CL. The situation is worse if $\sin^2 2\theta_{23}$ is closer to unity.

The precision on $|\Delta m^2_{32}|$ will keep improving with ongoing and future long-baseline experiments. The inclusion of the information may improve the chance of ICAL being able to identify deviation of θ_{23} from maximal mixing and its octant to some extent.

We would like to remind the reader that all the results in this section (§5.2.1) use only the information on muon energy and direction. The addition of hadron information is expected to improve the physics reach of ICAL in all aspects, and this will be explored in the next sections.

5.7 *Analysis with* E_ν *and* $\cos\theta_\mu$

The addition of the value of hadron energy $E'_{\rm had}$, calibrated with respect to the number of hadronic hits as described in §4, to the muon energy E_μ reconstructs the incoming neutrino energy in a charged-current interaction. Since it is the neutrino energy that appears in the neutrino oscillation probabilities, it is conceivable that direct access to neutrino energy will improve the reach of the ICAL to the oscillation parameters.

The analyses in this section and the next that use the hadron energy information assume that the hits created by a muon and hadron can be separated with a

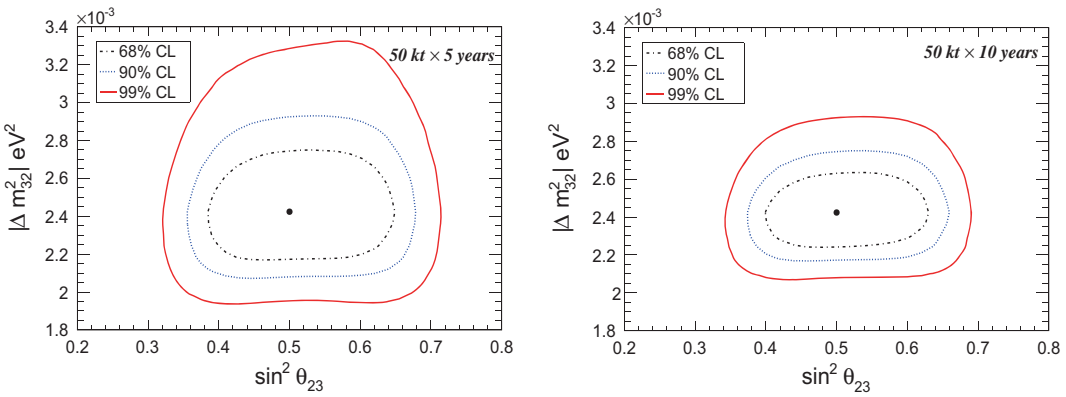

(a) Precision reach for 5 years run (b) Precision reach for 10 years run

Figure 5.10. The precision reach expected at ICAL in the $\sin^2\theta_{23}$–$|\Delta m^2_{32}|$ plane at various confidence levels, using only muon information. The black, blue, and red lines show 68, 90, and 99% CL contours. The true values of $\sin^2\theta_{23}$ and $|\Delta m^2_{32}|$ used for generating data are shown by the black dots. The true values of other parameters used are given in table 1.1. Panel (a) is for five-year running of the 50 kt detector while (b) is for ten-year exposure [12].

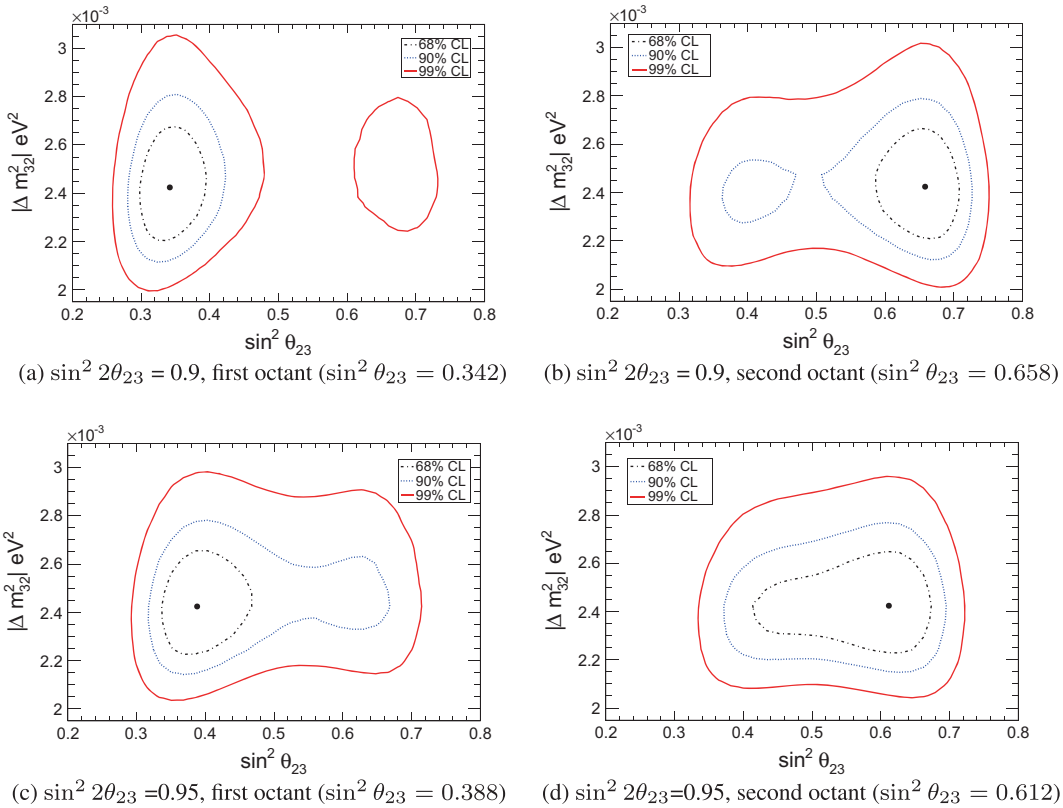

(a) $\sin^2 2\theta_{23} = 0.9$, first octant ($\sin^2\theta_{23} = 0.342$) (b) $\sin^2 2\theta_{23} = 0.9$, second octant ($\sin^2\theta_{23} = 0.658$)

(c) $\sin^2 2\theta_{23} = 0.95$, first octant ($\sin^2\theta_{23} = 0.388$) (d) $\sin^2 2\theta_{23} = 0.95$, second octant ($\sin^2\theta_{23} = 0.612$)

Figure 5.11. The projected reach in the $\sin^2\theta_{23}$–$|\Delta m^2_{32}|$ plane for four different non-maximal choices of θ_{23}. The black, blue and red lines show 68, 90, and 99% CL contours for 10 years of 50 kt ICAL run, using only muon information. Note that we use normal hierarchy, and assume that it is already known [12].

100% efficiency by the ICAL particle reconstruction algorithm. Then, whenever a muon is reconstructed, the corresponding hadron hits can always be considered to be a hadron shower, so that the energy $E'_{\rm had}$ can be reconstructed. This implies that the neutrino event reconstruction efficiency is the same as the muon reconstruction effciency. (Note that the calibration of $E'_{\rm had}$ against the number of hadron shower hits also allows for the possibility of no hits observed in the hadron shower.) Finally, the background hits coming from other sources such as the neutral-current events, charged-current ν_e events, cosmic muons and noise, have not been taken into account so far. The systematics due to these effects will have to be taken care of in future, as the understanding of the ICAL detector improves.

The neutrino energy E_ν is reconstructed as the sum of the reconstructed muon energy E_μ (§4.1) and the calibrated hadron energy $E'_{\rm had}$ (§4.2). The muon energy resolutions and zenith angle resolutions have been implemented by smearing the true muon energy and direction of each μ^+ and μ^- event, as discussed earlier. Energy of hadron events has also been smeared separately, following the discussion in §4.2. The reconstructed neutrino energy is then taken as the sum of reconstructed muon energy and hadron energy, with the uncertainties calculated separately for each event. The events are then binned in $(E_\nu, \cos\theta_\mu)$ bins: 15 equal E_ν bins in the range [0.8, 5.8] GeV, 5 equal E_ν bins in the range [5.8, 10.8] GeV, and 20 equal $\cos\theta_\mu$ bins in the range $[-1.0, 1.0]$. The same analysis as in §5.2 is then performed, marginalizing over the 3σ allowed ranges of $|\Delta m^2_{32}|$, $\sin^2\theta_{23}$, and θ_{13}, with a 10% prior on θ_{13}. The systematic errors have been taken into account using the method of pulls as before.

Figure 5.12 shows the sensitivity of ICAL to the atmospheric mixing parameters $|\Delta m^2_{\rm eff}|$ and $\sin^2\theta_{23}$, where $\Delta m^2_{\rm eff} \equiv \Delta m^2_{32} - (\cos^2\theta_{12} - \cos\delta_{\rm CP}\sin\theta_{32} \times \sin 2\theta_{12}\tan\theta_{23})\Delta m^2_{21}$ is the effective value of $\Delta m^2_{\rm atm}$ relevant for the two-neutrino analysis of atmospheric neutrino oscillations [6,7]. It is seen that with 10 years of data and the $(E_\nu, \cos\theta_\mu)$ analysis technique, the 50 kt ICAL can measure the magnitude of the atmospheric neutrino mass squared difference to 4% and $\sin^2\theta_{23}$ to 13%, at 1σ. A comparison of these numbers against those obtained using the $(E_\mu, \cos\theta_\mu)$ analysis shows that using the reconstructed neutrino energy

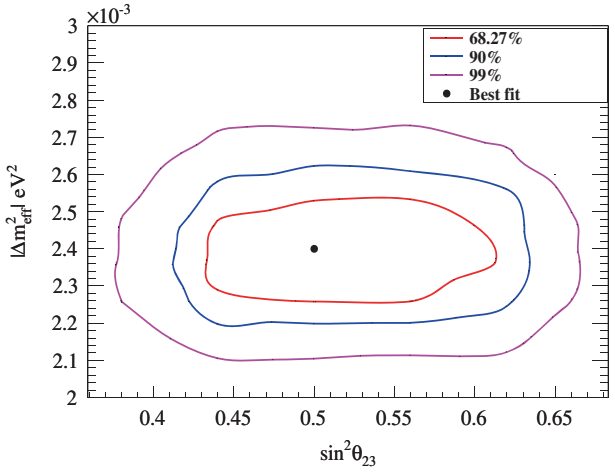

Figure 5.12. The reach of the ICAL for precision measurements of $|\Delta m^2_{\rm eff}|$ and $\sin^2\theta_{23}$, using information on E_ν and $\cos\theta_\mu$, for an exposure of 500 kt-yr. The contours with 68, 90, and 99% confidence level are shown [13].

improves the precision on $\sin^2\theta_{23}$ and $|\Delta m^2_{32}|$ by about 20%. However, the addition of the coarsely measured hadron energy to the accurately measured muon energy results in some loss of information, resulting in some degradation in the performance for mass hierarchy identification.

5.8 *Analysis using correlated information on* E_μ, $\cos\theta_\mu$, *and* $E'_{\rm had}$

The preceeding analyses have been performed by using only the information on muon direction, and the energy of muons or neutrinos. However, in each CC event at ICAL, the information on E_μ, $\cos\theta_\mu$ and $E'_{\rm had} \equiv E_\nu - E_\mu$ is available independently. Thus, the inelasticity $y \equiv E'_{\rm had}/E_\nu$ is an additional measurable quantity in each event. This advantage of ICAL may be exploited to enhance its physics reach [14], as will be seen in this section. This is implemented by performing an analysis that employs binning in all these three quantities, so that no information is lost and all correlations are taken care of.

5.8.1 *The three-dimensional binning.* For event generation and inclusion of oscillation, we use the same procedure as described in §5.2. After incorporating the detector response for muons and hadrons [8,9], the measured event distribution in terms of (E_μ, $\cos\theta_\mu$, $E'_{\rm had}$) is obtained. A three-dimensional binning scheme using the measured quantities E_μ, $\cos\theta_\mu$ and $E'_{\rm had}$ is employed for the χ^2 analysis. In order to ensure significant statistics in each bin and also to avoid large number of bins, we use a non-uniform binning scheme for each polarity as shown in table 5.2. Thus, for each polarity, one has a total of $(10 \times 21 \times 4) = 840$ bins.

For the statistical analysis, we define the Poissonian χ^2_- for the μ^- events as

$$\chi^2_- = \min_{\xi_l} \sum_{i=1}^{N_{E'_{\rm had}}} \sum_{j=1}^{N_{E_\mu}} \sum_{k=1}^{N_{\cos\theta_\mu}} \times \left[2(N^{\rm theory}_{ijk} - N^{\rm data}_{ijk}) - 2N^{\rm data}_{ijk} \ln\left(\frac{N^{\rm theory}_{ijk}}{N^{\rm data}_{ijk}}\right)\right] + \sum_{l=1}^{5} \xi_l^2 , \quad (5.13)$$

where

$$N^{\rm theory}_{ijk} = N^{0\ {\rm theory}}_{ijk}\left(1 + \sum_{l=1}^{5} \pi^l_{ijk}\xi_l\right). \quad (5.14)$$

Here $N^{\rm theory}_{ijk}$ and $N^{\rm data}_{ijk}$ are the expected and the observed number of μ^- events in a given (E_μ, $\cos\theta_\mu$, $E'_{\rm had}$) bin, with $N_{E'_{\rm had}} = 4$, $N_{E_\mu} = 10$, and $N_{\cos\theta_\mu} = 21$. The systematic uncertainties have been included by using

Table 5.2. The binning scheme in E_μ, $\cos\theta_\mu$, and $E'_{\rm had}$ for each polarity.

Observable	Range	Bin width	Total bins	
E_μ (GeV)	1–4	0.5	6	10
	4–7	1	3	
	7–11	4	1	
$\cos\theta_\mu$	(–1)–(–0.4)	0.05	12	21
	(–0.4) – 0	0.1	4	
	0–1	0.2	5	
$E'_{\rm had}$ (GeV)	0–2	1	2	4
	2–4	2	1	
	4–15	11	1	

the pull method [120,121], which uses the 'pull' variables ξ_l [11,12].

For μ^+ events, χ^2_+ is similarly defined. The total χ^2 is obtained as

$$\chi^2_{\text{ICAL}} = \chi^2_- + \chi^2_+ + \chi^2_{\text{prior}}\,, \tag{5.15}$$

where

$$\chi^2_{\text{prior}} \equiv \left(\frac{\sin^2 2\theta_{13} - \sin^2 2\theta_{13}(\text{true})}{0.08 \times \sin^2 2\theta_{13}(\text{true})}\right)^2. \tag{5.16}$$

The 8% prior on $\sin^2 2\theta_{13}$ corresponds to the current accuracy in the measurement of this quantity. No prior on θ_{23} or Δm^2_{32} is used because these parameters will be directly measured at the ICAL.

While implementing the minimization procedure, χ^2_{ICAL} is first minimized with respect to the pull variables ξ_l, and then marginalized over the 3σ allowed ranges of oscillation parameters $\sin^2\theta_{23}$, Δm^2_{eff}, and $\sin^2 2\theta_{13}$, wherever appropriate. We do not marginalize over δ_{CP}, Δm^2_{21}, and θ_{12} because they have negligible effect on the relevant oscillation probabilities at ICAL [18,122]. Also, $\delta_{\text{CP}} = 0$ throughout the analysis.

5.8.2 *Mass hierarchy sensitivity*. We quantify the statistical significance of the analysis to rule out the wrong hierarchy by

$$\Delta\chi^2_{\text{ICAL-MH}} = \chi^2_{\text{ICAL}}\,(\text{false MH}) - \chi^2_{\text{ICAL}}\,(\text{true MH}). \tag{5.17}$$

Here, $\chi^2_{\text{ICAL}}(\text{true MH})$ and $\chi^2_{\text{ICAL}}(\text{false MH})$ are obtained by performing a fit to the 'observed' data assuming true and false mass hierarchy, respectively.

Figure 5.13 shows the mass hierarchy sensitivity of ICAL as a function of the run-time of the experiment. It is found that after including the hadron energy information, 10 years of running of the 50 kt ICAL can rule out the wrong hierarchy with $\Delta\chi^2_{\text{ICAL-MH}} \approx 9.7$ (for true NH) and $\Delta\chi^2_{\text{ICAL-MH}} \approx 9.1$ (for true IH). In other words, the wrong hierarchy can be ruled out to about 3σ for either hierarchy. If the true values of θ_{23} and θ_{13} are varied over their allowed 3σ range, the corresponding range for $\Delta\chi^2_{\text{ICAL-MH}}$ after 10 years is 7–12. Compared to the results without using hadron information, with the same binning scheme, the value of $\Delta\chi^2_{\text{ICAL-MH}}$ increases by about 40% when the correlated hadron energy information is added. This improvement is not merely due to using additional bins compared to the muon-only analysis, as can be checked by comparing the results with those in §5.2.

5.8.3 *Precision measurement of atmospheric parameters*. In order to quantify the precision in the measurements of a parameter λ (here λ may be $\sin^2\theta_{23}$ or Δm^2_{32} or both), we use the quantity

$$\Delta\chi^2_{\text{ICAL-PM}}(\lambda) = \chi^2_{\text{ICAL}}(\lambda) - \chi^2_0, \tag{5.18}$$

where χ^2_0 is the minimum value of χ^2_{ICAL} in the allowed parameter range.

The two panels of figure 5.14 show the sensitivity of ICAL to the two parameters $\sin^2\theta_{23}$ and $|\Delta m^2_{32}|$ separately, where the other parameter has been marginalized over, along with θ_{13} and the two possible mass hierarchies. While the figure shows the results for NH as the true hierarchy, the results with true IH are almost identical. It may be observed from the figure that with the inclusion of hadron energy information, 500 kt-yr of ICAL exposure will be able to measure $\sin^2\theta_{23}$ to a 1σ precision of 12% and $|\Delta m^2_{32}|$ to a 1σ precision of 2.9%. This may be compared with

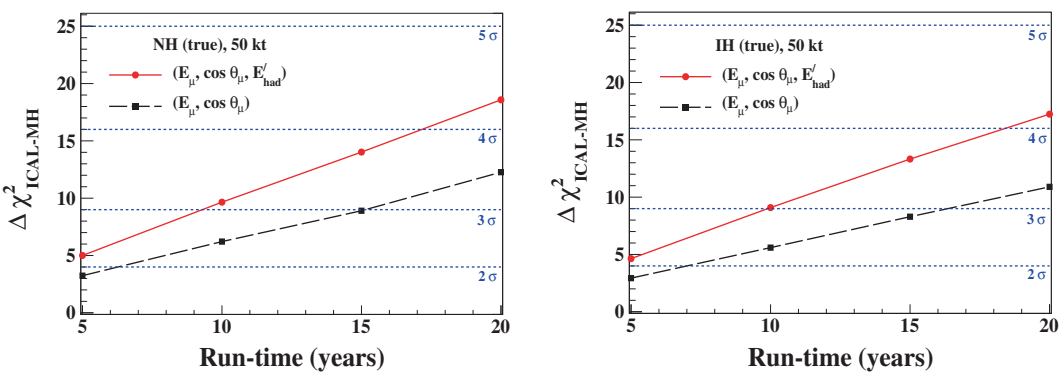

Figure 5.13. $\Delta\chi^2_{\text{ICAL-MH}}$ as a function of the exposure assuming NH (left panel) and IH (right panel) as the true hierarchy. The line labelled $(E_\mu, \cos\theta_\mu)$ denotes results without including hadron information, while the line labelled $(E_\mu, \cos\theta_\mu, E'_{\text{had}})$ denotes improved results after including hadron energy information [14]. Here we have taken $\sin^2 2\theta_{13}(\text{true}) = 0.1$ and $\sin^2\theta_{23}(\text{true}) = 0.5$.

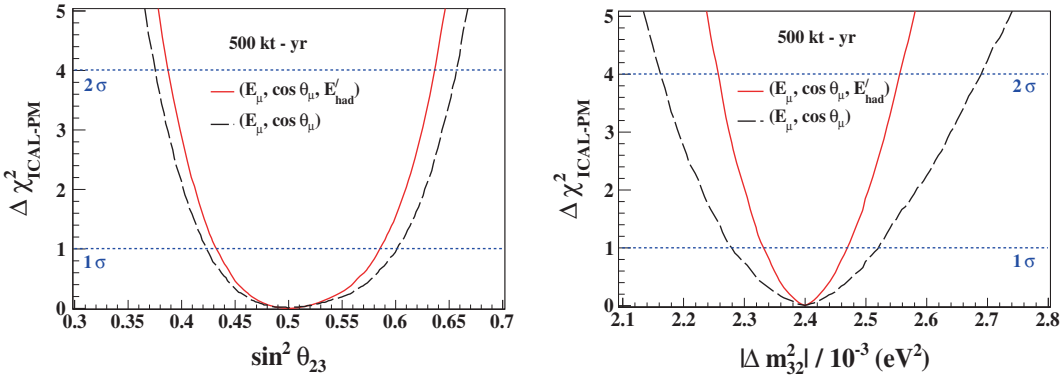

Figure 5.14. The left panel shows $\Delta\chi^2_{\text{ICAL-PM}}(\sin^2\theta_{23})$ and the right panel shows $\Delta\chi^2_{\text{ICAL-PM}}(|\Delta m^2_{32}|)$, assuming NH as true hierarchy. The lines labelled $(E_\mu, \cos\theta_\mu)$ denote results without including hadron information, while the lines labelled $(E_\mu, \cos\theta_\mu, E'_{\text{had}})$ denote improved results after including hadron energy information [14].

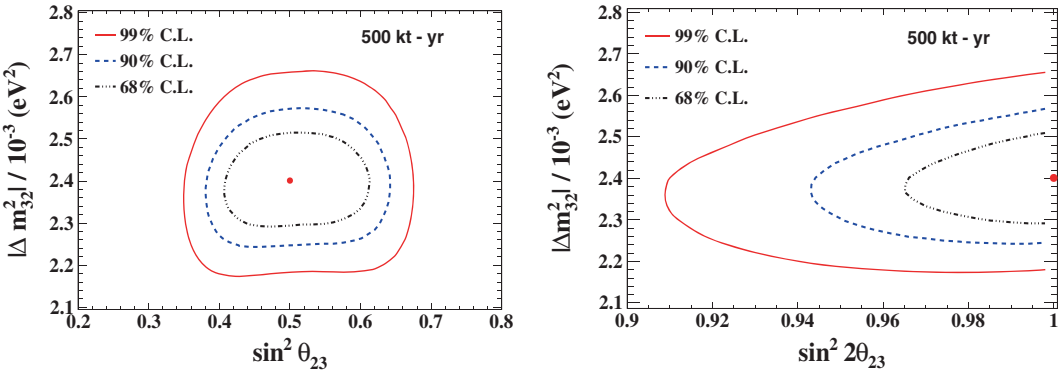

Figure 5.15. $\Delta\chi^2_{\text{ICAL-PM}}$ confidence level contours (2 dof) in the $\sin^2\theta_{23}$–$|\Delta m^2_{32}|$ plane (left panel) and in the $\sin^2 2\theta_{23}$–$|\Delta m^2_{32}|$ plane (right panel), using the hadron energy information, with NH as the true hierarchy. The true choices of the parameters have been marked with a dot [14].

the muon-only analysis with identical $(E_\mu, \cos\theta_\mu)$ binning, which gives precisions of 13.7 and 5.4%, respectively.

Figure 5.15 shows the $\Delta\chi^2_{\text{ICAL-PM}}$ contours in the $\sin^2\theta_{23}$–$|\Delta m^2_{32}|$ plane (left panel) and in the $\sin^2 2\theta_{23}$–$|\Delta m^2_{32}|$ plane (right panel), using the hadron energy information. Here the true value of θ_{23} has been taken to be maximal, and so the contours in the left panel are almost symmetric in $\sin^2\theta_{23}$.

Figure 5.16 shows the comparison of the projected 90% CL precision reach of ICAL (500 kt-yr) in $\sin^2\theta_{23}$–$|\Delta m^2_{32}|$ plane with other experiments [127–129]. Using hadron energy information, the ICAL will be able to achieve the $\sin^2\theta_{23}$ precision comparable to the current precision for Super-Kamiokande [127] or T2K [129], and the $|\Delta m^2_{32}|$ precision comparable to the MINOS reach [128]. Of course, some of these experiments would have collected much more statistics by the time ICAL would have an exposure of 500 kt-yr, and so the ICAL will therefore not be competing with these experiments for the precision measurements of these mixing parameters. However,

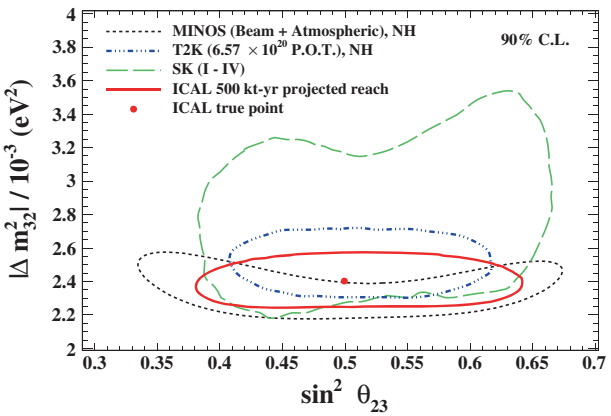

Figure 5.16. 90% CL contours in the $\sin^2\theta_{23}$–$|\Delta m^2_{32}|$ plane (2 dof): the current limits from Super-Kamiokande [127], MINOS [128], and T2K [129] have been shown along with the ICAL reach for the exposure of 500 kt-yr, assuming true NH. The true choices of the parameters for ICAL have been marked with a dot [14].

the ICAL measurements will serve as complementary information for the global fit of world neutrino data. Note that, as compared to the atmospheric neutrino

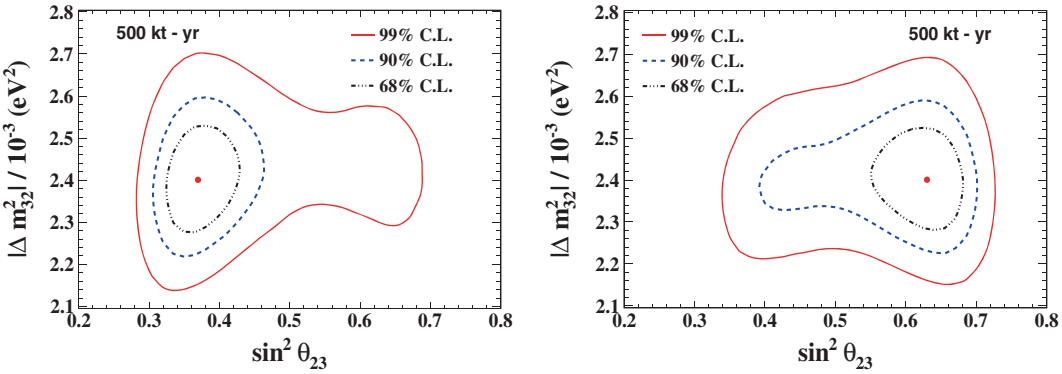

Figure 5.17. $\Delta\chi^2_{\text{ICAL-PM}}$ confidence level contours in the $\sin^2\theta_{23}$–$|\Delta m^2_{32}|$ plane, for $\sin^2\theta_{23}(\text{true}) = 0.37$ (left panel) and $\sin^2\theta_{23}(\text{true}) = 0.63$ (right panel), using the hadron energy information. Here the true hierarchy is NH [14].

analysis at Super-Kamiokande, the ICAL precision on $|\Delta m^2_{32}|$ is far superior. This is due to the better precision in the reconstruction of muon energy and direction at ICAL.

With a non-maximal true value of θ_{23}, the bounds on $\sin^2\theta_{23}$ range will be asymmetric about 0.5. Figure 5.17 shows the sensitivity of ICAL for $\sin^2 2\theta_{23} = 0.93$ (i.e. $\sin^2\theta_{23} = 0.37, 0.63$). It may be observed that for θ_{23} in the lower octant, the maximal mixing can be ruled out with 99% CL with 500 kt-yr of ICAL data. However, if θ_{23} is closer to the maximal mixing value, or in the higher octant, then the ICAL sensitivity to exclude maximal mixing would be much smaller.

5.8.4 *Non-maximal θ_{23} and its octant.* In analogy with the mass hierarchy discovery sensitivity, the statistical significance of the analysis to rule out the wrong octant is quantified as

$$\Delta\chi^2_{\text{ICAL-OS}} = \chi^2_{\text{ICAL}}(\text{false octant}) - \chi^2_{\text{ICAL}}(\text{true octant}). \tag{5.19}$$

Here, $\chi^2_{\text{ICAL}}(\text{true octant})$ and $\chi^2_{\text{ICAL}}(\text{false octant})$ are obtained by performing a fit to the 'observed' data assuming the true octant and wrong octant, respectively.

Figure 5.18 shows the sensitivity of ICAL to the identification of the θ_{23} octant, with and without including hadron energy information. It may be observed that a 2σ identification of the octant is possible with the 500 kt-yr INO data alone only when the true hierarchy is NH and the true octant is LO. In this case, without using the hadron energy information, one can get a 2σ identification only when $\sin^2\theta_{23}\,(\text{true}) < 0.365$, which is almost close to the present 3σ bound. With the addition of hadron energy information, this task is possible as long as $\sin^2\theta_{23}\,(\text{true}) < 0.395$. If the true octant is HO or the true mass hierarchy is inverted, then the discrimination of θ_{23} octant with the ICAL data alone becomes rather difficult. The reach is found not to be much sensitive to the exact value of θ_{13}. Clearly, the octant discrimination becomes more and more difficult as the true value of $\sin^2\theta_{23}$ goes close

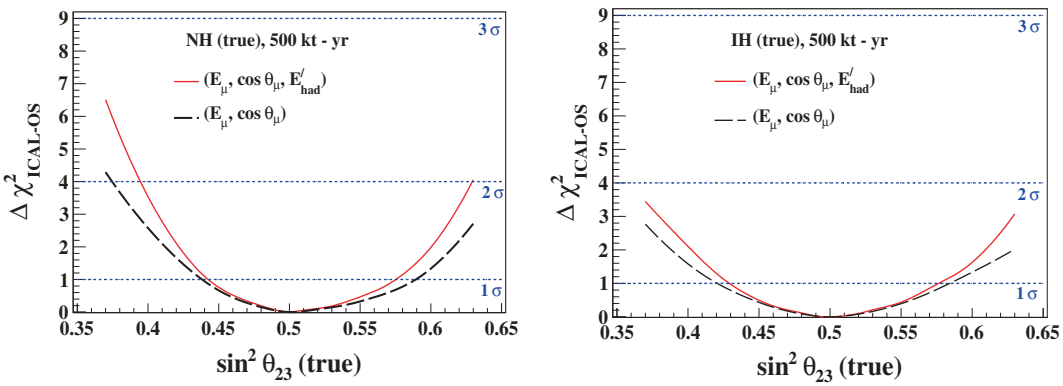

Figure 5.18. $\Delta\chi^2_{\text{ICAL-OS}}$ for octant discovery potential as a function of true $\sin^2\theta_{23}$. The left panel (right panel) assumes NH (IH) as true hierarchy. The line labelled $(E_\mu, \cos\theta_\mu)$ denotes results without including hadron information, while the line labelled $(E_\mu, \cos\theta_\mu, E'_{\text{had}})$ denotes improved results after including hadron energy information. ICAL exposure of 500 kt-yr is considered [14].

to the maximal mixing. A combination of atmospheric as well as long-baseline experiments is needed to make this measurement [130].

In conclusion, the inclusion of correlated hadronic information improves the sensitivity of ICAL to mass hierarchy, precision measurement of $|\Delta m^2_{32}|$ and θ_{23}, exclusion of maximal mixing, as well as θ_{23} octant determination. This analysis appears to be the optimal one to extract information from ICAL data. However, for the potential of this method to be realized, a very good understanding of the hadron response of the ICAL detector is crucial.

5.9 *ICAL physics potential: Highlights*

In summary, the ICAL detector is extremely suitable for determining the neutrino mass hierarchy, due to its capabilities of measurements of muon and hadron energies, and identification of the muon charge. The cleanest and the simplest analysis of the ICAL data uses the information on muons only. However, the reach of the detector improves tremendously if the information on hadron energy is also used additionally. Simply adding this energy to the muon energy to reconstruct the neutrino energy is, however, not enough, as it causes some dilution in the accurately known muon information. The information on the muon energy, muon direction, and hadron energy has to be kept separately and used in the analysis. Such an analysis indicates that in 10 years, a 50 kt ICAL can, by itself, distinguish between the normal and the inverted hierarchy with a significance of more than 3σ.

One important point to emphasize here is that this capability of ICAL is independent of the actual value of $\delta_{\rm CP}$. Hence, the results in this section are independent of $\delta_{\rm CP}$. Moreover, this feature may be exploited by combining the ICAL information with that from the other CP-sensitive experiments, to improve the mass hierarchy discrimination. Such synergies between ICAL and the other experiments will be explored in the next section.

6. Synergy with other experiments

The whole is greater than the sum of its parts.
– Aristotle

While ICAL has not yet started construction, long-baseline experiments like NOνA [68–70] and T2K [39] have already been taking data, and are in principle sensitive to the mass hierarchy. Apart from them, major atmospheric neutrino detectors like Hyper-Kamiokande (HK) [72], Precision IceCube Next Generation Upgrade (PINGU) [73] and Oscillation Research with Cosmic in the Abyss (ORCA) [131] are being planned. The medium-baseline reactor oscillation experiments JUNO [132] and RENO-50 [83] also will aim to determine the mass hierarchy by performing a very precise, high statistics measurement of the neutrino energy spectrum. In this section, we first comment on the individual sensitivities of these experiments, and later explore the synergy between them.

While NOνA and T2K get a large number of events due to intense neutrino beams created at Fermilab and J-PARC respectively, the neutrino-baseline distances available to them are rather small ($\approx$800 and 300 km, respectively), compared to those for atmospheric neutrinos, which can be as long as 10000 km. As a result, the matter effects experienced by the neutrinos during their propagation, which are crucial for the mass hierarchy identification, are small. In spite of this, the large input flux allows NOνA to be sensitive to mass hierarchy, at least with favourable values of $\delta_{\rm CP}$.

HK is a planned water Cherenkov detector with a fiducial volume of 500 kt, while PINGU is a megaton-size part of IceCube, where an increased density of the digital optical modules would bring down the threshold from 150 to 5 GeV so that atmospheric neutrinos may be detected. ORCA would be a deep sea neutrino telescope in the Mediterranean Sea. All these detectors can measure the energy and direction of muons as well as electrons (PINGU can also detect hadron showers through their cascade events). However, they do not have charge identification capabilities. The sensitivities of these atmospheric neutrino experiments will arise from their large sizes, which lead to a large number of events.

The reactor experiments JUNO and RENO50, with $\sim$50 km baseline, will approach the mass hierarchy measurement by using interference effects between the two oscillation frequencies [133,134]. Determination of mass hierarchy in such set-ups require a very good knowledge of the shape uncertainty of the reactor neutrino fluxes and the non-linearity of the detector response. In a detailed analysis by the JUNO Collaboration [82], it has been claimed that $\sim 3\sigma$ sensitivity to mass hierarchy including reasonable values of systematic uncertainties is possible in six years.

In figure 6.1, we compare the individual hierarchy sensitivities of NOνA, HK, and PINGU with the sensitivity of ICAL [135]. The figure is drawn following [18], wherein the median sensitivities of the experiments are shown when the true hierarchy is NH. The

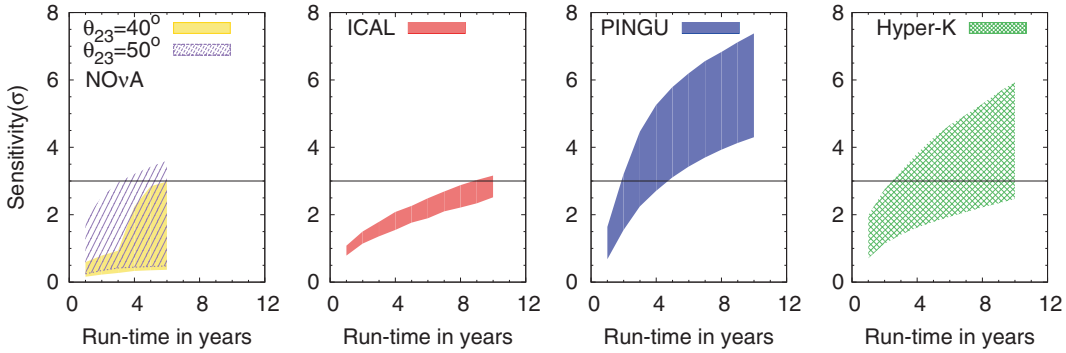

Figure 6.1. Projected hierarchy sensitivities of NOνA, ICAL, HK, and PINGU, if the true hierarchy is NH. It is to be noted that this figure is only indicative in nature; the actual sensitivities may get altered with changes in analysis techniques, systematics etc. While NOνA has already started taking data, the other experiments are yet to start.

NOνA results, obtained by using GLoBES [136,137], assume equal time runs for ν and $\bar{\nu}$ every year, with two θ_{23} values, 40° and 50°. The projected sensitivities of ICAL from [14], HK from [138] and PINGU from [73] are used in generating this plot. Note that the sensitivity for ICAL shown here is higher than that shown in [18] due to the improvement coming from the inclusion of hadronic information [14].

The width of the shaded/coloured regions for NOνA arises from the variation of $\delta_{\rm CP}$ in its full range, while for atmospheric neutrino experiments, which are insensitive to $\delta_{\rm CP}$, the width of the shaded region is due mainly to the variation of θ_{23}. (The θ_{23} ranges used are slightly different for different experiments, depending on what they use for their analyses. The range used is 38°–53° for ICAL, 40°–50° for HK, and 38.7°–51.3° for PINGU.) The lower end of the bands, indicating the worst sensitivity, corresponds to the lowest value of θ_{23}.

The figure demonstrates that after three years of ν and three years of $\bar{\nu}$ run at NOνA, which is the current plan, one may obtain a sensitivity anywhere between 0.5σ and 3.5σ, depending on the actual value of $\delta_{\rm CP}$. HK can attain a 3σ sensitivity to mass hierarchy in approximately five years for $\sin^2\theta_{23} = 0.5$ [72], while PINGU can reach the same sensitivity in three years for this scenario, if the cascade events can be included in the analysis [73]. The hierarchy sensitivity of PINGU and HK depends strongly on θ_{23}, growing very fast with increasing θ_{23} because of the corresponding increase in the number of events. ORCA (not shown in the figure) can achieve 3–5σ hierarchy sensitivity using the muon events for a 20 Mt-yr exposure [131]. ICAL is expected to take about 9–10 years to reach the 3σ sensitivity by itself. However, if true value of $\delta_{\rm CP}$ is in the unfavourable region for NOνA, then an early hint may be obtained from ICAL. Even later, for lower values of θ_{23}, the hierarchy sensitivity of ICAL can be greater than that of HK.

The relative importance of different experiments to the mass hierarchy determination thus depends crucially on what the value of $\delta_{\rm CP}$ is, and what the starting dates of the experiments are. However, note that ICAL is the only experiment among these that has a magnetic field and the resulting charge identification capability that can distinguish between neutrinos and antineutrinos. Among the atmospheric neutrino experiments, it will be the only experiment that can perform a neutrino and antineutrino analysis independently. Its importance in pinning down the mass hierarchy is thus expected to be crucial.

So far in this Review, the expected data from ICAL alone have been used. However, the reach of INO will be enhanced due to the information available from earlier experiments. A consistent way of taking the impact of these experiments into account is to include their data in a combined χ^2 fit. In this work, we present the impact of the prior data from these experiments on the ICAL physics reach, as well as how the ICAL data will help these experiments remove certain ambiguities from their analysis, and zero in on the actual neutrino mixing parameters.

6.1 *Combined mass hierarchy reach at* $\delta_{\rm CP} = 0$ *for ICAL + T2K + NOνA*

As we have seen in §5, the 50 kt ICAL by itself can identify the mass hierarchy with a significance of $\Delta\chi^2 \approx 9$ with 10 years of running. This reach is independent of the actual value of the CP-violating phase $\delta_{\rm CP}$. Currently running fixed-baseline experiments like T2K and NOνA would already have obtained some sensitivity to the mass hierarchy during their run. This sensitivity will depend on the actual value of $\delta_{\rm CP}$, as we

shall see in §6.2. In this section, we shall see the effect of using the information from these experiments, in the case where the value of δ_{CP} is taken to be zero. Note that the contribution of the current reactor experiments to the mass hierarchy measurements is negligible [11].

A preliminary estimate of the combined sensitivity to the neutrino mass hierarchy as a function of the number of years of run of the ICAL atmospheric neutrino experiment is shown in figure 6.2 [17]. For each set of oscillation parameters, the joint χ^2 from all experiments is given by

$$\chi^2 = \chi^2_- + \chi^2_+ + \sum_i \chi^2_i + \chi^2_{\text{prior}}, \tag{6.1}$$

where χ^2_-, χ^2_+ are as defined in eqs (5.13) and (5.14), $\sum_i \chi^2_i$ is the contribution from the accelerator experiments (i runs over T2K and NOνA), and χ^2_{prior} is the prior on θ_{13} from the reactor experiments. Here a prior of 4.5% on $\sin^2 2\theta_{13}$ has been taken, which matches the outcome of the recent global fit [53]. This joint χ^2 is computed and marginalized over all oscillation parameters, to determine the minimized joint $\Delta\chi^2$ shown in the figure. Note that the x-axis in this figure shows the number of years of running of ICAL only. We assume a complete T2K run (total luminosity 8×10^{21} protons on target) with neutrinos only, three years of NOνA run with neutrinos, and three years of NOνA run with antineutrinos have already been completed. We use the standard set-up of these experiments as in the GLoBES package [136,137].

The figure shows that the prior information from T2K and NOνA implies that the target of $\Delta\chi^2 = 9$ significance for the hierarchy identification may now be achieved within six years of the ICAL running, as opposed to about ten years with only the ICAL data. Note that this is not just the effect of $\Delta\chi^2$ provided by the fixed-baseline experiments. These experiments also yield an improved precision in θ_{23}, $|\Delta m^2_{\text{eff}}|$ (through their disappearance channel), and in θ_{13} (through their appearance channel). As a result, the impact of marginalization over these parameters in the ICAL analysis is greatly reduced. Indeed, for 500 kt-yr of ICAL data, the contribution of $\Delta\chi^2_{\text{ICAL-MH}}$ to total $\Delta\chi^2$ in the case of true normal hierarchy increases from 9.5 (without the data from T2K and NOνA) to 10.4 (with the data from T2K and NOνA). Note that the contributions of T2K and NOνA themselves are expected to be $\Delta\chi^2 \approx 0.12$ and 2.6, respectively.

The fact that total $\Delta\chi^2$ in the ICAL, T2K, and NOνA experiments is greater than the sum of their individual $\Delta\chi^2$ values is the synergy among these experiments. Though ICAL is the dominant contributor to the hierarchy sensitivity in this case, it clearly benefits tremendously from this synergy. Similarly, for other physics issues like the precision measurements of mixing parameters, the combination of data from long-baseline experiments and ICAL will help improve our overall understanding of these parameters. Here, the long-baseline experiments are expected to play dominant roles because they are directly sensitive to θ_{23} and $|\Delta m^2_{\text{eff}}|$ through their disappearance channel, while ICAL is expected to play a complementary role.

So far we have discussed the case of $\delta_{CP} = 0$. In the next section, we shall explore the case of non-vanishing δ_{CP} in detail because it affects the mass hierarchy sensitivity of fixed-baseline experiments.

6.2 *Ensuring mass hierarchy sensitivity for all* δ_{CP}

As seen in §5.6, the insensitivity of ICAL to the actual value of δ_{CP} comes from the fact that the muon

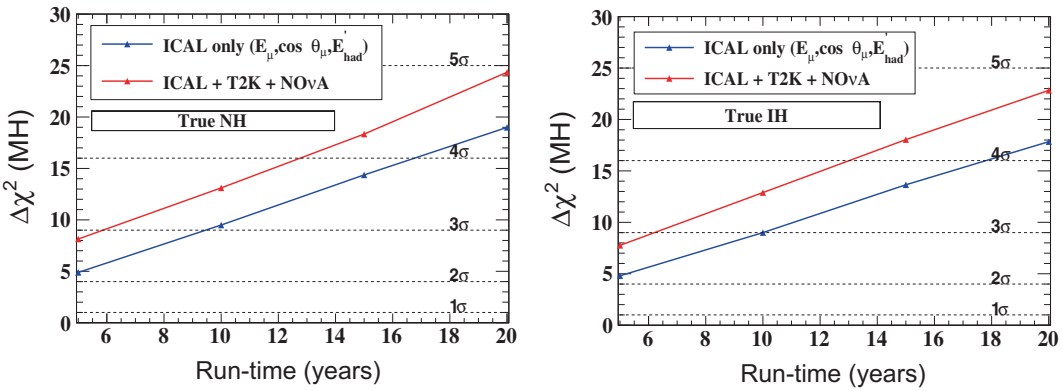

Figure 6.2. Preliminary results on $\Delta\chi^2$ for the wrong hierarchy obtained from a combined analysis of T2K (a luminosity of 8×10^{21} protons on target in neutrino run), NOνA (three-year neutrino and three-year antineutrino runs), and ICAL [17]. The left (right) panel is for true normal (inverted) hierarchy. We take $\sin^2 2\theta_{13}(\text{true}) = 0.1$, $\sin^2 \theta_{23}(\text{true}) = 0.5$, and $\delta_{CP} = 0$, and all parameters are allowed to vary over their 3σ ranges as shown in table 1.1.

neutrinos at ICAL come dominantly from the original unoscillated muon neutrinos, while the muon neutrinos coming from the oscillated electron neutrinos play a subdominant role. The survival probability $P_{\mu\mu}$ (see Appendix B) is therefore more relevant than the conversion probability $P_{e\mu}$. In $P_{\mu\mu}$, the CP-violating phase $\delta_{\rm CP}$ appears as a subdominant oscillating term, whose oscillations, moreover, are averaged out due to the uncertainties in the energies and directions of the incoming neutrinos [19].

On the other hand, the fixed-baseline experiments like T2K or NOνA are sensitive to the conversion probability $P_{\mu e}$, whose dominant term depends on $\delta_{\rm CP}$. Moreover, though this term is oscillating, these experiments have a better knowledge of the neutrino energies, and the neutrino directions are very precisely known. As a result, the data at these experiments are highly sensitive to $\delta_{\rm CP}$. In particular, while performing the fit to the data, the value of $\delta_{\rm CP}$ can be adjusted, along with the value of $|\Delta m^2_{31}|$, to compensate for the wrong hierarchy in half the $\delta_{\rm CP}$ parameter space. As a result, even if the wrong hierarchy is being fitted, a good fit may be obtained, albeit at a wrong value of $\delta_{\rm CP}$. As the actual $\delta_{\rm CP}$ value is unknown, this worsens the hierarchy sensitivity of the experiment. This may be seen from the left panel of figure 6.3, where the actual $\delta_{\rm CP}$ is taken to be vanishing. However, NOνA gives a better fit at another value of $\delta_{\rm CP}$, with a very reduced value of $\delta_{\rm CP}$ as compared to that at the true $\delta_{\rm CP}$ value. In the absence of any knowledge about the actual $\delta_{\rm CP}$ value, this results in a reduced performance of the detector.

The right panel of figure 6.3 shows $\Delta\chi^2$ for the mass hierarchy sensitivity as a function of $\delta_{\rm CP}$(true). The data are generated for normal hierarchy at each value of $\delta_{\rm CP}$(true) shown on the x-axis, and a fit is performed for inverted hierarchy by marginalizing over *all* oscillation parameters, including $\delta_{\rm CP}$. Clearly, the reach of NOνA alone for determining the neutrino mass hierarchy is extremely sensitive to the actual value of $\delta_{\rm CP}$. While the sensitivity is $\Delta\chi^2 \approx 9$ for $\delta_{\rm CP}$(true) near 270°, it falls to almost zero for $\delta_{\rm CP}$(true) $\simeq$ [50°–150°].

When T2K and all reactor data are added, there is some improvement to the combined sensitivity. In particular, in the $\delta_{\rm CP}$(true) $\simeq$ [50°–150°] range where NOνA by itself gives no mass hierarchy sensitivity, the addition of T2K and reactor data takes $\Delta\chi^2$ to $\simeq$3.5. The reason for this is the mismatch between the best-fits for different experiments. For the same reason, even the reactor data that are not sensitive to $\delta_{\rm CP}$ but only to $|\Delta m^2_{31}|$ help, albeit marginally, in disfavouring the spurious best-fit minima for the wrong hierarchy, as they do not allow the fit value of $|\Delta m^2_{31}|$ to stray far from the actual one. A combined fit with all accelerator and reactor data thus gives a best-fit at a point ($\delta_{\rm CP} = 198°$, $\sin^2\theta_{23} = 0.48$ and $\sin^2 2\theta_{13} = 0.1$) where the tension between these experiments gives a small hierarchy sensitivity even in the disfavoured $\delta_{\rm CP}$(true) range ([0°–180°] for normal hierarchy).

Finally, addition of the ICAL data raises $\Delta\chi^2$ by a constant amount for all values of $\delta_{\rm CP}$(true), and ensures the identification of hierarchy to more than $\Delta\chi^2 \approx 10$ for even those $\delta_{\rm CP}$(true) values for which other experiments cannot rule out wrong hierarchy by themselves. In the best-case scenario, the hierarchy may be identified to $\Delta\chi^2 \approx 20$.

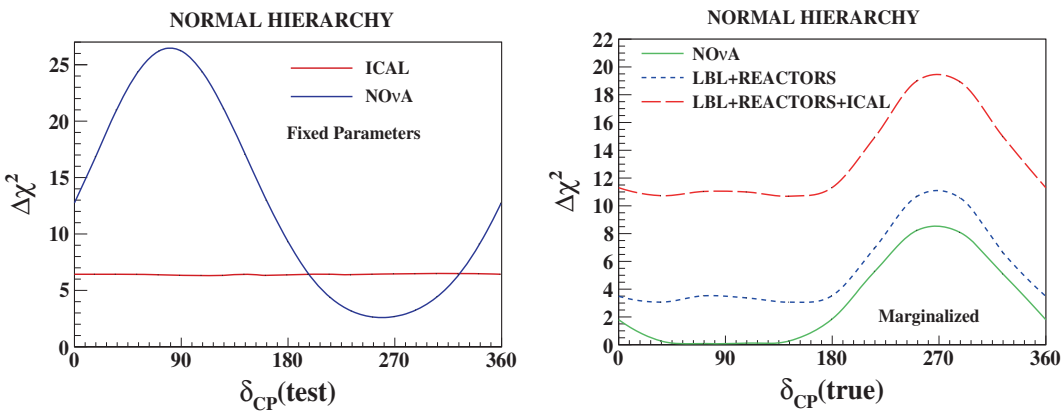

Figure 6.3. The left panel shows $\Delta\chi^2$ for mass hierarchy sensitivity at NOνA and ICAL, when the actual value of $\delta_{\rm CP}$ is vanishing, and different test values of $\delta_{\rm CP}$ (shown along the x-axis) are taken. The right panel shows the dependence of mass hierarchy sensitivities of experiments (or their combinations) to the actual $\delta_{\rm CP}$, when the test $\delta_{\rm CP}$ is varied over all its range for minimizing $\Delta\chi^2$. The full proposed runs of the long-baseline and reactor experiments are taken. The ICAL exposure is taken to be 500 kt-yr, and only the muon energy and direction are used, ignoring the hadron information [11].

Note that the ICAL results in the figure have been obtained by using only the information on muon energy and momentum. If the hadron information is also added, the combined $\Delta\chi^2$ of all the experiments is expected to be 12–22, depending on whether the actual δ_{CP} value is favourable to the fixed-baseline experiments or not.

6.3 *Octant of θ_{23} from the ICAL, NOνA, and T2K data*

Combined analysis of all the neutrino oscillation data available disfavours the maximal mixing solution for θ_{23} at 1.4σ confidence level [54,57] which is mostly driven by the MINOS accelerator data in ν_μ and $\bar{\nu}_\mu$ disappearance modes [60]. Now, if $\sin^2 2\theta_{23}$ turns out to be different from unity as suggested by the recent oscillation data, this creates the problem of octant degeneracy of θ_{23} [61]. In a recent global fit work by Capozzi *et al* [58], the authors have found an overall preference for the first or lower octant (LO) at 95% confidence level assuming normal hierarchy. In the case of inverted hierarchy, the higher octant (HO) seems to be preferred [54].

In this section, we present the preliminary results showing the discovery reach of the octant of θ_{23} with atmospheric neutrinos at ICAL in combination with the projected T2K [139,140] and NOνA [68–70] data. We have performed the analysis for ICAL by using only the information on muon energy and muon direction which has been described in detail in §5.2. The Earth matter effect in the $P_{\mu\mu}$ channel can be very useful to resolve the octant ambiguity of θ_{23} [124].

The potential of the experiments for excluding the wrong octant as a function of true value of $\sin^2\theta_{23}$ is shown in figure 6.4. For each given value of θ_{23}(true), we marginalize over all the allowed values of θ_{23} in the opposite octant, including the maximal mixing value. We take 5% prior on $\sin^2 2\theta_{13}$ with a true value of 0.1, and take $|\Delta m^2_{\text{eff}}|$(true) $= 2.4 \times 10^{-3}$ eV^2. No priors have been taken on atmospheric parameters. In the case of T2K and NOνA, we generate the data with $\delta_{CP} = 0°$, but while performing the fit, we marginalize over the entire range of δ_{CP} between 0 and 2π. For ICAL, we take $\delta_{CP} = 0°$ both in data and in the fit as ICAL atmospheric analysis is not sensitive to δ_{CP}.

From figure 6.4, we can see that 50 kt ICAL in ten years can identify the correct octant at 2σ if $\sin^2\theta_{23}$ (true) $< 0.38(0.35)$ only when the true hierarchy is normal(inverted) and the true octant is LO. The green dotted line depicts the combined sensitivity of T2K (2.5 years of ν run + 2.5 years of $\bar{\nu}$ run) and NOνA (3 years of ν run + 3 years of $\bar{\nu}$ run). The red dashed line presents the combined results of ICAL, T2K, and NOνA.

The projected data from T2K and NOνA will clearly play a crucial role in addressing the issue of θ_{23} octant. Adding the information from these long-baseline experiments, we can improve the octant discovery reach of ICAL significantly, suggesting the possible synergy between the atmospheric and long-baseline data. While the contribution of ICAL itself is marginal, the combined atmospheric and long-baseline data can establish the correct octant at 3σ if $\sin^2\theta_{23}$(true) $<$ 0.42(0.43) assuming normal(inverted) hierarchy and the lower octant is chosen by nature.

6.4 *ICAL data for improving CPV discovery potential of T2K and NOνA*

The identification of mass hierarchy and measurement of CP violation are intrinsically interconnected at the

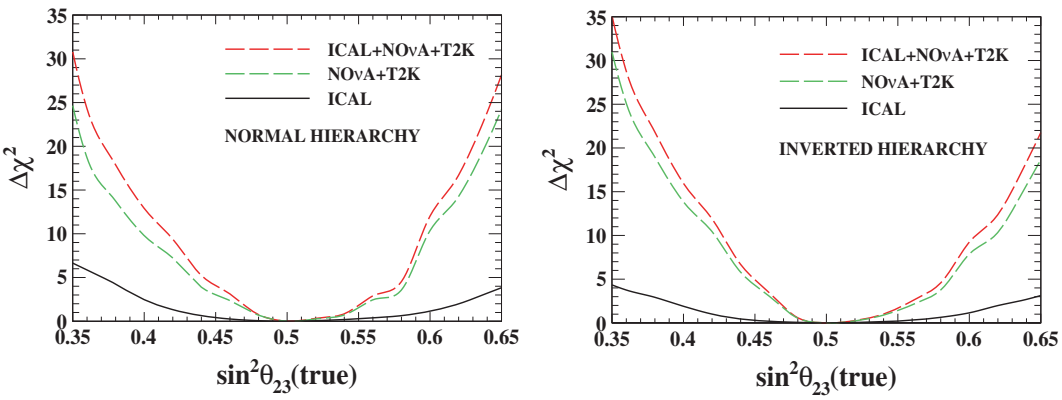

Figure 6.4. $\Delta\chi^2_{\text{ICAL-OS}}$ for octant discovery potential as a function of true $\sin^2\theta_{23}$. The left (right) panel assumes normal (inverted) hierarchy as the true choice. In each panel, the black solid line shows the performance of ICAL with an exposure of 500 kt-yr using only the information on muon energy and muon direction. The green dotted line depicts the combined sensitivity of T2K (integrated luminosity of 4×10^{21} protons on target in neutrinos and 4×10^{21} protons on target in antineutrinos) and NOνA (three years of ν run + three years of $\bar{\nu}$ run). The red dashed line presents the combined results of ICAL, T2K, and NOνA.

fixed-baseline experiments, due to the leading term in the relevant conversion probability $P_{\mu e}$ as given in Appendix B. Therefore, in the absence of knowledge about hierarchy, it is possible that the wrong hierarchy conspiring with an incorrect value of δ_{CP} may mimic the correct combination of hierarchy and δ_{CP}. As a result, in the unfavourable range of δ_{CP} as described in §6.2, i.e. $\delta_{CP} \in [0°, 180°]$ if the actual hierarchy is normal (NH) and $\delta_{CP} \in [180°, 360°]$ if the actual hierarchy is inverted, the ability of NOνA and T2K to measure δ_{CP}, in particular to discover non-zero δ_{CP} and hence CP violation, is severely curtailed. The hierarchy sensitivity of an atmospheric neutrino experiment like ICAL, which is independent of the actual δ_{CP} value, can restore the ability of these fixed-baseline experiments to discover CP violation [19,88].

The ICAL analysis is performed using only the information on muon energy and direction, neglecting hadronic information, and taking an exposure of 500 kt-yr. The input parameter ranges and marginalization ranges as given in table 1.1 are used, with the prior of 5% taken on θ_{13}. The discovery potential for CPV is quantified by considering a variation of δ_{CP} over the full range [0°, 360°] in the simulated data, and comparing it with $\delta_{CP} = 0°$ or 180° in the theory expectation. The definition of χ^2 used is the same as in §5.2.

In figure 6.5, we plot the CPV discovery potential of T2K and NOνA with and without information from ICAL. For T2K and NOνA, the same specifications as in §6.1 have been used. The figure shows that, as expected, the CP-violation sensitivity of the experiments is zero for true $\delta_{CP} = 0$ and π, while it is close to maximum at the maximally CP-violating values $\delta_{CP} = 90°$ or $\delta_{CP} = 270°$, depending on the hierarchy. The CPV discovery with NOνA and T2K suffers a drop in one of the half-planes of δ_{CP}, depending on the true hierarchy – in the region [0°, 180°] if it is NH and [180°, 360°] if it is IH.

The figure also shows that the additional information from ICAL will increase the sensitivities of these experiments in the unfavourable δ_{CP} half-plane. This corresponds to an almost two-fold increase in the range of δ_{CP} values for which CP violation can be discovered by the fixed-baseline experiments, and it happens because the hierarchy sensitivity of ICAL excludes the wrong-hierarchy minimum for the CPV discovery at 2σ. Thus, it is quite possible that, though an atmospheric neutrino experiment like ICAL is not sensitive

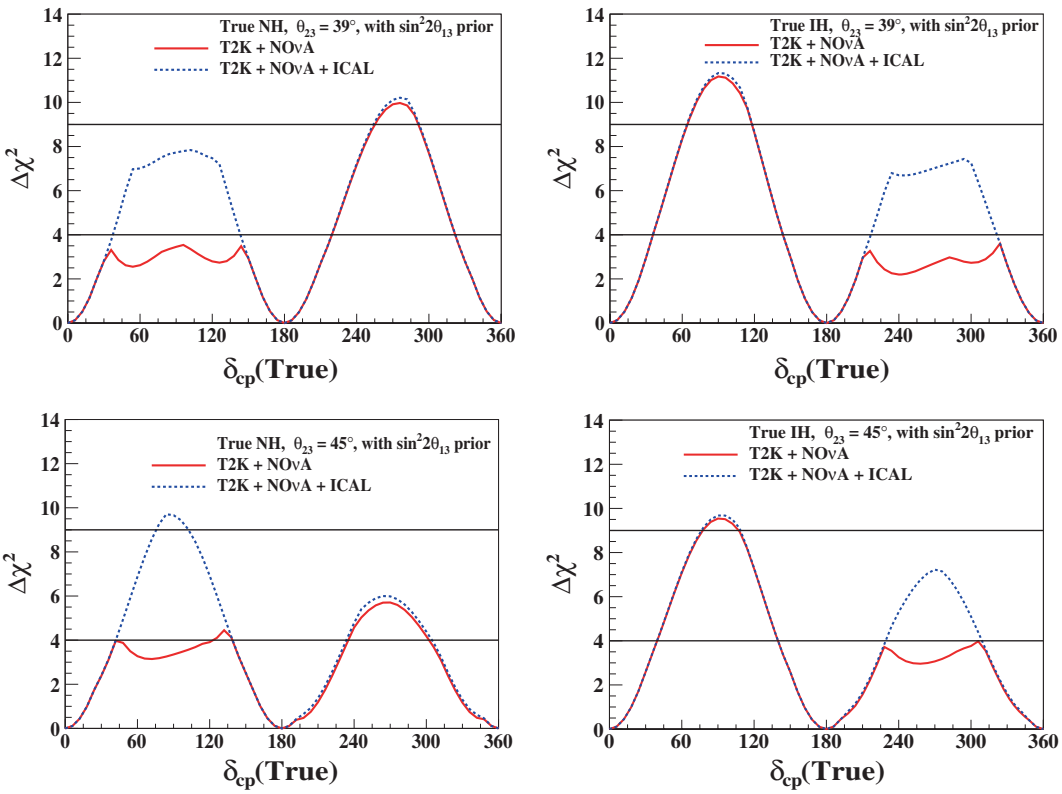

Figure 6.5. CPV discovery vs. true δ_{CP} for NOνA + T2K and NOνA + T2K + ICAL, for θ_{23}(true) = 39° (upper row) and 45° (lower row). The left and right panels correspond to normal and inverted true hierarchies, respectively. We use $\sin^2 2\theta_{13} = 0.1$, a prior of $\sigma_{\theta_{13}} = 0.005$, and a 500 kt-yr exposure for the ICAL.

to the CP phase, the first signature of CP violation may well come by the addition of ICAL data to those of these fixed-baseline experiments, possibly even a few years after these experiments have completed their runs [19,88].

The sensitivities of the fixed-baseline experiments to CPV discovery, and the relative improvement due to the addition of ICAL, have a clear dependence on θ_{23}, which may be discerned from figure 6.5, where we compare the results with $\theta_{23} = 39°$ and $\theta_{23} = 45°$. In the favourable δ_{CP} region, the CPV discovery potential worsens with increasing θ_{23}. This is because the δ_{CP}-independent leading term in eq. (B.9) increases with θ_{23}, giving a higher statistical error, while the CP-dependent term has only a weak dependence on this parameter [86]. In the unfavourable region, on the other hand, the CPV discovery potential improves with increasing θ_{23}. This happens because here the minimum of χ^2 from the long-baseline experiments comes with the wrong hierarchy, and the atmospheric neutrino data are needed to bring it to the correct hierarchy. The hierarchy identification capability of atmospheric neutrino data increases for larger θ_{23}, and hence the improvement in CPV discovery potential with higher θ_{23}, as can be seen in figure 6.5. For $\theta_{23} \gtrsim 50°$, the ICAL information is nearly superfluous, because the hierarchy sensitivity of the T2K and NOνA combination itself is good enough to exclude the wrong hierarchy CPV discovery minimum even for unfavourable δ_{CP} values.

In this section, we have shown that for unfavourable values of δ_{CP}, atmospheric neutrino data from ICAL considerably improves the CPV discovery potential of T2K and NOνA, and can lead to a significant CPV discovery using existing and upcoming facilities for a large fraction ($\gtrsim$50%) of δ_{CP} values. Adding ICAL muon data to T2K and NOνA results in an enhanced CPV discovery potential at 2σ for almost twice the range of δ_{CP} values compared to the fixed-baseline experiments alone. For maximal CPV the significance of the signal can reach 3σ in the unfavourable half-plane also. Indeed, if nature has chosen such unfavourable combinations of parameters then the addition of ICAL to T2K+NOνA may give us the first signal of leptonic CP violation.

7. Exploring new physics at ICAL

The end of all our exploring will be to arrive where we started. And know the place for the first time.
– T S Eliot

In addition to determining the parameters describing neutrino masses and mixing, the neutrino detection at ICAL may be used for probing various sources of new physics that can affect neutrino oscillations. Moreover, while ICAL is primarily designed for detecting muons and hadrons produced from neutrino interactions, it can also be sensitive to more exotic particles like magnetic monopoles or dark matter particles passing through the detector. In this section, we briefly discuss a few such ideas.

7.1 *Probing Lorentz and CPT violation*

Invariance under the product of charge conjugation (C), parity (P), and time reversal (T), i.e., the CPT theorem [141,142], is an essential feature of quantum field theories that underlie particle physics. This is a consequence of the invariance of the Lagrangian under proper Lorentz transformations. However, in a Standard Model extended (SME) Lagrangian that does not respect the Lorentz transformation symmetry, the CPT violation (CPTV) may be manifest [143,144], which may be measurable at the neutrino oscillation experiments. Some bounds on the CPTV parameters have already been obtained, using the atmospheric neutrino data from Super-Kamiokande [145]. The ultra-high energy neutrino data are expected to be especially sensitive to CPTV; for instance, see [146]. If the effects of CPTV are not observed, one may obtain limits on CPT and Lorentz-violating parameters.

7.1.1 *CPTV effects at the probability level.* Lorentz violation may be introduced in the effective Lagrangian for a single fermion field as [147]

$$\mathcal{L} = i\bar{\psi}\partial_\mu\gamma^\mu\psi - m\bar{\psi}\psi - A_\mu\bar{\psi}\gamma^\mu\psi - B_\mu\bar{\psi}\gamma_5\gamma^\mu\psi, \tag{7.1}$$

where A_μ and B_μ are constant 4-vectors. The terms containing A_μ and B_μ may be induced by new physics at higher energies, for instance. Since A_μ and B_μ are invariant under boosts and rotations, they explicitly give rise to Lorentz violation, which in turn leads to CPTV [148]. (CPT violation may also occur if particle and antiparticle masses are different. Such violation, however, also breaks the locality assumption of quantum field theories [148]. This mode of CPTV is not considered here.) The effective CPTV contribution to the neutrino Lagrangian can then be parametrized [149] as

$$\mathcal{L}_\nu^{\text{CPTV}} = \bar{\nu}_L^\alpha\, b_\mu^{\alpha\beta}\, \gamma^\mu\, \nu_L^\beta, \tag{7.2}$$

where $b_\mu^{\alpha\beta}$ are four Hermitian 3×3 matrices corresponding to the four Dirac indices μ, while α, β are

flavour indices. The effective Hamiltonian in vacuum for ultrarelativistic neutrinos with definite momentum p then becomes

$$H \equiv \frac{MM^\dagger}{2p} + b, \tag{7.3}$$

where M is the neutrino mass matrix in the CPT-conserving limit and b is the CPT-violating term.

For atmospheric neutrinos that may pass through appreciable amounts of matter before reaching the detector, the effective Hamiltonian in the flavour basis, that takes the matter effects and CPTV effects into account, may be written as

$$H_f = \frac{1}{2E} \cdot U_0 \cdot D(0, \Delta m^2_{21}, \Delta m^2_{31}) \cdot U_0^\dagger + U_b \cdot D_b(0, \delta b_{21}, \delta b_{31}) \cdot U_b^\dagger + D_m(V_e, 0, 0), \tag{7.4}$$

where U_0 and U_b are unitary matrices that diagonalize the $MM^\dagger$ and b matrices, respectively, while D, D_m and D_b are diagonal matrices with their elements as listed in brackets. Here, $V_e = \sqrt{2} G_F N_e$ with the electron number density N_e, and $\delta b_{i1} \equiv b_i - b_1$ for $i = 2, 3$, with b_1, b_2 and b_3 the eigenvalues of b.

As in the standard convention, U_0 is parametrized by three mixing angles $(\theta_{12}, \theta_{23}, \theta_{13})$ and one phase $\delta_{\rm CP}$. The matrix U_b is parametrized by three mixing angles $(\theta_{b12}, \theta_{b23}, \theta_{b13})$ and six phases. Thus, H_f contains six mixing angles $(\theta_{12}, \theta_{23}, \theta_{13}, \theta_{b12}, \theta_{b23}, \theta_{b13})$ and seven phases.

The results will clearly depend on the mixing angles in the CPTV sector. In this section, we examine the effects of three different representative sets of mixing angles: (1) small mixing: $(\theta_{b12} = 6°, \theta_{b23} = 9°, \theta_{b13} = 3°)$, (2) large mixing: $(\theta_{b12} = 38°, \theta_{b23} = 45°, \theta_{b13} = 30°)$ and (3) identical to the mixing angles in the PMNS matrix: $(\theta_{b12} = \theta_{12}, \theta_{b23} = \theta_{23}, \theta_{b13} = \theta_{13})$. For simplicity, all seven phases have been taken to be zero, and the neutrino oscillation parameters as given in table 1.1 are used. It is observed that in the probability expressions, δb_{21} always appears with the smaller (by a factor of 30) mass squared difference Δm^2_{21}. Thus, its effects on oscillations are subdominant, limiting the capability of atmospheric neutrinos to constrain it, so that no useful constraints on δb_{21} seem to be possible.

For illustration, the oscillograms for the difference of the survival probability of ν_μ with and without CPTV for $\delta b_{31} = 3 \times 10^{-23}$ GeV are shown in figure 7.1. Several general features may be observed. First, the CPTV effects are larger at larger baselines for all energies. This is as expected from the results of the two-flavour analysis [96], which showed that the survival probability difference in vacuum is proportional to $\sin(\Delta m^2 L/2E) \sin(\delta b L)$. Secondly, as is well-known, matter effects are large and resonant for neutrinos with NH, and for antineutrinos with IH. Thus, in both these cases, they mask the (smaller) effect of CPTV stemming from U_b. Hence, for neutrino events, the CPTV sensitivity is significantly higher if the hierarchy is inverted as opposed to normal, and the converse is true for antineutrino events. Finally, the CPTV effects are largest for Cases 2 and 3, as compared to Case 1. This is due to the fact that mixing in Case 1 is very small compared to the other two. The origin of the difference for Cases 2 and 3 may be due to the fact that CPT violating effects are smaller when θ_{b13} is large [15].

7.1.2 *Simulation procedure and results.* The oscillation probabilities are calculated with the true values of oscillation parameters corresponding to table 1.1 and assuming no CPTV. The re-weighting algorithm [11] has been used to generate oscillated events. The energy resolutions, efficiencies, and charge misidentification errors are taken into account. Oscillated muon events are binned as a function of muon energy (10 bins) and muon zenith angle (40 bins). These binned data are folded with detector efficiencies and resolution functions. These data (labelled as $N^{\rm ex}$) are then fitted with another set of data (labelled as $N^{\rm th}$), where CPTV is allowed. The statistical significance of the difference between these two sets of data is calculated, using the pull method to include systematic errors as in the analyses in §5. χ^2 is calculated separately for the μ^+ and μ^- events and then added, to exploit the charge identification capability of ICAL. Marginalization has been carried out with respect to the neutrino oscillation parameters Δm^2_{31}, θ_{23}, θ_{13}, which are varied over their 3σ allowed ranges. The CP-violating phase $\delta_{\rm CP}$ is varied over its whole range, while δb_{21} is marginalized over the range 0 to 5×10^{-23} GeV.

Figure 7.2 illustrates the results of the analysis. It is observed that the best bounds on δb_{31} are obtained for both hierarchies in Case 3, where mixing in the CPTV sector is the same as the neutrino mixing. Good bounds are also obtainable if the mixing in the CPTV sector is large, as in Case 2. While the analysis for all mixing angles of U_b has not been carried out, these results indicate that, as long as the mixing angles are not too small, limits on δb_{31} of the order of 4×10^{-23} GeV will be possible at 99% CL. It should be noted that the above analysis assumes the mass hierarchy to be known. Indeed, if the marginalization over the

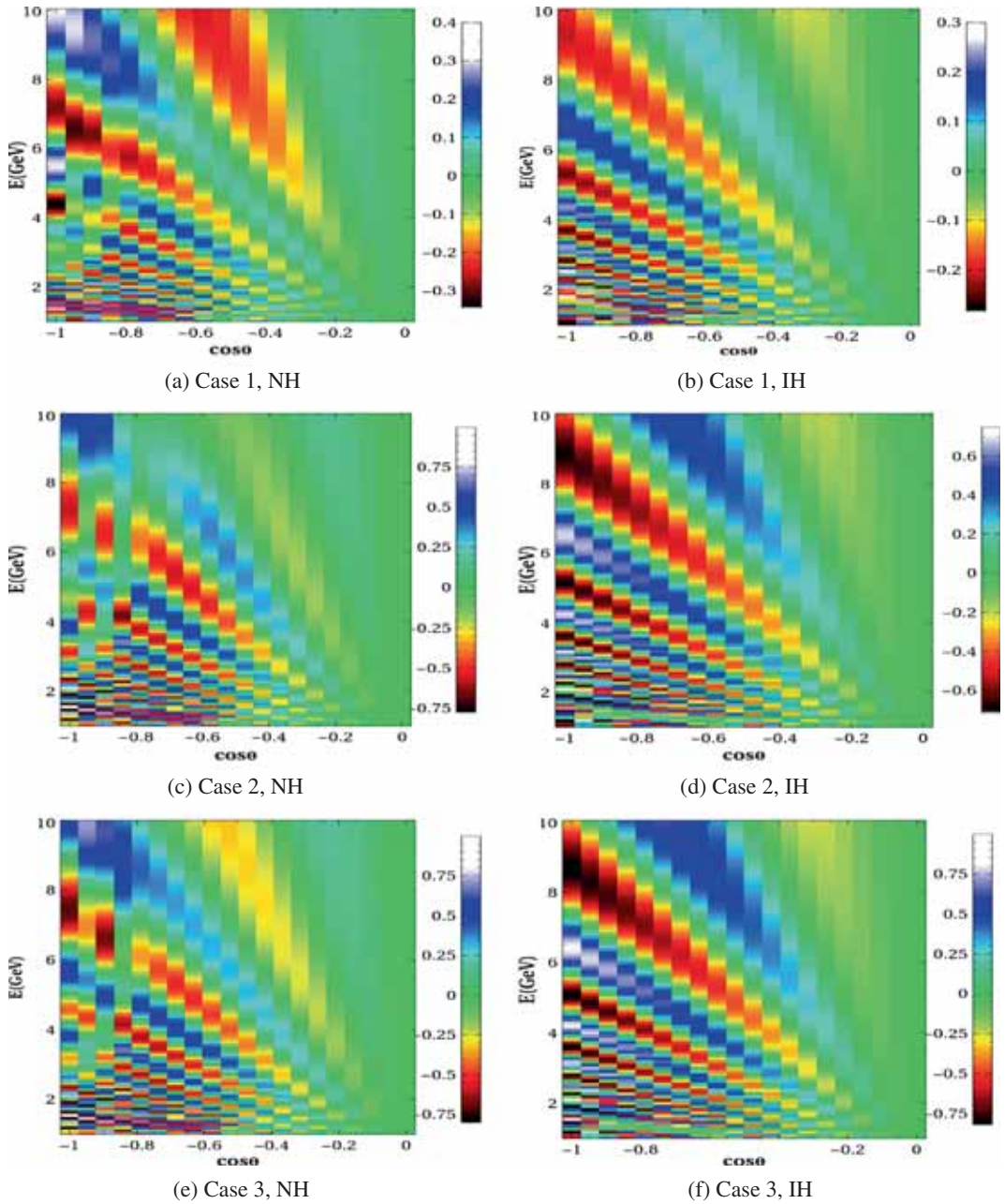

(a) Case 1, NH (b) Case 1, IH

(c) Case 2, NH (d) Case 2, IH

(e) Case 3, NH (f) Case 3, IH

Figure 7.1. The oscillograms of $\Delta P = (P^{U_b \neq 0}_{\nu_\mu \nu_\mu} - P^{U_b=0}_{\nu_\mu \nu_\mu})$ for three different mixing cases as described in the text. The left and right panels are for normal and inverted hierarchy, respectively. The value of $\delta b_{31} = 3 \times 10^{-23}$ GeV has been taken for illustration [15].

hierarchy is carried out, the results are considerably weaker.

Note that this study pertains to the type of CPTV that may be parametrized by eq. (7.1), which stems from explicit Lorentz violation, and the analysis is restricted to the muon detection channel. The CPTV that gives rise to differing masses for particles and antiparticles has not been considered. Given the smaller statistics and flux uncertainties that typify atmospheric data, it would be difficult to obtain good sensitivities to this type of CPTV, which breaks the locality assumption of quantum field theories. Finally, we note that in order to obtain good sensitivity to CPTV, knowing the hierarchy will be an important asset. This will anyway be the focus of many other analyses at ICAL.

7.2 *Search for magnetic monopoles*

The possible existence of magnetic monopoles (MM) is predicted by unification theories. These monopoles

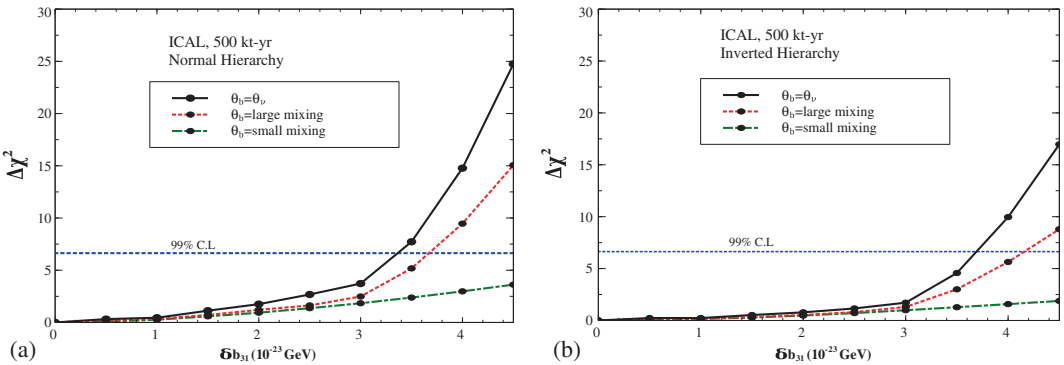

Figure 7.2. The bounds on δb_{31} for different cases for the mixing angles θ_b. The results are marginalized over θ_{23}, θ_{13}, $\delta_{\rm CP}$, Δm^2_{31}, and δb_{21}. Left and right panels are for normal and inverted hierarchy respectively [15].

can have their magnetic charge g quantized via $eg = n\hbar c/2$, where n can take positive or negative integer values [150,151]. MM solutions of the classical equations of motion for spontaneously broken non-Abelian gauge theories [152,153] lead to a lower bound on the mass of the monopole: $M_{\rm MM} \geq M_X/G$, where M_X is the mass of the carrier of the unified interaction and G is the unified coupling constant. The MMs are therefore expected to have large masses. They are expected to be created during the Big-Bang, and being heavy, their relative speed with respect to Earth should be of the same order of magnitude as the speed of the galaxy, i.e. $\sim 10^{-3}c$. The MMs that enter the Earth lose their energy gradually by electromagnetic interactions with the surrounding medium [154]. If their mass is small, so will be their kinetic energy and they will be stopped in the Earth matter. The heavier MMs can however penetrate large distances, and can reach deep inside the Earth, like in the ICAL cavern.

Monopoles would be accelerated in the magnetic field of the galaxy, and hence energy would be drained from the galactic magnetic field. As the rate of this energy loss should be small over the time-scale of regeneration of the galactic magnetic field, an upper bound on the MM flux can be obtained [155]. This bound on the MM flux, called the Parker limit, is about 10^{-15} cm^{-2} s^{-1} sr^{-1} for $M_{\rm MM} \leq 10^{17}$ GeV. For higher masses, the bound increases linearly. The detectors used for detecting MM are mainly based either on the principle of induction or excitation/ionization. The induction method, where the induced magnetic field is measured using a superconducting quantum interferometer device (SQUID) [156,157], has yielded the upper bound on the MM flux to be $\sim 3.8 \times 10^{-13}$ cm^{-2} s^{-1} sr^{-1}. The ionization method has been used in Cherenkov detectors [158,159], as well as in scintillators and gaseous detectors [160–162]. The bounds from these experiments are much tighter – for example, the current best bound for 10^{10} GeV $< M_{\rm MM} < 10^{16}$ GeV is $\sim 2.8 \times 10^{-16}$ cm^{-2} s^{-1} sr^{-1}, from the MACRO experiment [161]. MMs have also been looked for in accelerator-based experiments [163–165].

When MMs pass through the ICAL, the ionization produced in the RPC detectors can be detected as a pulse which carries the information that there has been a hit, and the time of the hit. As the momentum of the MMs would be large, they will transfer only a small fraction of it to the detector, and will travel through the detector in a straight line, almost unaffected. The large surface area of the ICAL, combined with the large number of layers the MMs will be able to pass through, makes the MM detection possible. The track of the MM in the ICAL and the characteristic sequence of trigger times of consecutive layers of RPCs will help in identifying the MM against the background. Here we focus on MMs with masses 10^7–10^{17} GeV and speeds $10^{-3}c$–$0.7c$ [16]. (The results are presented in terms of $\beta \equiv v/c$ of the particle.) In this parameter space, if the MM flux is near the Parker limit, a few events per year may be expected at ICAL. On the other hand, the non-observation of such events will allow ICAL to put strong bounds on the incoming MM flux.

7.2.1 *Monopole simulation for ICAL.* The ICAL detector response for the monopole events is simulated using GEANT4, wherein the ICAL detector geometry is defined. A rock mass of 2.89 g/cc density and 1.3 km height from the top surface of the detector is considered in addition to the ICAL itself. Particles are incident on the surface of the rock, and pass through it before being detected in ICAL. An isotropic flux of downward-going MMs is taken into account by smearing it over the zenith angle ($\cos\theta$) from 0 to $\pi/2$, and uniformly over the 2π range of the azimuthal angle ϕ.

The stopping power in the rock of the Earth and the iron of the ICAL are taken care of using [166–168]

$$-\frac{\mathrm{d}E}{\mathrm{d}X} = \frac{4\pi N_e^2 g^2}{m_e c^2}\left[\ln\left(\frac{2m_e c^2\beta^2\gamma^2}{I_m}\right) - \frac{1}{2} - \frac{\delta_m}{2} - B(|g|) + \frac{K(|g|)}{2}\right]. \quad (7.5)$$

Particles also lose energy in the active region of the detector which has a gas mixture [R134A (95.15%), isobutane (4.15%) and SF_6 (0.34%)], and register hits, whose position and time information is recorded. This allows the reconstruction of the velocity of the particle.

We use the time-of-flight method for identifying the MM using ICAL. For relativistic monopoles, the high-energy muons will constitute the main background. We avoid this background by focussing on the events with $\beta < 0.8$. In the smaller velocity region, the background will be due to chance coincidences. This can also be minimized by choosing only those events which cross a certain minimum number of layers: if the noise rate per pick-up strip is $\mathcal{R}$ and the speed of the particle is βc, the probability of getting random hits in n consecutive layers in the relevant time window is $nR^n(nd/\beta c)^{n-1}$, where d is the distance between two layers. Thus, for $R \sim 200$ Hz and $\beta = 0.1$, for example, each additional layer will decrease the probability of chance coincidence by $\sim 10^{-5}$. We require the particle to cross at least 10 RPC layers, which will suppress both the high-β and low-β backgrounds to negligible levels. For each mass and β, we use a sample of 10,000 events to estimate the detector efficiency. The result is shown in the left panel of figure 7.3. It may be observed that the efficiency is almost 90% for $M_{\mathrm{MM}} > 10^{12}$ GeV and $10^{-3} < \beta < 0.1$.

7.2.2 *Reach for limits on the monopole flux.* The event rate expected at ICAL may be estimated by taking the area A of the top surface as the effective area, and the solid angle in which the MM will cross the cut of the minimum number of layers as the effective solid angle Ω. If the MM flux is f and the detector efficiency is ϵ, the expected number of events N_{ex} after a running time T of the detector will be

$$N_{\mathrm{ex}} = f(\mathrm{cm}^{-2}\ \mathrm{sr}^{-1}\ \mathrm{s}^{-1})A(\mathrm{cm}^2)\Omega(\mathrm{sr})T(\mathrm{s})\epsilon. \quad (7.6)$$

If the total observed number of events N_{obs} is not significantly greater than the expected number of background events N_{BG}, then an upper bound on the MM flux may be obtained. In the right panel of figure 7.3, we present the upper bound that will be obtained at the 50 kt ICAL in 10 years, in the scenario $N_{\mathrm{obs}} = N_{\mathrm{BG}} = 0$ for different β values. From the figure, it may be observed that an upper bound of $\sim 2 \times 10^{-16}$ cm^{-2} s^{-1} sr^{-1} (90% CL) should be possible with an exposure of 500 kt-yr of the ICAL detector. This is fairly competitive with the current strongest bound coming from MACRO [161]. Indeed, a direct comparison for $\beta = 0.1$ shows that for $M_{\mathrm{MM}} \lesssim 10^{16}$ GeV, the ICAL reach is clearly better. Monopoles with higher masses can penetrate through the Earth, and the additional up-going events accessible to the detector cause the increase in the sensitivity of MACRO as seen in the figure. Our analysis presented here is restricted to the flux from the upper hemisphere, and the upward-going events at high monopole masses have not been taken into account. With additional detectors on the walls and ceiling of the cavern, the sensitivity of ICAL to MMs can be increased by about a factor of 2 [16].

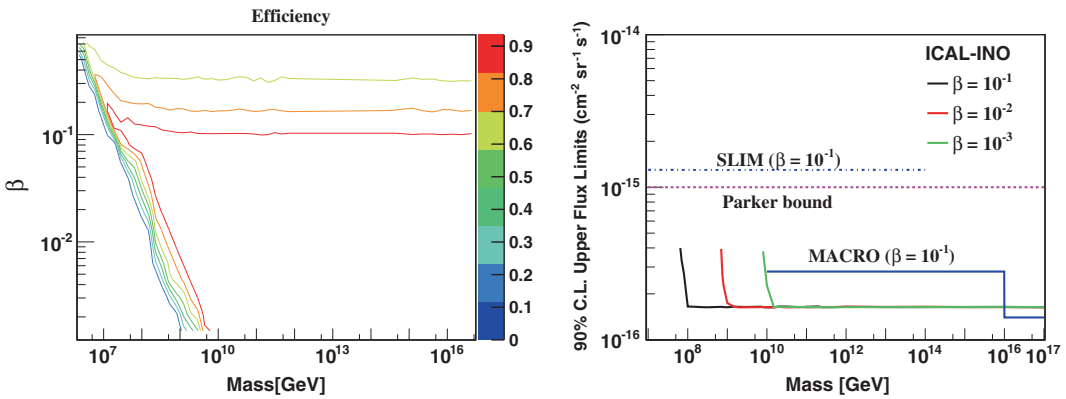

Figure 7.3. The left panel shows the efficiency of the detector for MM events, with cuts on the maximum value of β and the minimum number of layers to be traversed by the particle. The right panel indicates the 90% upper bounds on the MM flux expected from 10 year running of the 50 kt ICAL, if the number of candidate events is zero [16]. The upper bounds obtained from the MACRO [161] and SLIM [162] have also been shown.

8. Concluding remarks

This review presents the first systematic study of the physics capabilities and potential of the ICAL detector. This includes the response of ICAL to the muons and hadrons produced in the ν_μ interactions in the detector, and an understanding of the physics reach of the experiment for the identification of neutrino mass hierarchy and precision measurements of the atmospheric mixing parameters.

The ICAL detector geometry, and its elements such as iron plates, RPCs, the magnetic field, etc. are coded in the GEANT4 simulation framework. At this stage the atmospheric neutrino fluxes used are those at the Kamioka site. However, the fluxes at the INO site will soon be incorporated. The atmospheric muon neutrino-induced events are generated using the NUANCE neutrino generator.

The ICAL detector is sensitive to muons in the GeV range. The muon momenta are reconstructed using a Kalman filter algorithm that uses the bending of muons in the magnetic field. It enables the reconstruction of muons with an efficiency of more than 80%, and the measurement of its momentum with a precision of ∼20% (10%) at 1 GeV (10 GeV). The muon charge is identified correctly with an efficiency of more than 98% for $E_\mu > 4$ GeV, while the zenith angle of the muon at the point of production can be reconstructed to within a degree.

The reconstruction of multi-GeV hadrons is a unique feature of the ICAL. Using calibration against the number of hits in the detector, the energy of a hadron shower can be reconstructed to ∼85% (35%) at 1 GeV (15 GeV). The addition of the hadron energy information enhances the reach of ICAL much above that from the muon information alone. The optimal analysis method to obtain the best sensitivity seems to be the analysis that uses these three quantities in each event, without trying to reconstruct the neutrino energy or direction itself.

The simulation studies have included various systematic uncertainties from neutrino fluxes and cross-sections. However, some detector systematics, like the background contributions from misidentified neutral current events, have not yet been included in the analyses. The studies show that with 10 years run of the 50 kt ICAL, the mass hierarchy may be identified with a significance of $\chi^2 \geq 9$, i.e. more than 3σ. At the same time, the values of the atmospheric mixing parameters $|\Delta m^2_{32}|$ ($\sin^2\theta_{23}$) may be determined to a precision of 3% (12%). The identification of the octant of θ_{23} with the ICAL alone is limited to a 2σ significance even for favourable ranges of the parameter.

Detection of the atmospheric neutrinos with ICAL is rather insensitive to the value of δ_{CP}. This means that its reach for the mass hierarchy identification does not depend on the actual value of δ_{CP}, unlike the ongoing fixed-baseline experiments. As it provides a dataset that is free of the ambiguities due to the unknown δ_{CP}, the addition of the ICAL data to the long-baseline data of the ongoing experiments will enhance the δ_{CP} reach of these experiments. This synergy of the ICAL with other concurrent experiments should be exploited.

Given the multipurpose nature of ICAL, it can also be used for exploring exotic physics scenarios like CPT violation, magnetic monopoles, dark matter, etc., and more such avenues of using the ICAL data are sure to be found in years to come. The simulation studies presented in this report make a strong physics case for the ICAL detector. The codes and algorithms used in the analyses will be improved and fine-tuned to make them more realistic and efficient. This is expected to be a continually ongoing effort.

In parallel with the simulations described in this Review, efforts have gone on to finalize the design and structure of the ICAL detector modules, including the magnet, the RPCs, and their associated electronics. A prototype 1:8 scale model is planned to be built in Madurai, India, where most of the design will be validated. In the meantime, many more exciting and novel ideas are in the pipeline, and will be presented in future versions of this report.

The Government of India has recently (Dec. 2014) given the final approval for the establishment of INO, giving a big boost to the project. The INO Collaboration currently has more than 20 participating institutes from India, and welcomes the participation of high-energy physicists from all over the world.

Acknowledgements

The simulation and physics analysis of the ICAL detector would not have been possible without those who have set up the simulation framework for INO on multiple platforms; the authors would like to especially thank Pavan Kumar and P Nagaraj, as well as the computing resource personnel in all the institutions where this work was carried out. The authors are grateful to Dave Casper for making the NUANCE neutrino generator software freely available, and answering a long list of questions on its use in the initial stages. The authors also thank Sunanda Banerjee for sharing his expertise on GEANT. The authors would also like to express

their gratitude towards M Honda, who has provided us the detailed theoretical predictions of atmospheric neutrino fluxes, at the Super-Kamiokande site as well as at the INO site.

Such a large endeavour is not possible without direct or indirect support from many of the colleagues. While it is not possible to mention the names of everyone here, the authors would like to thank Debajyoti Choudhury, Anindya Datta, Anjan Joshipura, Namit Mahajan, Subhendra Mohanty, and many international colleagues who have worked on phenomenological aspects of atmospheric neutrino oscillations, and whose ideas have been developed into some of the physics analysis issues discussed in this Review. Many students and postdocs have contributed to the development and testing of the simulation framework in the initial stages, and to the early results. The authors would like to make a special mention of Abhijit Bandyopadhyay, Subhendu Chakrabarty, G K Padmashree, Arnab Pal, Subhendu Rakshit, Vikram Rentala, and Abhijit Samanta, who have worked on simulations related to atmospheric neutrino oscillations.

While this Review deals with the simulations of the ICAL detector, these simulations are based on the detector development that has been taking place in parallel, and the feedback of the hardware colleagues has been crucial in fine-tuning these simulations. The authors would therefore like to thank D N Badodkar, M S Bhatia, N S Dalal, S K Thakur, S P Prabhakar, and Suresh Kumar for the development and simulation of the magnet; Anita Behere, Nitin Chandrachoodan, S Dhuldhaj, Satyajit Jena, S R Joshi, N Krishnapurna, S M Lahamge, P K Mukhopadhyay, P Nagaraj, B K Nagesh, S Padmini, Shobha K Rao, Anil Prabhakar, Mandar Saraf, R S Shastrakar, K M Sudheer, M Sukhwani, and S S Upadhya for electronics development; Sarika Bhide, Manas Bhuyan, Suresh Kalmani, L V Reddy, R R Shinde, and Piyush Verma for the detector development. The authors would also like to thank Manoj Kumar Jaiswal, N Raghuram, and Vaibhav Pratap Singh, students who have completed their projects related to ICAL hardware.

The authors would like to thank K S Gothe, Kripa Mahata, Vandana Nanal, Sreerup Raychaudhuri, and Aradhana Shrivastava for their invaluable help in running the INO Graduate Training Program (INO GTP). The authors gratefully acknowledge the guidance from C V K Baba (deceased), Pijushpani Bhattacharjee, Ramanath Cowsik, J N Goswami, S K Ghosh, H S Mani, V S Narasimham, Sudhakar Panda, Raj Pillay, Amit Roy, D P Roy, Probir Roy, Utpal Sarkar, C P Singh, and Bikash Sinha from time to time.

The authors thank the Homi Bhabha National Institute (HBNI) for accepting the INO GTP in its ambit. The authors are grateful to TIFR, which has been the host institute for INO, for making its resources available for INO, including for the GTP. The authors would also like to acknowledge BARC for all the support it has provided over the years, and for acting as the host constituent institution of HBNI for the INO GTP.

Finally, the authors are grateful to the Department of Atomic Energy and the Department of Science and Technology, Government of India, for funding the INO project. The authors would also like to acknowledge the funding provided by the University Grants Commission for many of the students working on INO and ICAL, without which this review would not have been possible.

Appendix A. Neutrino fluxes at the Kamioka and INO sites

In this section, we briefly discuss the preliminary atmospheric neutrino flux calculations corresponding to the INO site, and compare them with those for the Kamioka site. This work is based on refs [5] and [100]. The primary cosmic ray flux model based on AMS [169] and BESS [170,171] data has been used, and the hadronic interactions have been implemented with DPMJET-III [172] above 32 GeV, and JAM below 32 GeV. For the propagation of cosmic rays in the atmosphere, the model NRLMSISE-00 [173], which takes into account the temperatures and densities of the

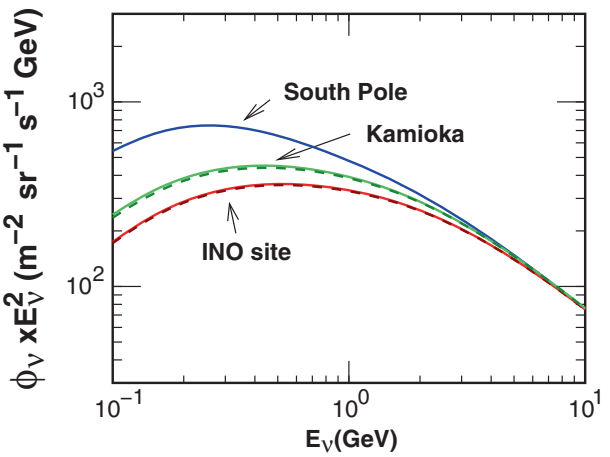

Figure A.1. Atmospheric neutrino flux averaged over all directions and summed over $\nu_e + \bar{\nu}_e + \nu_\mu + \bar{\nu}_\mu$, as a function of neutrino energy for Super-Kamiokande, INO, and South Pole sites. This is for all the energy ranges of the calculation. The fluxes calculated with US-standard76 are also plotted in dashed line for the Kamioka and the INO sites.

atmosphere's components and takes care of the position dependence and the time variation in a year, is used. The geomagnetic field model used is IGRF2010 [174]. The atmospheric neutrino flux is obtained using a three-dimensional scheme below 32 GeV, and a one-dimensional scheme above that. The flux calculated in both the schemes agree with each other at 32 GeV [5].

Figure A.1 shows the calculated atmospheric neutrino flux averaged over one year by folding over all directions and summing over all types of neutrinos ($\nu_e, \bar{\nu}_e, \nu_\mu, \bar{\nu}_\mu$) for the Super-Kamiokande, INO and South Pole sites. These results, obtained with the NRLMSISE-00 model, agree well with those obtained from the US-standard76 [175] model. However, the fluxes with the NRLMSISE-00, as used here, have an advantage in the study of seasonal variations, which can be appreciable at the INO site.

It is observed that the total flux at INO is slightly smaller than that at Kamioka at low energies ($E \lesssim 3$ GeV), but the difference becomes small with the increase in neutrino energy. It may be noted that this is true only for the angle-integrated fluxes. Figure A.2 shows the zenith angle dependence (integrating over all azimuthal angles) of fluxes at Kamioka and at the INO site at two values of energy. It is found that at 1 GeV, there are large up–down asymmetries in the fluxes at the INO site; the upward-going flux is larger than the downard-going one. These asymmetries decrease with the increase in neutrino energy and almost disappear at 10 GeV.

The results for the atmospheric neutrino fluxes as functions of the azimuthal angle ϕ, in five zenith angle bins, are shown in figure A.3 for Kamioka and in figure A.4 for the INO site. These results are presented

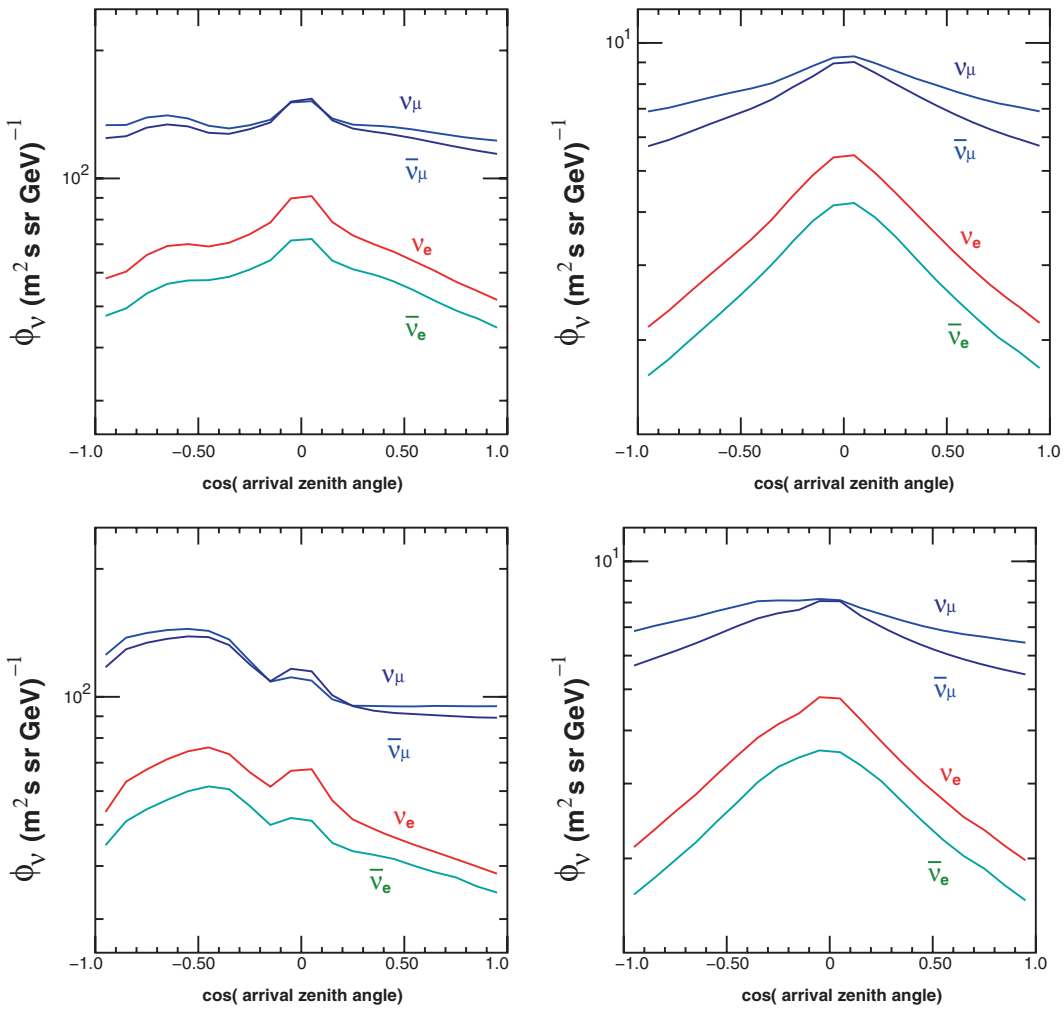

Figure A.2. The zenith angle dependence of atmospheric neutrino flux at $E = 1.0$ GeV (left) and $E = 3.2$ GeV (right), averaged over all azimuthal angles calculated for the Super-Kamiokande (top) and the INO (bottom) sites. Here θ is the arrival direction of the neutrino, with $\cos\theta = 1$ for vertically downward-going neutrinos and $\cos\theta = -1$ for vertically upward-going neutrinos.

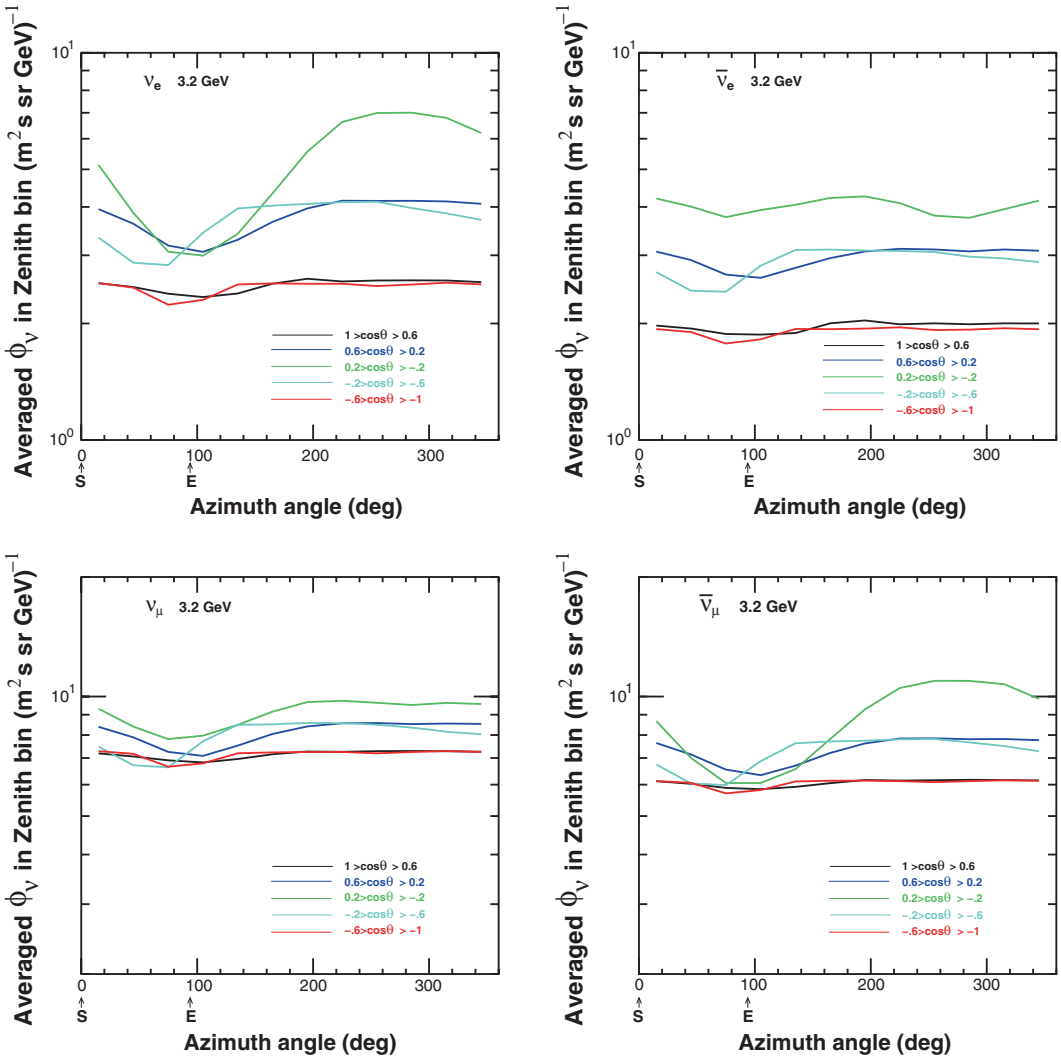

Figure A.3. The azimuthal angle dependence of atmospheric neutrino flux, averaged over zenith angle bins calculated for the Super-Kamiokande site for ν_e at $E = 3.2$ GeV.

for ν_e, $\bar{\nu}_e$, ν_μ, and $\bar{\nu}_\mu$, for the (anti)neutrino energy of 3.2 GeV. It is observed that even for such a high energy, the variation of the atmospheric neutrino flux has a complex structure. This is a result of the rigidity cut-off and muon bending in the geomagnetic field. At the INO site, the horizontal component of the geomagnetic field is ∼40 μT, larger than that at Kamioka, where it is ∼30 μT, and so the azimuthal angle dependence is also more complex. This complex azimuthal angle dependence continues even above 10 GeV for the near horizontal directions.

The atmospheric electron neutrino flux also shows a rapid variation in the azimuth angles, but the statistical errors in the simulations of production of atmospheric neutrinos are still large, and more statistics is needed for a better understanding. As the INO site is close to the equator, the seasonal variation is also expected, the calculation for which is also in progress. These updates are expected to be reported after the accumulation of sufficient statistics.

Detailed physics re-analyses with the fluxes at the INO site need to be carried out in order to determine the final physics potential of ICAL. However, the effect of the change of flux may be estimated by comparing the number of events calculated using the fluxes at Kamioka and at the INO site. The comparison of the number of μ^- and μ^+ events at these two sites, as a function of the muon energy, is shown in figure A.5. For the sake of this sample comparison, we have considered charged-current muon events in the energy range 1–11 GeV, with no oscillations, 100% efficiency for detection and charge identification of muons and extremely accurate energy measurement.

The total number of muon events will be less with the fluxes at the INO site. As a result, the performance

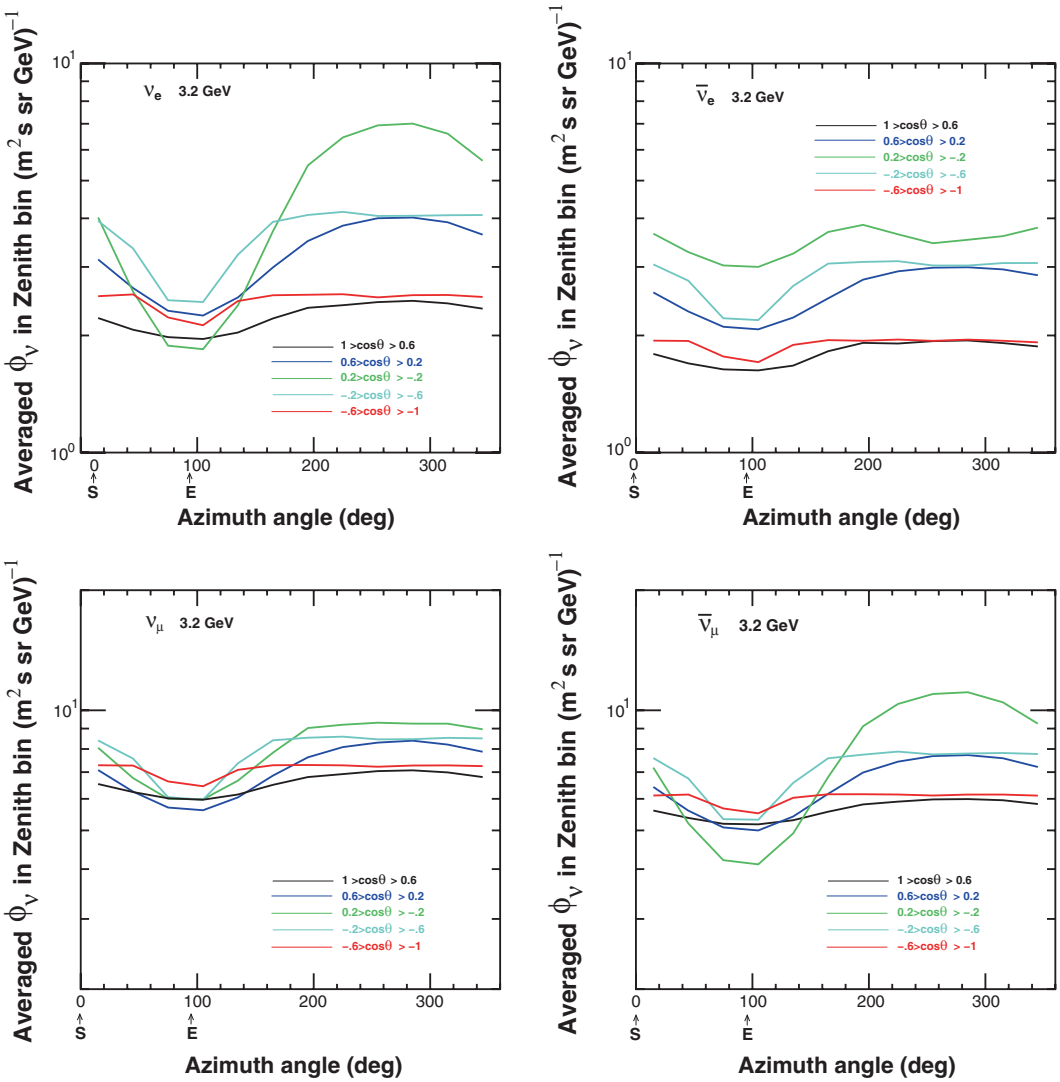

Figure A.4. The azimuthal angle dependence of atmospheric neutrino flux, averaged over zenith angle bins calculated for the INO site for ν_e at $E = 3.2$ GeV.

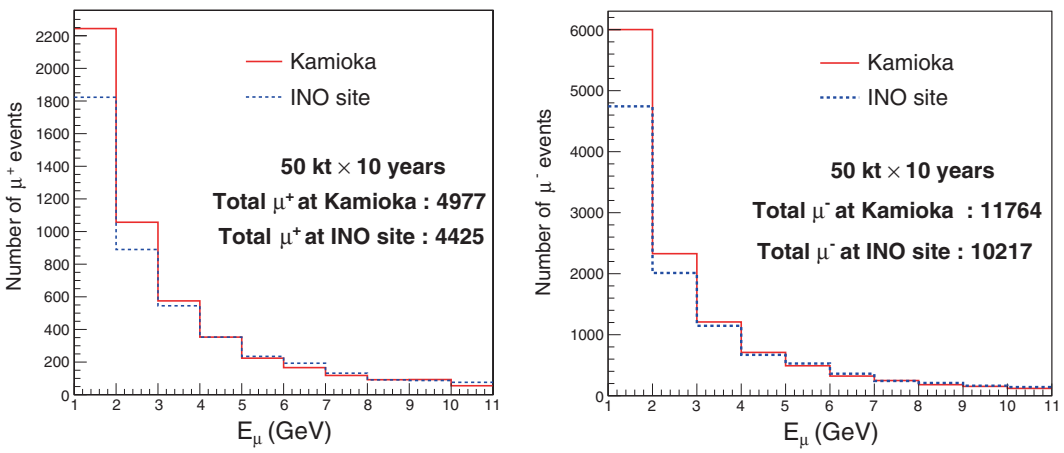

Figure A.5. Comparisons of energy distributions of μ^- and μ^+ events in 500 kt-yr of ICAL, with no oscillations, 100% efficiency for detection and charge identification of muons and extremely accurate energy measurement.

may be expected to be slightly worse than that calculated from the Kamioka fluxes. The extent to which the performance will be affected will depend on the quantity of interest, though. For example, the accuracy in the measurement of $\sin^2 2\theta_{23}$ typically is controlled by the total number of events. As the total number of events with the fluxes at the INO site are about 14% smaller, we expect to take about 14% additional exposure to obtain the same level of accuracy as described in this review. On the other hand, as has been pointed out in figure 5 of [14], the hierarchy sensitivity comes mainly from the events with muon energy greater than 4 GeV. As figure A.5 indicates, the numbers of such muon events calculated using the two fluxes are nearly the same within statistical uncertainties. The results for the mass hierarchy determination are thus expected to be unaffected.

Appendix B. Neutrino oscillation probabilities in matter

Neutrino oscillation probabilities in matter are obtained by solving the propagation equation, which may be written in the flavour basis as

$$i\frac{\mathrm{d}|\nu_\alpha(x)\rangle}{\mathrm{d}x} = H|\nu_\alpha(x)\rangle, \tag{B.1}$$

where $|\nu_\alpha(x)\rangle = (\nu_e(x), \nu_\mu(x), \nu_\tau(x))^T$. H is the effective Hamiltonian, given as

$$H = \frac{1}{2E}\, U\ \mathrm{diag}(0, \Delta m^2_{21}, \Delta m^2_{31})U^\dagger + \mathrm{diag}(V(x), 0, 0). \tag{B.2}$$

Here E is the energy of the neutrino and $\Delta m^2_{ij} = m^2_i - m^2_j$ is the mass-squared difference between the neutrino mass eigenstates. The PMNS mixing matrix U relates the neutrino flavour eigenstates and mass eigenstates. $V(x)$ is the matter potential arising due to the charged-current interaction of ν_e with electrons and is given in terms of the electron density n_e by $V(x) = \sqrt{2}G_F n_e(x)$. For antineutrinos, $U \to U^*$ and $V \to -V$. In general, for an arbitrary density profile one needs to solve the above equation numerically to obtain the probabilities. However, simplified analytic expressions can be obtained by assuming constant matter density. In such cases, one can diagonalize the above Hamiltonian to obtain

$$H = \frac{1}{2E}\, U^{\mathrm{m}}\ \mathrm{diag}((m^{\mathrm{m}}_1)^2, (m^{\mathrm{m}}_2)^2, (m^{\mathrm{m}}_3)^2)U^{\mathrm{m}\dagger}, \tag{B.3}$$

where m^{m}_i and U^{m} denote the mass eigenvalues and mixing matrix in matter respectively. For a neutrino travelling a distance L, the flavour conversion probability in matter of constant density has an analogous expression as in the case of vacuum (see eq. (1.2)), and can be expressed as

$$P_{\alpha\beta}(L) = \delta_{\alpha\beta} - 4\sum_{j>i}\mathrm{Re}(U^{\mathrm{m}}_{\alpha i}U^{\mathrm{m}\star}_{\beta i}U^{\mathrm{m}\star}_{\alpha j}U^{\mathrm{m}}_{\beta j})\sin^2\Delta^{\mathrm{m}}_{ij} + 2\sum_{j>i}\mathrm{Im}(U^{\mathrm{m}}_{\alpha i}U^{\mathrm{m}\star}_{\beta i}U^{\mathrm{m}\star}_{\alpha j}U^{\mathrm{m}}_{\beta j})\sin(2\Delta^{\mathrm{m}}_{ij}), \tag{B.4}$$

where the quantity Δ^{m}_{ij} in the presence of matter is defined as

$$\Delta^{\mathrm{m}}_{ij} = \frac{1.27\ (\Delta m^2_{ij})^{\mathrm{m}}(\mathrm{eV}^2)\ L(\mathrm{km})}{E(\mathrm{GeV})},$$

with $(\Delta m^2_{ij})^{\mathrm{m}} = (m^{\mathrm{m}}_i)^2 - (m^{\mathrm{m}}_j)^2$ the difference between the squares of the mass eigenvalues m^{m}_i and m^{m}_j in matter.

To obtain tractable expressions, further assumptions need to be made. Many approximate analytic expressions for probabilities exist in the literature. However, different assumptions that lead to different approximate forms have different regimes for validity. To understand the results presented in this review, the probability expressions obtained under the following two approximations are mostly relevant:

- the one mass scale dominance (OMSD) approximation which assumes $\Delta m^2_{21} = 0$,
- the double expansion in terms of small parameters $\alpha = \Delta m^2_{21}/\Delta m^2_{31}$ and $\sin\theta_{13}$ [176,177].

The condition on the neutrino energy and baseline for the validity of both approximations can be expressed as $\Delta m^2_{21}L/E \ll 1$. This translates to $L/E \ll 10^4$ km/GeV for typical values of the solar mass-squared difference Δm^2_{21}, and hence to $L \leq 10^4$ km for neutrinos of energy $\mathcal{O}$(GeV). Thus, these approximations are valid for most of the energy and path length ranges considered here. The OMSD approximation is exact in θ_{13} and works better near the resonance region. Below we give the probabilities relevant for the study presented in this Review in both OMSD and double expansion approximations, and discuss in which L and E regimes these are appropriate. Note that we give the expressions only for neutrino propagation through a constant matter density. This approximation is not applicable for neutrinos passing through the Earth's core. However, it is enough for an analytic understanding of our arguments. All our numerical calculations take the variation of Earth's density into account through the preliminary reference Earth model (PREM).

Appendix B.1: *One mass scale dominance approximation*

In this approximation, the Hamiltonian in eq. (B.2) can be exactly diagonalized analytically. Below we give the expressions for the muon neutrino survival probability $P(\nu_\mu \to \nu_\mu) \equiv P_{\mu\mu}$ and conversion probability of electron neutrinos to muon neutrinos $P(\nu_e \to \nu_\mu) \equiv P_{e\mu}$, which are relevant for the atmospheric neutrinos at ICAL because the detector is sensitive to muon flavour. In the OMSD approximation, these can be expressed as

$$\begin{aligned} P_{\mu\mu} &= 1 - \cos^2\theta_{13}^{\mathrm{m}}\ \sin^2 2\theta_{23} \\ &\quad \times \sin^2\left[1.27(\Delta m^2_{31} + A + (\Delta m^2_{31})^{\mathrm{m}})L/2E\right] \\ &\quad - \sin^2\theta_{13}^{\mathrm{m}}\ \sin^2 2\theta_{23} \\ &\quad \times \sin^2\left[1.27(\Delta m^2_{31} + A - (\Delta m^2_{31})^{\mathrm{m}})L/2E\right] \\ &\quad - \sin^4\theta_{23}\ \sin^2 2\theta_{13}^{\mathrm{m}}\ \sin^2\left[1.27\Delta m^2_{31}L/E\right], \end{aligned} \tag{B.5}$$

and

$$P_{e\mu} = \sin^2\theta_{23}\ \sin^2 2\theta_{13}^{\mathrm{m}}\ \sin^2\left[1.27(\Delta m^2_{31})^{\mathrm{m}}L/E\right]. \tag{B.6}$$

In the above expressions, $(\Delta m^2_{31})^{\mathrm{m}}$ and $\sin 2\theta_{13}^{\mathrm{m}}$, the mass-squared difference and mixing angle in matter, respectively, are given by

$$\begin{aligned} (\Delta m^2_{31})^{\mathrm{m}} &= \sqrt{(\Delta m^2_{31}\cos 2\theta_{13} - A)^2 + (\Delta m^2_{31}\sin 2\theta_{13})^2}, \\ \sin 2\theta_{13}^{\mathrm{m}} &= \sin 2\theta_{13}\frac{\Delta m^2_{31}}{(\Delta m^2_{31})^{\mathrm{m}}}, \end{aligned} \tag{B.7}$$

where

$$\begin{aligned} A(\mathrm{eV}^2) &= 2EV = 2\sqrt{2}G_F n_e E \\ &= 0.76 \times 10^{-4}\ \rho(\mathrm{g/cc})\ E(\mathrm{GeV}). \end{aligned}$$

When $A = \Delta m^2_{31}\cos 2\theta_{13}$, we see a resonance. The resonance energy is given by

$$E_{\mathrm{res}} = \frac{\Delta m^2_{31}\cos 2\theta_{13}}{2\sqrt{2}G_F n_e}. \tag{B.8}$$

In table B.1, we give the average resonance energies for neutrinos travelling a given distance L through the Earth, for baselines ranging from 1000 to 10,000 km.

Table B.1. Values of E_{res} at various baselines using the line-averaged PREM [178] density ρ_{avg}. We have used $\Delta m^2_{31} = 2.5 \times 10^{-3}$ eV^2 and $\sin^2 2\theta_{13} = 0.1$.

L (km)	ρ_{avg} (g/cc)	E_{res} (GeV)
1000	3.00	9.9
3000	3.32	9.4
5000	3.59	8.7
7000	4.15	7.5
10000	4.76	6.6

It is seen from the table that the resonance energy is in the range 6–10 GeV for path lengths in the range 1000–10,000 km. These ranges are relevant for atmospheric neutrinos passing through Earth and hence provide an excellent avenue to probe resonant Earth matter effects. The importance of this can be understood by noting that the resonance condition depends on the sign of Δm^2_{31}. For $\Delta m^2_{31} > 0$ there is a matter enhancement in θ_{13}^{m} for neutrinos, and a matter suppression in θ_{13}^{m} for antineutrinos (as $A \to -A$). The situation is reversed for $\Delta m^2_{31} < 0$. Thus, matter effects can differentiate between the two hierarchies and detectors with charge sensitivity (like ICAL) are very suitable for probing this.

For atmospheric neutrinos in ICAL, the most relevant probability is $P_{\mu\mu}$. The significance of the $P_{e\mu}$ channel is less than that of $P_{\mu\mu}$ for two reasons: the number of electron neutrinos produced in the atmosphere is smaller, and more importantly, the probability of their conversion to muon neutrinos is also usually smaller than $P_{\mu\mu}$, so that their contribution to the total number of events in ICAL is small. It is not completely negligible though, because the value of θ_{13} is moderately large.

Note that $P_{e\mu}$ does not attain its maximum value at $E = E_{\mathrm{res}}$ even though $\sin 2\theta_{13}^{\mathrm{m}}$ achieves its maximum value of unity at this energy, because the mass-squared difference $(\Delta m^2_{31})^{\mathrm{m}}$ hits a minimum [179]. The values of $(\Delta m^2_{31})^{\mathrm{m}} \sin 2\theta_{13}^{\mathrm{m}}$ and $P_{\mu e}$ remain small for path lengths of $L \lesssim 1000$ km. If L is chosen suitably large so as to satisfy $(1.27\Delta m^2_{31}\sin 2\theta_{13}L/E) \geq \pi/4$, then $P_{e\mu}$ can reach values ≥ 0.25 for $\sin^2 2\theta_{23} = 1$. One needs $L \gtrsim 6000$ km to satisfy the above condition. For such baselines and in the energy range 6–8 GeV, the resonant Earth matter effects lead to $P_{e\mu}$ in matter being significantly greater than its vacuum value [180].

The muon neutrino survival probability is a more complicated function and can show both fall and rise above the vacuum value for longer baselines (∼10,000 km). Thus, the energy and angular smearing effects are more for $P_{\mu\mu}$. The maximum hierarchy sensitivity is achieved in this channel when resonance occurs close to a vacuum peak or dip, thus maximizing the matter effects because when there is resonant matter effect for one hierarchy, the probability for the other hierarchy closely follows the vacuum value. Figure B.1 shows oscillograms for muon neutrino and antineutrino survival probabilities in the case of normal hierarchy, in the plane of neutrino energy and cosine of the zenith angle θ_z. The plot in the left panel shows the resonant effect in the muon neutrino probabilities in the region between $\cos\theta_z$ between -0.6 to -0.8 and energy in the range 6–8 GeV. This feature is not present in the right panel because for the normal hierarchy, the muon antineutrinos do not encounter any resonance effect. The plot also shows the enhanced oscillation features due to the effects of the Earth's core ($\cos\theta_z$ between -0.8 and -1.0) for neutrinos. For the inverted hierarchy, the muon antineutrino survival probability will show resonance effects, whereas the neutrino probabilities will not. The ICAL detector being charge sensitive can differentiate between neutrino and antineutrino effects and hence between the two hierarchies.

Equations (B.5) and (B.6) can also help us understand the octant sensitivity of atmospheric neutrinos arising due to resonant matter effects. The leading-order term in $P_{e\mu}$ in vacuum depends on $\sin^2\theta_{23}\sin^2 2\theta_{13}$. Although this term is sensitive to the octant of θ_{23}, the uncertainty in the value of θ_{13} may give rise to octant degeneracies. In matter, the $\sin^2 2\theta_{13}^{\rm m}$ term gets amplified near resonance, and the combination $\sin^2\theta_{23}\sin^2 2\theta_{13}^{\rm m}$ breaks the degeneracy of the octant with θ_{13}. Also, the strong octant-sensitive nature of the term $\sin^4\theta_{23}\sin^2 2\theta_{13}^{\rm m}$ near resonance can overcome the degeneracy due to the $\sin^2 2\theta_{23}$-dependent terms. Unfortunately, the muon events in ICAL get contribution from both $P_{\mu\mu}$ channel and $P_{e\mu}$ channel, and the matter effect in these two channels act in opposite directions for most of the baselines. This causes a worsening in the octant sensitivity of muon events at atmospheric neutrino experiments.

The OMSD probabilities are in the limit $\Delta m^2_{21} = 0$ and have no dependence on the CP phase. These expressions match well with the numerical probabilities obtained by solving the propagation equation in the resonance region, i.e. for the baseline range 6000–10,000 km. Accelerator-based experiments like T2K and NOνA have shorter baselines and lower matter effects, and lie far from resonance. For these experiments, the dominant terms in $P_{\mu\mu}$ are insensitive to the hierarchy and octant. Consequently, the relative change in probability due to the hierarchy/octant-sensitive subdominant terms is small. Therefore, the $P_{\mu\mu}$ oscillation channel does not contribute much to the hierarchy and octant sensitivity of T2K and NOνA. However, these experiments get their sensitivity primarily from the $\nu_\mu \to \nu_e$ conversion probability. For this case, the double expansion up to second order in α and $\sin\theta_{13}$ works better.

Appendix B.2: *Double expansion in* α *and* $\sin\theta_{13}$

In accelerator experiments, high-energy pions or kaons decay to give muons and muon neutrinos/antineutrinos. One can study the muon neutrino conversion probability $P(\nu_\mu \to \nu_e) \equiv P_{\mu e}$ in these with a detector sensitive to electron flavour. In order to study the effect due to Δm^2_{21} and the CP phase $\delta_{\rm CP}$ it is convenient to write down the probabilities as an expansion in terms of the two small parameters, $\alpha = \Delta m^2_{21}/\Delta m^2_{31}$ and

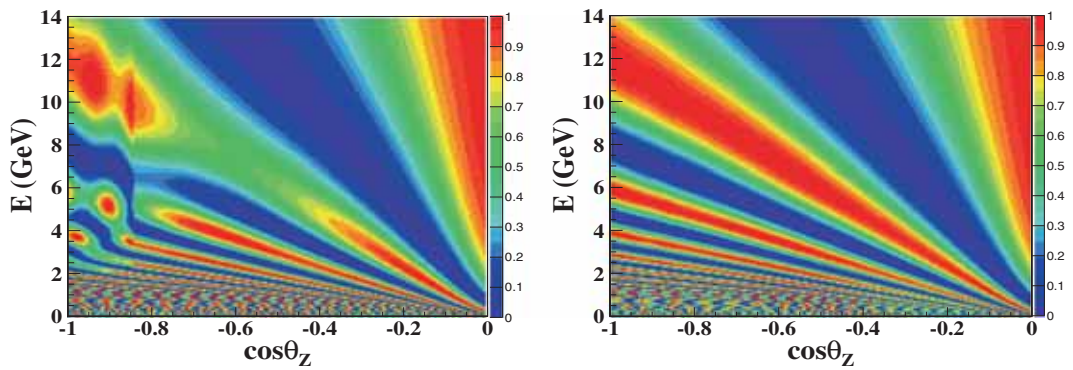

Figure B.1. The oscillograms for the muon neutrino (left panel) and antineutrino (right panel) survival probabilities during their passage through Earth in E–$\cos\theta_z$ plane. The oscillation parameters used are $\theta_{23} = 45°$, $\delta_{\rm CP} = 0$, $\Delta m^2_{31} = +2.45 \times 10^{-3}$ eV^2 (NH) and $\sin^2 2\theta_{13} = 0.1$.

$\sin\theta_{13}$, to second order (i.e. terms up to α^2, $\sin^2\theta_{13}$ and $\alpha\sin\theta_{13}$ are kept) [176,177].

$$\begin{aligned} P_{\mu e} &= \sin^2 2\theta_{13}\sin^2\theta_{23}\frac{\sin^2[(1-\hat{A})\Delta]}{(1-\hat{A})^2} \\ &+ \alpha\sin 2\theta_{13}\sin 2\theta_{12}\sin 2\theta_{23}\cos(\Delta+\delta_{\rm CP}) \\ &\times \frac{\sin(\hat{A}\Delta)}{\hat{A}}\frac{\sin[(1-\hat{A})\Delta]}{(1-\hat{A})} \\ &+ \alpha^2\sin^2\theta_{12}\cos^2\theta_{23}\frac{\sin^2(\hat{A}\Delta)}{\hat{A}^2} \\ &+ \mathcal{O}(\alpha^3, \alpha^2 s_{13}, \alpha s_{13}^2, s_{13}^3). \end{aligned} \tag{B.9}$$

The notations used in writing the probability expressions are: $\Delta \equiv \Delta m^2_{31}L/4E$, $s_{ij}(c_{ij}) \equiv \sin\theta_{ij}(\cos\theta_{ij})$, $\hat{A} = 2\sqrt{2}G_F n_e E/\Delta m^2_{31}$. For neutrinos, the signs of $\hat{A}$ and Δ are positive (negative) for NH (IH). The sign of $\hat{A}$ as well as $\delta_{\rm CP}$ reverse for antineutrinos. This probability is sensitive to all the three current unknowns in neutrino physics – hierarchy, octant of θ_{23} as well as $\delta_{\rm CP}$ – and is often hailed as the golden channel. However, the dependences are interrelated and extraction of each of these unknowns depends on the knowledge of the others. Specially, the complete lack of knowledge of $\delta_{\rm CP}$ gives rise to the hierarchy-$\delta_{\rm CP}$ degeneracy as well as the octant-$\delta_{\rm CP}$ degeneracy in these experiments, through the second term in eq. (B.9).

The above expressions reduce to the vacuum expressions for shorter baselines for which $A \to 0$. For such cases there is no hierarchy sensitivity. The hierarchy sensitivity increases with increasing baseline and is maximum in the resonance region. The resonance energy at shorter baselines is >10 GeV and therefore these experiments cannot probe resonant Earth matter effects.

Appendix B.3: *Probability for reactor neutrinos*

A crucial input in the analysis presented in this Review is the value of θ_{13}, measured by the reactor neutrino experiments. The probability relevant for reactor neutrinos is the survival probability for electron antineutrinos $P(\bar{\nu}_e \to \bar{\nu}_e) \equiv P_{\bar{e}\bar{e}}$. Since reactor neutrinos have very low energy (order of MeV) and they travel very short distances (order of km), they experience negligible matter effects. The exact formula for the survival probability in vacuum is given by [180,181]

$$\begin{aligned} P_{\bar{e}\bar{e}} &= 1 - c_{13}^4\sin^2 2\theta_{12}\sin^2\Delta_{21} - \sin^2 2\theta_{13}\sin^2\Delta_{31} \\ &+ \sin^2 2\theta_{13}s_{12}^2[\sin^2\Delta_{31} - \sin^2\Delta_{32}]. \end{aligned} \tag{B.10}$$

As this is independent of $\delta_{\rm CP}$ and matter effects, the probability is the same for neutrinos and antineutrinos (assuming CPT conservation, i.e. the same mass and mixing parameters describing neutrinos and antineutrinos).

Appendix C. The Vavilov distribution function

The Vavilov probability distribution function is found to be suitable to represent the hit distributions of hadrons of a given energy in the ICAL, as has been observed from figure 4.8. The Vavilov probability density function in the standard form is defined by [182]

$$P(x;\kappa,\beta^2) = \frac{1}{2\pi i}\int_{c-i\infty}^{c+i\infty}\phi(s)\mathrm{e}^{xs}\mathrm{d}s, \tag{C.1}$$

where

$$\phi(s) = \mathrm{e}^C\mathrm{e}^{\psi(s)}, \quad C = \kappa(1+\beta^2\gamma) \tag{C.2}$$

and

$$\begin{aligned} \psi(s) &= s\ln\kappa + (s+\beta^2\kappa)\cdot\left[\int_0^1\frac{1-\mathrm{e}^{-st/\kappa}}{t}\,\mathrm{d}t - \gamma\right] \\ &- \kappa\mathrm{e}^{-s/\kappa}, \end{aligned} \tag{C.3}$$

where $\gamma = 0.577\ldots$ is the Euler's constant.

The parameters mean and variance (σ^2) of the distribution in eq. (C.1) are given by

$$\text{Mean} = \gamma - 1 - \ln\kappa - \beta^2; \quad \sigma^2 = \frac{2-\beta^2}{2\kappa}. \tag{C.4}$$

For $\kappa \le 0.05$, the Vavilov distribution may be approximated by the Landau distribution, while for $\kappa \ge 10$, it may be approximated by the Gaussian approximation, with the corresponding mean and variance.

We have used the Vavilov distribution function $P(x;\kappa,\beta^2)$ defined above, which is also built into ROOT, as the basic distribution for the fit. However, the hadron hit distribution itself is fitted to the modified distribution $(P_4/P_3)\,P((x-P_2)/P_3;\ P_0,\ P_1)$, to account for the x-scaling (P_3), normalization P_4 and the shift of the peak to a non-zero value, P_2. Clearly, $P_0 = \kappa$ and $P_1 = \beta^2$. The modified mean and variance are then

$$\begin{aligned} \text{Mean}_{\rm Vavilov} &= (\gamma - 1 - \ln P_0 - P_1)P_3 + P_2, \\ \sigma^2_{\rm Vavilov} &= \frac{(2-P_1)}{2P_0}P_3^2. \end{aligned} \tag{C.5}$$

These are the quantities used while presenting the energy response of hadrons in the ICAL detector.

Appendix D. Hadron energy resolution as a function of plate thickness

A potentially crucial factor in the determination of hadron energy and direction is the thickness of absorber material, namely iron plate thickness in ICAL. In all the simulation studies reported here, we have assumed that the thickness of the iron plate is 5.6 cm, which is the default value. While not much variation in this thickness is possible due to constraints imposed by total mass, physical size, location of the support structure, and other parameters like the cost factor etc., we look at possible variation of this thickness in view of optimizing the hadron energy resolution [10]. The hadron energy resolution is a crucial limiting factor in reconstructing the neutrino energy in atmospheric neutrino interactions in the ICAL detector. This information is also helpful because ICAL is modular in form and future modules may come in for further improvements using such analyses.

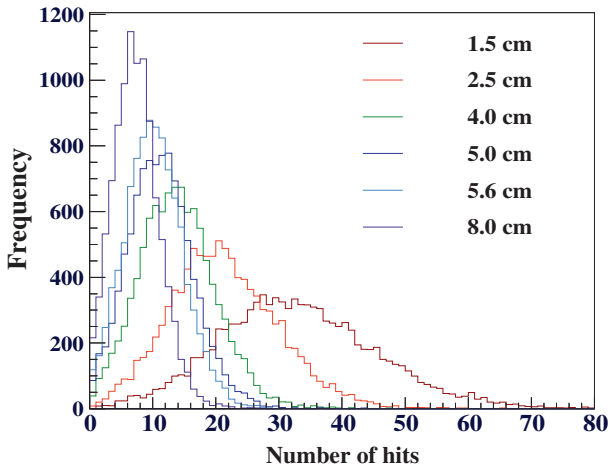

Figure D.1. Hit distribution of 5 GeV pions propagated through sample iron plate thicknesses [10].

Naively, this can be achieved by simply changing the angle of propagation of the particle in the simulation, because the effective thickness is $(t/\cos\theta)$. In the case of muons this itself may be sufficient to study the effect of plate thickness. However, in an actual detector, the detector geometry – including support structure, orientation as well as the arrangement of detector elements – imposes additional non-trivial dependence on thickness. Therefore, we study hadron energy resolution with the present arrangement of ICAL by varying the plate thickness, while other parameters are fixed. The analysis was done by propagating pions in the simulated ICAL detector at various fixed energies, averaged over all directions in each case.

The hit distribution patterns for 5 GeV pions propagated through sample plate thicknesses in the central region are shown in figure D.1. The methodology is already discussed in §4 and we shall not repeat it here. For comparing the resolutions with different thicknesses we use the mean and rms width (σ) of the hit distributions as functions of energy.

The hadron energy resolution is parametrized as

$$\left(\frac{\sigma}{E}\right)^2 = \frac{a^2}{E} + b^2, \tag{D.1}$$

where a is the stochastic coefficient and b is a constant, both of which depend on the thickness. We divide the relevant energy range 2–15 GeV into two subranges, below 5 GeV and above 5 GeV. Below 5 GeV, the quasielastic, resonance and deep inelastic processes contribute to the production of hadrons in neutrino interactions in comparable proportions, while above 5 GeV the hadron production is dominated by the deep inelastic scattering. The results for the energy resolution as a function of plate thickness are shown in figure D.2. Note that here, we show the square of the resolution instead of the resolution itself.

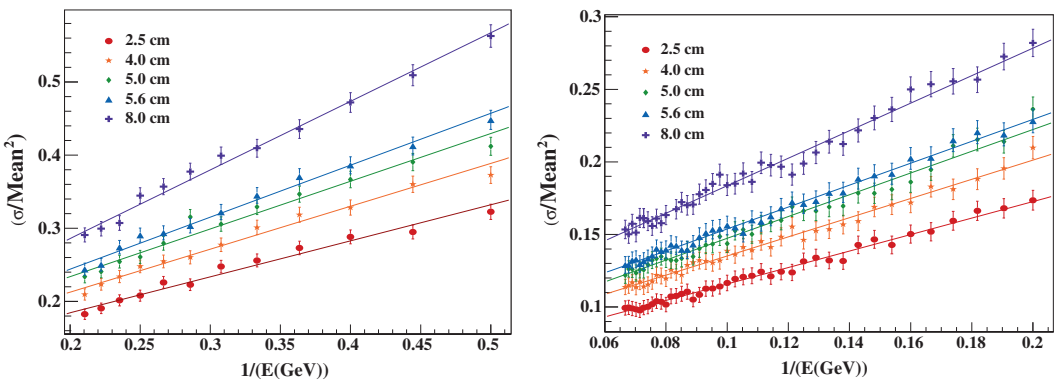

Figure D.2. Plots of $(\sigma/\text{mean})^2$ as a function of $1/E$. The data as well as fits to eq. (D.1) are shown in the energy range 2–4.75 GeV (left) and 5–15 GeV (right). The thickness is varied from 2.5 to 8 cm [10].

The stochastic coefficient a as a function of thickness is obtained from a fit to the hadron energy resolution, and is shown in figure D.3 as a function of plate thickness for the two energy ranges as in figure D.2.

The analysis in the two energy ranges shows that the thickness dependence is stronger than $\sqrt{t}$ which is observed in hadron calorimeters at high energies (tens of GeV) [183]. In fact, at the energies of relevance to us, the thickness dependence is not uniform but dependent on the energy. This is borne out by two independent analyses: in the first one we obtain the thickness dependence of the stochastic coefficient a and in the second analysis we directly parametrize the energy resolution as a function of thickness at each energy. Typically, instead of $t^{0.5}$, we find the power varying from about 0.65 to 0.98 depending on the energy.

Finally, we compare the ICAL simulations with varying thicknesses with MONOLITH and MINOS and their test beam runs. This is a useful comparison because test beam runs with ICAL prototype have not been done till now. The data from the above detectors can however be used for the validation of the ICAL simulations results.

The test beam results for the Baby MONOLITH (BM) detector at CERN with 5 cm thick iron plates [184,185] have been obtained when the beam energy is in the range 2–10 GeV. In order to provide a comparison, we have simulated the ICAL detector response with 5 cm iron plates, for single pions of 2–10 GeV energy incident normally on the detector at a fixed vertex. Also, in order to be consistent with the BM parametrization, the energy resolution σ_E/E is fitted to the function $A/\sqrt{E} + B$. A comparison of the ICAL-simulated results with the BM beam results, along with the respective fits, is shown in figure D.4.

For BM, an energy resolution of $\sigma_E/E = 68\%/\sqrt{E} + 2\%$ was reported [184]. However, no errors on the parameters A and B were specified. Our fit to the same BM data gives $A_{\mathrm{BM}} = (66 \pm 5)\%$ and $B_{\mathrm{BM}} = (1 \pm 2)\%$, which also gives an estimation of errors on these parameters. The fit for the ICAL resolution gives the parameter values $A_{\mathrm{ICAL}} = (64 \pm 2)\%$ and $B_{\mathrm{ICAL}} = (2 \pm 1)\%$. The consistency of our simulated results with the beam results of BM testifies to the correctness of our approach.

In the test beam run of MINOS with aluminium proportional tube (APT) active detectors and 1.5 inch (4 cm) steel plates, a hadron energy resolution of $71\%/\sqrt{E} \pm 6\%$ was reported in the range 2.5–30 GeV [186]. ICAL simulation with 4 cm iron plates in the same energy range gave $61\%/\sqrt{E} \pm 14\%$. The results are compatible within errors, because the two detector geometries are very different.

Obviously the final choice of the plate thickness depends not only on the behaviour of hadrons but also on the energy range of interest to the physics goals of the experiment. There are also issues of cost, sensitivity to muons and even possibly electrons. The thickness dependence study summarized here provides one such input to the final design.

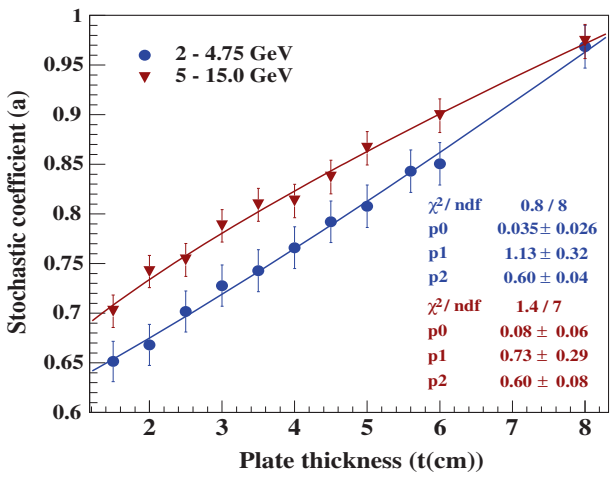

Figure D.3. The stochastic coefficient a obtained from the fit to eq. (D.1) is shown in the two energy ranges as a function of plate thickness [10].

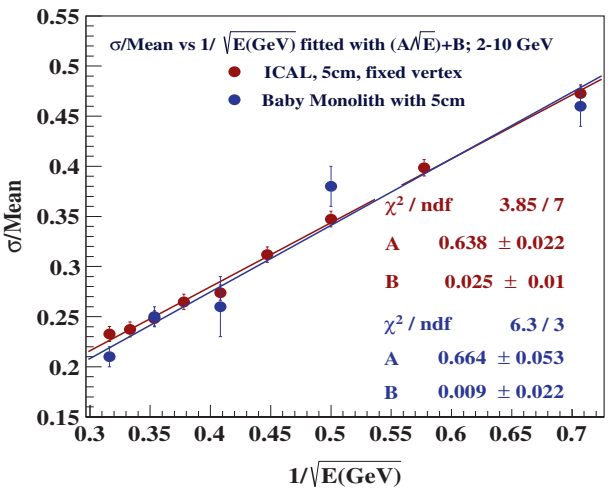

Figure D.4. The energy response of ICAL detector with 5 cm thick iron plates with single pions in the energy range 2–10 GeV, propagated from a fixed vertex in the vertical direction [10] compared with the data from MONOLITH test beam run [184,185].

References

[1] India-based Neutrino Observatory (INO), http://www.ino.tifr.res.in/ino/

[2] INO Collaboration: M S Athar *et al*, *India-based Neutrino Observatory: Project Report Volume I (INO-2006-01)*, 2006

[3] GEANT4 Collaboration: S Agostinelli *et al*, GEANT4: A Simulation toolkit, *Nucl. Instrum. Methods A* **506**, 250 (2003), http://geant4.cern.ch/. counted in INSPIRE as of 05 Apr. 2013

[4] D Casper, *Nucl. Phys. Proc. Suppl.* **112**, 161 (2002), hep-ph/0208030

[5] M Honda, T Kajita, K Kasahara and S Midorikawa, *Phys. Rev. D* **83**, 123001 (2011), arXiv:1102.2688

[6] H Nunokawa, S J Parke and R Zukanovich Funchal, *Phys. Rev. D* **72**, 013009 (2005), hep-ph/0503283

[7] A de Gouvea, J Jenkins and B Kayser, *Phys. Rev. D* **71**, 113009 (2005), hep-ph/0503079

[8] A Chatterjee *et al*, *J. Instrum.* **9**, P07001 (2014), arXiv:1405.7243

[9] M M Devi *et al*, *J. Instrum.* **8**, P11003 (2013), arXiv:1304.5115

[10] S M Lakshmi *et al*, arXiv:1401.2779

[11] A Ghosh, T Thakore and S Choubey, *J. High Energy Phys.* **1304**, 009 (2013), arXiv:1212.1305

[12] T Thakore, A Ghosh, S Choubey and A Dighe, *J. High Energy Phys.* **1305**, 058 (2013), arXiv:1303.2534

[13] D Kaur, M Naimuddin and S Kumar, *Eur. Phys. J. C* **75**(**4**), 156 (2015), arXiv:1409.2231

[14] M M Devi, T Thakore, S K Agarwalla and A Dighe, *J. High Energy Phys.* **1410**, 189 (2014), arXiv:1406.3689

[15] A Chatterjee, R Gandhi and J Singh, *J. High Energy Phys.* **1406**, 045 (2014), arXiv:1402.6265

[16] N Dash, V M Datar and G Majumder, *Astropart. Phys.* **70**, 33 (2015)

[17] S K Agarwalla and T Thakore, Synergy between ICAL atmospheric neutrino data and ongoing long-baseline experiments, T2K and NOvA. (Work in progress, 2015)

[18] M Blennow and T Schwetz, *J. High Energy Phys.* **1208**, 058 (2012), arXiv:1203.3388

[19] M Ghosh, P Ghoshal, S Goswami and S K Raut, *Phys. Rev. D* **89**, 011301 (2014), arXiv:1306.2500

[20] C Cowan, F Reines, F Harrison, H Kruse and A McGuire, *Science* **124**, 103 (1956)

[21] C V Achar *et al*, *Phys. Lett.* **18**, 196 (1965)

[22] F Reines *et al*, *Phys. Rev. Lett.* **15**, 429 (1965)

[23] J Davis, Raymond, D S Harmer and K C Hoffman, *Phys. Rev. Lett.* **20**, 1205 (1968)

[24] B Cleveland *et al*, *Astrophys. J.* **496**, 505 (1998)

[25] Kamiokande-II Collaboration: K Hirata *et al*, *Phys. Rev. D* **44**, 2241 (1991)

[26] Super-Kamiokande Collaboration: Y Fukuda *et al*, *Phys. Rev. Lett.* **81**, 1158 (1998), hep-ex/9805021

[27] Super-Kamiokande Collaboration: Y Fukuda *et al*, *Phys. Rev. Lett.* **81**, 1562 (1998), hep-ex/9807003

[28] SAGE Collaboration: J Abdurashitov *et al*, *Phys. Rev. C* **60**, 055801 (1999), astro-ph/9907113

[29] GALLEX Collaboration: P Anselmann *et al*, *Phys. Lett. B* **285**, 376 (1992)

[30] GALLEX, GNO Collaboration: T Kirsten, *Nucl. Phys. Proc. Suppl.* **77**, 26 (1999)

[31] SNO Collaboration: Q Ahmad *et al*, *Phys. Rev. Lett.* **87**, 071301 (2001), nucl-ex/0106015

[32] SNO Collaboration: Q Ahmad *et al*, *Phys. Rev. Lett.* **89**, 011301 (2002), nucl-ex/0204008

[33] KamLAND Collaboration: K Eguchi *et al*, *Phys. Rev. Lett.* **90**, 021802 (2003), hep-ex/0212021

[34] K2K Collaboration: M Ahn *et al*, *Phys. Rev. Lett.* **90**, 041801 (2003), hep-ex/0212007

[35] Double Chooz Collaboration: Y Abe *et al*, *Phys. Rev. Lett.* **108**, 131801 (2012), arXiv:1112.6353

[36] RENO Collaboration: J Ahn *et al*, *Phys. Rev. Lett.* **108**, 191802 (2012), arXiv:1204.0626

[37] Daya Bay Collaboration: F An *et al*, *Phys. Rev. Lett.* **108**, 171803 (2012), arXiv:1203.1669

[38] MINOS Collaboration: D Michael *et al*, *Phys. Rev. Lett.* **97**, 191801 (2006), hep-ex/0607088

[39] T2K Collaboration: K Abe *et al*, *Phys. Rev. Lett.* **107**, 041801 (2011), arXiv:1106.2822

[40] NOνA Collaboration: P Adamson *et al*, *Phys. Rev. Lett.* **116**(**15**), 151806 (2016), arXiv:1601.0502

[41] NOνA Collaboration: P Adamson *et al*, *Phys. Rev. D* **93**(**5**), 051104 (2016), arXiv:1601.0503

[42] V S Narasimham, *Proc. Indian Natl Sci. Acad. A* **70**(**1**), 11 (2004)

[43] M Krishnaswamy *et al*, *Phys. Lett. B* **57**, 105 (1975)

[44] M Krishnaswamy *et al*, *Pramana – J. Phys.* **5**, 59 (1975)

[45] M R Krishnaswamy *et al*, *Proc. XXIII Int. Conf. on High Energy Physics*, Berkeley, edited by S Loken (World Scientific, 1986)

[46] M Murthy *et al*, *Pramana – J. Phys.* **55**, 347 (2000), hep-ph/0112076

[47] MONOLITH Collaboration: T Tabarelli de Fatis, *MONOLITH: A High resolution neutrino oscillation experiment*, hep-ph/0106252

[48] MONOLITH Collaboration: N Agafonova *et al*, *MONOLITH: A massive magnetized iron detector for neutrino oscillation studies*

[49] S Behera, M Bhatia, V Datar and A Mohanty, *Simulation studies for electromagnetic design of INO ICAL magnet and its response to muons*, arXiv:1406.3965

[50] B Pontecorvo, *Sov. Phys. JETP* **6**, 429 (1957)

[51] Z Maki, M Nakagawa and S Sakata, *Prog. Theor. Phys.* **28**, 870 (1962)

[52] Particle Data Group Collaboration: K Olive *et al*, *Chin. Phys. C* **38**, 090001 (2014)

[53] M Gonzalez-Garcia, M Maltoni and T Schwetz, *J. High Energy Phys.* **1411**, 052 (2014), arXiv:1409.5439

[54] NuFIT webpage, http://www.nu-fit.org/

[55] F Capozzi, E Lisi, A Marrone, D Montanino and A Palazzo, *Nucl. Phys. B* **908**, 218 (2016), arXiv:1601.0777

[56] M C Gonzalez-Garcia, M Maltoni and T Schwetz, *Nucl. Phys. B* **908**, 199 (2016), arXiv:1512.0685

[57] M Gonzalez-Garcia, M Maltoni, T Salvado and Jordi vand Schwetz, *J. High Energy Phys.* **1212**, 123 (2012), arXiv:1209.3023

[58] F Capozzi *et al*, *Phys. Rev. D* **89**, 093018 (2014), arXiv:1312.2878

[59] D Forero, M Tortola and J Valle, *Neutrino oscillations refitted*, arXiv:1405.7540

[60] MINOS Collaboration: P Adamson *et al*, *Phys. Rev. Lett.* **110**, 251801 (2013), arXiv:1304.6335

[61] G L Fogli and E Lisi, *Phys. Rev. D* **54**, 3667 (1996), hep-ph/9604415

[62] CHOOZ Collaboration: M Apollonio *et al*, *Phys. Lett. B* **420**, 397 (1998), hep-ex/9711002

[63] M Narayan, G Rajasekaran and S U Sankar, *Phys. Rev. D* **58**, 031301 (1998), hep-ph/9712409

[64] CHOOZ Collaboration: M Apollonio *et al*, *Phys. Lett. B* **466**, 415 (1999), hep-ex/9907037

[65] Palo Verde Collaboration: A Piepke, *Prog. Part. Nucl. Phys.* **48**, 113 (2002)

[66] T2K Collaboration: K Abe *et al*, *Phys. Rev. Lett.* **112**, 061802 (2014), arXiv:1311.4750

[67] Daya Bay Collaboration: F An *et al*, *Phys. Rev. Lett.* **112**, 061801 (2014), arXiv:1310.6732

[68] D Ayres *et al*, *Letter of intent to build an off-axis detector to study numu to nue oscillations with the NuMI neutrino beam*, hep-ex/0210005

[69] NOνA Collaboration: D Ayres *et al*, *NOνA: Proposal to build a 30 kiloton off-axis detector to study nu(mu) to nu(e) oscillations in the NuMI beamline*, hep-ex/0503053

[70] NOνA Collaboration: D Ayres *et al*, *The NOνA Technical Design Report*, Tech. Rep., FERMILAB-DESIGN-2007-01

[71] IceCube Collaboration: M Aartsen *et al*, *Phys. Rev. D* **91**(**7**), 072004 (2015), arXiv:1410.7227

[72] K Abe *et al*, *Letter of intent: The hyper-Kamiokande experiment – Detector design and physics potential*, arXiv:1109.3262

[73] IceCube-PINGU Collaboration: M Aartsen *et al*, *Letter of intent: The Precision IceCube Next Generation Upgrade (PINGU)*, arXiv:1401.2046

[74] KM3Net Collaboration: S Adrian-Martinez *et al*, *Letter of intent for KM3NeT2.0*, arXiv:1601.0745

[75] DUNE Collaboration: R Acciarri *et al*, *Long-Baseline Neutrino Facility (LBNF) and Deep Underground Neutrino Experiment (DUNE) Conceptual Design Report Volume 2: The Physics Program for DUNE at LBNF*, arXiv:1512.0614

[76] LBNE Collaboration: T Akiri *et al*, *The 2010 Interim report of the long-baseline neutrino experiment collaboration physics working groups*, arXiv:1110.6249

[77] LBNE Collaboration: C Adams *et al*, *Scientific opportunities with the long-baseline neutrino experiment*, arXiv:1307.7335

[78] S K Agarwalla, T Li and A Rubbia, *J. High Energy Phys.* **1205**, 154 (2012), arXiv:1109.6526

[79] A Stahl *et al*, *Expression of interest for a very long-baseline neutrino oscillation experiment (LBNO), CERN-SPSC-2012-021, SPSC-EOI-007*

[80] LAGUNA-LBNO Collaboration: S Agarwalla *et al*, *The mass-hierarchy and CP-violation discovery reach of the LBNO long-baseline neutrino experiment*, arXiv:1312.6520

[81] Y-F Li, J Cao, Y Wang and L Zhan, *Phys. Rev. D* **88**, 013008 (2013), arXiv:1303.6733

[82] JUNO Collaboration: F An *et al*, *Neutrino physics with JUNO*, arXiv:1507.0561

[83] S-B Kim, *Nucl. Part. Phys. Proc.* **265–266**, 93 (2015), arXiv:1412.2199

[84] T2K Collaboration: K Abe *et al*, *Neutrino oscillation physics potential of the T2K experiment*, arXiv:1409.7469

[85] S K Agarwalla, S Prakash, S K Raut and S U Sankar, *J. High Energy Phys.* **1212**, 075 (2012), arXiv:1208.3644

[86] P Huber, M Lindner, T Schwetz and W Winter, *J. High Energy Phys.* **0911**, 044 (2009), arXiv:0907.1896

[87] P Machado, H Minakata, H Nunokawa and R Z Funchal, *What can we learn about the lepton CP phase in the next 10 years?*, arXiv:1307.3248

[88] M Ghosh, P Ghoshal, S Goswami and S K Raut, *Nucl. Phys. B* **884**, 274 (2014), arXiv:1401.7243

[89] S K Agarwalla, S Prakash and S U Sankar, *J. High Energy Phys.* **1307**, 131 (2013), arXiv:1301.2574

[90] S K Agarwalla, S Prakash and S Uma Sankar, *J. High Energy Phys.* **1403**, 087 (2014), arXiv:1304.3251

[91] E Kearns, *Physics with massive water Cherenkov detectors*, 2013, Talk given at the NNN 2013 Workshop, November 11–13, 2013, Kavli IPMU, Japan, http://indico.ipmu.jp/indico/conferenceDisplay.py?confId=17

[92] Super-Kamiokande Collaboration: M Ishitsuka, *Super-Kamiokande results: Atmospheric and solar neutrinos*, hep-ex/0406076

[93] R Gandhi and S Panda, *J. Cosmol. Astropart. Phys.* **0607**, 011 (2006), hep-ph/0512179

[94] S Panda and S Sinegovsky, *Int. J. Mod. Phys. A* **23**, 2933 (2008), arXiv:0710.3125

[95] A S Joshipura and S Mohanty, *Phys. Lett. B* **584**, 103 (2004), hep-ph/0310210

[96] A Datta, R Gandhi, P Mehta and S U Sankar, *Phys. Lett. B* **597**, 356 (2004), hep-ph/0312027

[97] A Chatterjee, P Mehta, D Choudhury and R Gandhi, *Testing non-standard neutrino matter interactions in atmospheric neutrino propagation*, arXiv:1409.8472

[98] M V N Murthy and G Rajasekaran, *Pramana – J. Phys.* **82**, 609 (2014), arXiv:1305.2715

[99] N Dash, V Datar and G Majumder, *Sensitivity for detection of decay of dark matter particle using ICAL at INO*, arXiv:1410.5182, to be published in Pramana

[100] M Honda, T Kajita, K Kasahara, S Midorikawa and T Sanuki, *Phys. Rev. D* **75**, 043006 (2007), astro-ph/0611418

[101] G Barr, T Gaisser, P Lipari, S Robbins and T Stanev, *Phys. Rev. D* **70**, 023006 (2004), astro-ph/0403630

[102] G Battistoni, A Ferrari, T Montaruli and P Sala, *Astropart. Phys.* **19**, 269 (2003), hep-ph/0207035

[103] T Gaisser and M Honda, *Ann. Rev. Nucl. Part. Sci.* **52**, 153 (2002), hep-ph/0203272

[104] M Honda, M Sajjad Athar, T Kajita, K Kasahara and S Midorikawa. Atmospheric neutrino flux calculation using MSISIE00 atmosphere model, *Phys. Rev. D*, to be submitted, 2015

[105] M Sajjad Athar, M Honda, T Kajita, K Kasahara and S Midorikawa, *Phys. Lett. B* **718**, 1375 (2013), arXiv:1210.5154

[106] C Andreopoulos *et al*, *Nucl. Instrum. Methods A* **614**, 87 (2010), arXiv:0905.2517

[107] J L Hewett *et al*, *Fundamental physics at the intensity frontier*, doi: 10.2172/1042577, arXiv:1205.2671 [hep-ex]

[108] J A Formaggio *et al*, *Rev. Mod. Phys.* **84**, 1307 (2012)

[109] Infolytica Corp., Electromagnetic field simulation software, http://www.infolytica.com/en/products/magnet/

[110] B Satyanarayana, *Design and characterisation studies of resistive plate chambers*, Ph.D. thesis, PHY-PHD-10-701, (Department of Physics, IIT Bombay, 2009)

[111] J S Marshall, *A study of muon neutrino disappearance with the MINOS detectors and the NuMI neutrino beam*, Ph.D. thesis (University of Cambridge, 2008)

[112] E Wolin and L Ho, *Nucl. Instrum. Methods A* **329**, 493 (1993)

[113] H Bethe and J Ashkin, *Experimental nuclear physics* edited by E Segré (J Wiley, New York, 1953), p. 253

[114] K Bhattacharya, A K Pal, G Majumder and N K Mondal, *Comput. Phys. Commun.* **185**, 3259 (2014)

[115] Particle Data Group: J Beringer *et al*, *Phys. Rev. D* **86**, 010001 (2012), see also arXiv:1204.0626v2 [hep-ex]
[116] D Indumathi and N Sinha, *Phys. Rev. D* **80**, 113012 (2009), arXiv:0910.2020
[117] R Kanishka, K K Meghna, V Bhatnagar, D Indumathi and N Sinha, *J. Instrum.* **10**(**3**), P03011 (2015), arXiv:1503.0336
[118] M Blennow, P Coloma, P Huber and T Schwetz, *J. High Energy Phys.* **1403**, 028 (2014), arXiv:1311.1822
[119] G Cowan, K Cranmer, E Gross and O Vitells, *Eur. Phys. J. C* **71**, 1554 (2011), arXiv:1007.1727; Erratum, *Eur. Phys. J. C* **73**, 2501 (2013)
[120] G Fogli *et al*, *Phys. Rev. D* **67**, 073002 (2003), hep-ph/0212127
[121] P Huber, M Lindner and W Winter, *Nucl. Phys. B* **645**, 3 (2002), hep-ph/0204352
[122] R Gandhi *et al*, *Phys. Rev. D* **76**, 073012 (2007), arXiv:0707.1723
[123] M Gonzalez-Garcia and M Maltoni, *Phys. Rev. D* **70**, 033010 (2004), hep-ph/0404085
[124] S Choubey and P Roy, *Phys. Rev. D* **73**, 013006 (2006), hep-ph/0509197
[125] V Barger *et al*, *Phys. Rev. Lett.* **109**, 091801 (2012), arXiv:1203.6012
[126] D Indumathi, M Murthy, G Rajasekaran and N Sinha, *Phys. Rev. D* **74**, 053004 (2006), hep-ph/0603264
[127] Super-Kamiokande Collaboration: A Himmel, *Recent atmospheric neutrino results from Super-Kamiokande*, arXiv:1310.6677
[128] MINOS Collaboration: P Adamson *et al*, *Phys. Rev. Lett.* (2014), arXiv:1403.0867
[129] T2K Collaboration: K Abe *et al*, *Precise measurement of the neutrino mixing parameter* θ_{23} *from muon neutrino disappearance in an off-axis beam*, arXiv:1403.1532
[130] S Choubey and A Ghosh, *J. High Energy Phys.* **1311**, 166 (2013), arXiv:1309.5760
[131] KM3NeT Collaboration: U F Katz, The ORCA Option for KM3NeT, in: *Proceedings of the 15th International Workshop on Neutrino Telescopes (Neutel 2013)* (2014), arXiv:1402.1022
[132] Y-F Li, *Overview of the Jiangmen Underground Neutrino Observatory (JUNO)*, arXiv:1402.6143
[133] S T Petcov and M Piai, *Phys. Lett. B* **533**, 94 (2002), hep-ph/0112074
[134] S Choubey, S T Petcov and M Piai, *Phys. Rev. D* **68**, 113006 (2003), hep-ph/0306017
[135] INO Collaboration: S Goswami, *Neutrino Phenomenology: Highlights of oscillation results and future prospects*, 2014, talk given at the ICHEP 2014 Conference, July 2–9, 2014, Valencia, Spain, http://ichep2014.es/
[136] P Huber, M Lindner and W Winter, *Comput. Phys. Commun.* **167**, 195 (2005), hep-ph/0407333
[137] P Huber, J Kopp, M Lindner, M Rolinec and W Winter, *Comput. Phys. Commun.* **177**, 432 (2007), hep-ph/0701187
[138] K Abe *et al*, *Letter of intent: The Hyper-Kamiokande experiment – detector design and physics potential —*, arXiv:1109.3262
[139] T2K Collaboration: Y Itow *et al*, *The JHF-Kamioka neutrino project*, hep-ex/0106019
[140] T2K Collaboration: K Abe *et al*, *Nucl. Instrum. Methods A* **659**, 106 (2011), arXiv:1106.1238
[141] W Pauli, *Exclusion principle, Lorentz group and reflection of space-time and charge* (Pergamon Press, London, 1955)
[142] G Grawert, G Luders and H Rollnik, *Fortschr. d. Phys.* **7**, 291 (1959)
[143] V A Kostelecky and M Mewes, *Phys. Rev. D* **70**, 031902 (2004), hep-ph/0308300
[144] V A Kostelecky and M Mewes, *Phys. Rev. D* **69**, 016005 (2004), hep-ph/0309025
[145] Super-Kamiokande Collaboration: K Abe *et al*, *Phys. Rev. D* **91**(**5**), 052003 (2015), arXiv:1410.4267
[146] A Bhattacharya, S Choubey, R Gandhi and A Watanabe, *J. Cosmol. Astropart. Phys.* **1009**, 009 (2010), arXiv:1006.3082
[147] D Colladay and V A Kostelecky, *Phys. Rev. D* **55**, 6760 (1997), hep-ph/9703464
[148] O Greenberg, *Phys. Rev. Lett.* **89**, 231602 (2002), hep-ph/0201258
[149] S R Coleman and S L Glashow, *Phys. Rev. D* **59**, 116008 (1999), hep-ph/9812418
[150] P A M Dirac, *Proc. R. Soc. A* **133**, 60 (1931)
[151] M N Saha, *Ind. J. Phys.* **10**, 141 (1936)
[152] G t Hooft, *Nucl. Phys. B* **79**, 276 (1974)
[153] A M Polyakov, *JETP Lett.* **20**, 194 (1974)
[154] J Derkaoui *et al*, *Astropart. Phys.* **9**, 173 (1998)
[155] E Parker, *Astrophys. J.* **160**, 383 (1970)
[156] B Cabrera, *Phys. Rev. Lett.* **48**, 1378 (1982)
[157] S Bermon *et al*, *Phys. Rev. Lett.* **64**, 839 (1990)
[158] T Kajita *et al*, *J. Phys. Soc. Jpn* **54**, 4065 (1985)
[159] V Aynutdinov *et al*, *Astropart. Phys.* **29**, 366 (2008)
[160] Soudan 2 Collaboration: J L Thron *et al*, *Phys. Rev. D* **46**, 4846 (1992)
[161] MACRO Collaboration: M Ambrosio *et al*, *Eur. Phys. J. C* **25**, 511 (2002)
[162] S Balestra *et al*, *Eur. Phys. J. C* **55**, 57 (2008)
[163] CDF Collaboration: A Abulencia *et al*, *Phys. Rev. Lett.* **96**, 201801 (2006)
[164] G R Kalbfleisch *et al*, *Phys. Rev. Lett.* **85**, 5292 (2000)
[165] ATLAS Collaboration: G Aad *et al*, *Phys. Rev. Lett.* **109**, 261803 (2006)
[166] S P Ahlen, *Phys. Rev. D* **17**, 229 (1978)
[167] S P Ahlen and K Kinoshita, *Phys. Rev. D* **26**, 2347 (1982)
[168] J Derkaoui *et al*, *Astropart. Phys.* **10**, 339 (1999)
[169] AMS Collaboration: J Alcaraz *et al*, *Phys. Lett. B* **490**, 27 (2000)
[170] T Sanuki *et al*, *Astrophys. J.* **545**, 1135 (2000), astro-ph/0002481
[171] S Haino *et al*, *Phys. Lett. B* **594**, 35 (2004), astro-ph/0403704
[172] S Roesler, R Engel and J Ranft, *The Monte Carlo event generator DPMJET-III*, hep-ph/0012252
[173] http://en.wikipedia.org/wiki/NRLMSISE-00
[174] http://www.ngdc.noaa.gov/IAGA/vmod/igrf.html
[175] T Sanuki, M Honda, T Kajita, K Kasahara and S Midorikawa, *Phys. Rev. D* **75**, 043005 (2007), astro-ph/0611201
[176] M Freund, *Phys. Rev. D* **64**, 053003 (2001), hep-ph/0103300
[177] E K Akhmedov, R Johansson, M Lindner, T Ohlsson and T Schwetz, *J. High Energy Phys.* **0404**, 078 (2004), hep-ph/0402175
[178] A Dziewonski and D Anderson, *Phys. Earth Planet. Interiors* **25**, 297 (1981)

[179] M Banuls, G Barenboim and J Bernabeu, *Phys. Lett. B* **513**, 391 (2001), hep-ph/0102184
[180] R Gandhi, P Ghoshal, S Goswami, P Mehta and S U Sankar, *Phys. Rev. Lett.* **94**, 051801 (2005), hep-ph/0408361
[181] S Choubey and P Roy, *Phys. Rev. Lett.* **93**, 021803 (2004), hep-ph/0310316
[182] B Schorr, *Comp. Phys. Commun.* **7**, 215 (1974); see also A Rotondi and P Montagna, *Nucl. Instrum. Methods B* **47** 215 (1990)
[183] D Green, Physics of Particle Detectors, *Cambridge Monographs on Particle Physics, Nuclear Physics and Cosmology* (Cambridge University Press, 2000) pp. 266–8
[184] M Ambrosio *et al*, *Nucl. Instrum. Methods A* **456**, 67 (2000)
[185] G Bari *et al*, *Nucl. Instrum. Methods A* **508**, 170 (2003)
[186] D A Petyt, *A study of parameter measurement in a long-baseline neutrino oscillation experiment*, Ph.D. thesis, University of Oxford, Preprint FERMILAB-THESIS-1998-66 (1998)